Ultraviolet Photoemission and Inverse-Photoemission Spectroscopies of Diluted Magnetic Semiconductor $Cd_{1-x}Mn_xTe$

Kojiro MIMURA

1997. 1.

Hiroshima Synchrotron Radiation Center, Hiroshima University
Kagamiyama 2-313, Higashi-Hiroshima 739, Japan

Contents

List of abbreviations

BIS : bremsstrahlung isochromat spectroscopy
CBM : conduction-band minimum
CIS : constant-initial-state
DCMA : double-stage cylindrical mirror analyzer
DOS : density of states
EXAFS : extended X-ray absorption fine-structure
FWHM : full width at half maximum
HWE : hot wall epitaxy
IPES : inverse-photoemission spectroscopy
LEED : low-energy electron diffraction
PES : photoemission spectroscopy
RPES : resonant photoemission spectroscopy
UPS : ultraviolet photoemission spectroscopy
VBM : valence-band maximum
XANES : X-ray absorption near edge structure
XPS : X-ray photoemission spectroscopy
XRD : X-ray diffraction

Abstract

Valence-band and conduction-band densities of states (DOS's) of $Cd_{1-x}Mn_xTe$ epitaxial films ($0 \leq x \leq 0.7$) have been investigated by means of *in situ* measurements of ultraviolet photoemission and inverse-photoemission spectroscopies (UPS and IPES).

Based on one-electron band theory, features observed at –3.4 and 3.6 eV relative to the valence-band maximum (VBM) are ascribed to emission from the Mn $3d\downarrow$ and $3d\uparrow$ states with e_g symmetry, respectively, providing a Mn $3d$ spin-exchange splitting energy (U_{eff}) of 7.0±0.2 eV. This value compares well with the value predicted in the theoretical investigation of electronic structures and magnetic properties of $Cd_{1-x}Mn_xTe$. With increasing Mn concentration, the energy position of the conduction-band minimum shifts almost linearly toward higher energy relative to the VBM as a result of an increasing contribution of the higher-lying Mn $4s$ level relative to the Cd $5s$ level.

Mn $3d$ partial DOS's in the valence-band region of $Cd_{1-x}Mn_xTe$ have been determined from resonant photoemission spectroscopy in the Mn $3p$-$3d$ core excitation region. The partial DOS's reveal an appreciable contribution of the Mn $3d$ states to the top 9 eV of valence bands with three structures; valence bands at 0~–2.5 eV, a main peak at –3.4 eV and a multielectron satellite at –5~–9 eV. These features are almost independent of the Mn concentration. Apart from one-electron band theory, the whole spectrum including the multielectron satellite is found to be well reproduced in terms of the configuration interaction theory using a $Mn^{2+}(Te^{2-})_4$ model cluster.

Electronic structures of zinc-blende MnTe epitaxial films have also been investigated by means of UPS and IPES. The U_{eff}-value of zinc-blende MnTe is in good agreement with those of $Cd_{1-x}Mn_xTe$ and $Zn_{1-x}Mn_xTe$. The width of valence bands and U_{eff} are by 1.3 eV narrower and by 0.3 eV larger than those of NiAs-type MnTe, respectively.

Chapter 1.
Introduction

Diluted magnetic semiconductors (DMS's) are ternary alloys where magnetic atoms such as Mn and Fe randomly replace some of the cations in the lattice of host semiconductor crystals. Most of these materials are based on $A^{II}B^{VI}$ compounds (A^{II} = Zn, Cd, Hg; B^{VI} = S, Se, Te), with a fraction of the group-II constituent replaced by Mn.

The entire family of ternary $A^{II}_{1-x}Mn_xB^{VI}$ alloys can schematically be represented, as shown in Fig. 1-1. The thick lines in the figure show the Mn concentration (x) ranges in which ternary alloys can be formed [1, 2]. "Cub" and "Hex" indicate zinc-blende and wurtzite crystal

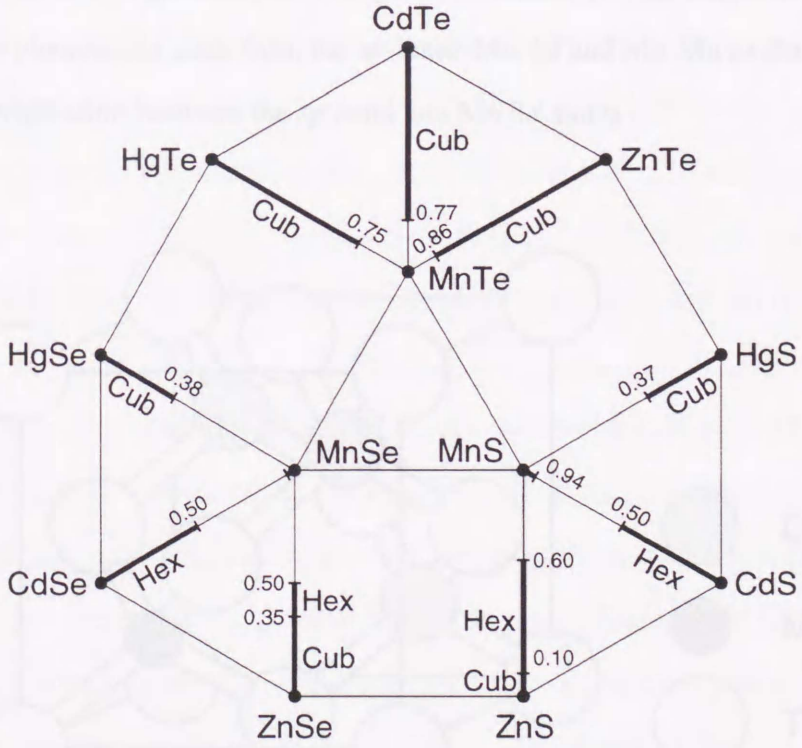

Fig. 1-1. A schematic overview of the alloys and their crystal structures [1]. The thick lines indicate ranges of the Mn concentration (x) for which homogeneous crystal phases form. "Cub" and "Hex" indicate zinc-blende and wurtzite structure, respectively.

structure of the stable phase, respectively. For example, $Cd_{1-x}Mn_xTe$, which is the material investigated in the present study, forms a ternary alloy of zinc-blende structure (as shown in Fig. 1-2) with x up to 0.77, while $Zn_{1-x}Mn_xSe$ exhibits zinc-blende structure for $x < 0.30$ and wurtzite structure for $0.30 < x < 0.55$. At values of x indicated by the thin lines, mixed phases occur.

The ternary $A^{II}_{1-x}Mn_xB^{VI}$ alloys have attracted much attention for several reasons. Firstly, their semiconducting and structural properties, such as the energy gap, the lattice constant and so on, can controllably be varied by varying the x. For example, the energy band gap and the lattice constant of $Cd_{1-x}Mn_xTe$ change linearly from 1.528 to 2.541 eV and from 6.481 to 6.368 Å, respectively, with the increase of x from 0 to 0.77 [1, 2]. Secondly, these materials are of interest for their magnetic and magneto-optical properties, e.g., the spin-glass transition [3, 4], antiferromagnetic cluster formation [5], magnon excitations [6], extremely large Faraday rotation [7], giant negative magneto-resistance [8], the magnetic polaron [9, 10], and so on. Such phenomena stem from the *sp*-band–Mn 3*d* and Mn-Mn exchange interactions through the hybridization between the *sp* band and Mn 3*d* states .

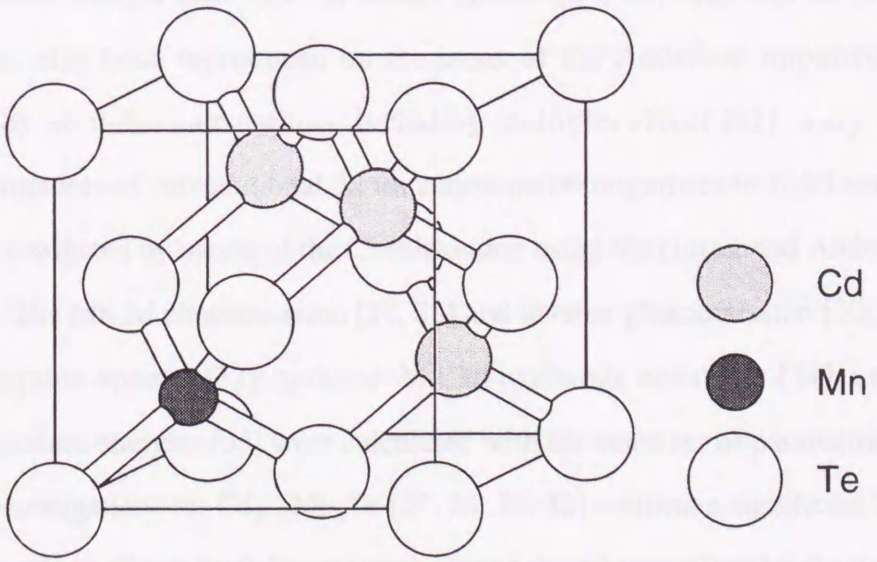

Fig. 1-2. Crystal structure of $Cd_{1-x}Mn_xTe$. $Cd_{1-x}Mn_xTe$ exhibits zinc-blende structure of single phase in the range of $0 \leq x \leq 0.77$.

The band structure and magnetic properties of Mn substituted DMS's have been theoretically investigated [11–20] based on a local-spin-density augmented-spherical-wave method [11, 12], a combination of *ab initio* spin-polarized band calculations, a semiempirical tight binding model containing available experimental data and consideration of alloying effects [13–16], self-consistent spin-polarized spin-density functional band-structure calculations [17], spin-polarized, self-consistent local-spin density total-energy and band-structure calculations [18, 19], and self-consistent local-density pseudofunction theory [20, 21]. The theoretical *sp*-band–Mn 3*d* and Mn-Mn exchange constants [13–16] are in fairly good agreement with the results from the enhanced Zeeman splittings of free-exciton lines in magneto-optical experiments [22], and those from magnetization [23, 24] and neutron scattering [25] experiments, respectively.

In recent years, the contribution of the Mn 3*d* states to the valence-band density of states (DOS) has been investigated experimentally to study the hybridization between the *sp*-band and Mn 3*d* states [20, 21, 26–30]. Resonant photoemission experiments using tunable synchrotron radiation (SR) provided a successful measure of the Mn 3*d* partial DOS of $Cd_{1-x}Mn_xTe$ with $x = 0.65$ [27]. The spectral features have been analyzed in terms of a configuration-interaction (CI) calculation using a $Mn^{2+}(Te^{2-})_4$ model cluster [27, 28]. The Mn 3*d* photoemission spectrum has also been reproduced on the basis of the Anderson impurity model with parameters by *ab initio* calculations, including multiplet effect [31]. Very recently, the electronic structures of substitutional 3*d* transition-metal impurities in II-VI semiconductors have been investigated by means of the CI calculation using the cluster and Anderson impurity models [32]. The Mn 3*d* photoemission [27, 28] and inverse-photoemission [20] spectra, d-d^* optical-absorption spectra [33], *sp*-band–Mn 3*d* exchange constants [34], and donor and acceptor ionization energies [35] were calculated with the same set of parameters [32]. These theoretical investigations for $Cd_{1-x}Mn_xTe$ [27, 28, 31, 32] confirm a significant Mn 3*d*–Te 5*p* hybridization which allows for sufficient screening of the 3*d* excitations by the ligand to *d*-hole charge transfer in the valence bands. In that sense, the spectral density at the top 5 eV of the valence bands can be assumed to be a good approximation for a measure of the valence-band

DOS [27].

The first attempt to investigate directly the conduction-band states of $Cd_{1-x}Mn_xTe$ has been made by Franciosi *et al.* using bremsstrahlung isochromat spectroscopy (BIS) at the photon energy of 1486.6 eV with a spectrometer resolution of 0.7 eV [20, 21]. The Mn-derived feature was observed at 4.8 eV above the valence-band maximum (VBM) and the Mn 3*d* spin-exchange splitting energy (U_{eff}) was estimated to be 8.3±0.4 eV. From a comparison with electronic structures of antiferromagnetic zinc-blende MnTe based on a local-density functional model calculation [20, 21], these authors have claimed that the ground-state configuration of the Mn is primarily $(d\uparrow)^5(s\uparrow)(p\uparrow)$ rather than $(d\uparrow)^5s^2$. The BIS measurements, however, suffered from experimental difficulties such as an electron-beam induced sample damage and a serious electrostatic charging effect, because the spectra were obtained as the sum of 20 quantitatively consistent spectra from different cleavage surfaces, which corresponds to a total of some 150 hours of data integration with a primary electron beam current of about 200 μA. The unoccupied states of $Cd_{0.5}Mn_{0.5}Te$ have also been investigated by Kisiel *et al.* using X-ray absorption near edge structure (XANES) spectroscopy [36]. The Te L_1 and L_3 edge XANES spectra were analyzed in combination with the electronic structure calculation in terms of a localized muffin-tin orbital method with local-spin-density approximation. The best agreement between the experiment and theory was obtained in the case for which the Mn 3*d* states were placed approximately at 3.3±0.5 eV above the VBM.

In the present study, we report valence-band and conduction-band spectra of $Cd_{1-x}Mn_xTe$ films ($0 \le x \le 0.7$) grown epitaxially on GaAs(100) substrates, measured *in situ* by means of ultraviolet photoemission and inverse-photoemission spectroscopies (UPS and IPES). The IPES spectra have successfully been obtained by preparing thin epitaxial films on GaAs(100) substrates with very low resistivity using a hot wall epitaxy (HWE) reactor specially constructed for this purpose, to overcome the electrostatic charging effect. In addition, in order to investigate the Mn 3*d* states in $Cd_{1-x}Mn_xTe$ in detail, resonant photoemission spectroscopy (RPES) measurements in the Mn 3*p*-3*d* core excitation region have been performed for bulk $Cd_{1-x}Mn_xTe$ samples ($0 \le x \le 0.69$). *In situ* measurements of UPS and IPES spectra make it

possible to connect these spectra at the Fermi level (see Chap. 4-1) and make it possible to determine directly the U_{eff}-value to be 7.0±0.2 eV. We shall discuss the UPS and IPES spectra, and a measure of Mn 3*d* partial density of states evaluated from the RPES spectra in comparison with the results of band-structure calculation in terms of the tight-binding semiempirical coherent potential approximation for $Cd_{1-x}Mn_xTe$ [13], and also with those of the CI calculation using a $Mn^{2+}(Te^{2-})_4$ model cluster [32] in distinction from the one-electron band picture.

We also report electronic structures of zinc-blende MnTe, as an end point material of $Cd_{1-x}Mn_xTe$ ($x = 1$), by means of UPS and IPES. The U_{eff}-value of zinc-blende MnTe is in good agreement with those of $Cd_{1-x}Mn_xTe$ and $Zn_{1-x}Mn_xTe$ [37–39]. We discuss the UPS and IPES spectra of zinc-blende MnTe in comparison with the results of band structure calculation in terms of the spin-polarized, self-consistent local-spin-density total-energy and band-structure calculation [19], and the UPS and IPES spectra of NiAs-type MnTe [40].

The construction of this thesis is as follows. In Chapter 2, we give a general description of photoemission and inverse-photoemission spectroscopy. In Chapter 3, fundamental aspects of the HWE are described, and the constitution of the HWE system constructed in the present study for the UPS and IPES measurements of DMS's is presented in detail. The experimental procedure for the UPS and IPES measurements of $Cd_{1-x}Mn_xTe$ epitaxial films ($0 \le x \le 0.7$) and zinc-blende MnTe epitaxial film ($x = 1$) is described in Chapter 4. The experimental procedure for the RPES measurements of bulk $Cd_{1-x}Mn_xTe$ samples ($0 \le x \le 0.69$) is described in Chapter 5. In Chapter 6, we introduce UPS, IPES and RPES spectra of $Cd_{1-x}Mn_xTe$ ($0 \le x \le 1$), and discuss them in comparison with not only the one-electron band picture but also with the CI calculation. Finally, we summarize our work in Chapter 7.

References

[1] *Diluted Magnetic Semiconductors,* Vol. 25 of Semiconductors and Semimetals, edited by J.K. Furdyna and J. Kossut (Academic, New York, 1988) and references therein.

[2] *Diluted Magnetic Semiconductors,* edited by M. Jain (World Scientific, Singapore, 1991) and references therein.

[3] R.R. Galazka, in *Proceendings of the Internatioal Conference on Narrow Gap Semiconsuctors, Linz, Sept. 1981*, Lecture Notes in Physics **152** (1982, Berlin, Springer-Verlag).

[4] S.B. Oseroff, Phys. Rev. **25** (1982) 6584.

[5] T. Dolling, T.M. Holden, V.F. Sears, J.K. Furdyna and W. Giriat, J. Appl. Phys. **53** (1982) 7644.

[6] A.K. Ramdas, J. Appl. Phys. **53** (1982) 7649.

[7] J.A. Gaj, R.R. Galazka and M. Nawrocki, Solid State Commun. **25** (1978) 193.

[8] A. Micielski and J. Micielski, J. Phys. Soc. Japan **49** (1980) 809.

[9] M. Nawrocki, R. Planel, G. Fishman and R.R. Galazka, Phys. Rev. Lett. **46** (1981) 735.

[10] T. Dietl and J. Spalek, Phys. Rev. B **28** (1983) 1548.

[11] B.E. Larson, K.C. Hass, M. Ehrenreich and A.E. Carlsson, Solid State Commun. **56** (1985) 347.

[12] K.C. Hass, B.E. Larson, H. Ehrenreich and A.E. Carlsson, J. Magn. Magn. Mater. **54-57** (1986) 1283.

[13] H. Ehrenreich, K.C. Hass, N.F. Johnson, B.E. Larson and R.J. Lampert, in *Proceedings of the 18th International Conference of the Physics* of Semiconductors, edited by O. Engstrom (World Scientific, Singapore, 1987), pp.1751-1754.

[14] B.E. Larson, K.C. Hass, H. Ehrenreich and A.E. Carlsson, Phys. Rev. B **37** (1988) 4137 (1988).

[15] B.E. Larson and H. Ehrenreich, Phys. Rev. B **39** (1989) 1747.

[16] B.E. Larson and H. Ehrenreich, J. Appl. Phys. **67** (1990) 5084.

[17] M. Podgórny, Z. Phys. B **69** (1988) 501.

[18] S.-H. Wei and A. Zunger, Phys. Rev. Lett. **56** (1986) 2391.

[19] S.-H. Wei and A. Zunger, Phys. Rev. B **35** (1987) 2340.

[20] A. Franciosi, A. Wall, Y. Gao, J.H. Weaver, M.-H. Tsai, J.D. Dow, R.V. Kasowski, R. Reifenberger and F. Pool, Phys. Rev. B **40** (1989) 12009.

[21] A. Wall, A. Franciosi, Y. Gao, J.H. Weaver, M.-H. Tsai, J.D. Dow and R.V. Kasowski, J. Vac. Sci. Technol. A **7** (1989) 656.

[22] J.A. Gaj, R. Planel and G. Fishman, Solid State Commun. **29** (1979) 435.

[23] B.E. Larson, K.C. Hass, and R.L. Aggwal, Phys. Rev. B **33** (1986) 1789.

[24] Y. Shapira and N.F. Olivera, Jr, Phys. Rev. B **35** (1987) 6888.

[25] T. Giebultowicz, B. Lebech, B. Buras, W. Minor, H. Kepa and R.R. Galazka, J. Appl. Phys. **55** (1984) 2305.

[26] M. Taniguchi, L. Ley, R.L. Johnson, J. Ghijsen and M. Cardona, Phys. Rev. B 33 (1986) 1206.

[27] L. Ley, M. Taniguchi, J. Ghijsen, R.L. Johnson and A. Fujimori, Phys. Rev. B 35 (1987) 2839.

[28] M. Taniguchi, A. Fujimori, M. Fujisawa, T. Mori, I. Souma and Y. Oka, Solid State Commun. **62** (1987) 431.

[29] M. Taniguchi, K. Soda, I. Souma and Y. Oka, Phys. Rev. B **46** (1992) 15789.

[30] A. Wall, A. Raisanen, G. Haugstad, L. Vanzetti and A. Franciosi, Phys. Rev. B **44** (1991) 8185.

[31] O. Gunnarsson, A.V. Postnikov and O.K. Andersen, Phys. Rev. B **39** (1989) 1708; Phys. Rev. B **40** (1989) 10407.

[32] T. Mizokawa and A. Fujimori, Phys. Rev. B **48** (1993) 14150; A. Fujimori and T. Mizokawa, Electronic Structure of 3*d* Transition-Metal Impurities in Semiconductors, in *II-VI Semiconductor Compounds,* edited by M. Jain (World Scientific, Singapore, 1992) p.103.

[33] Y.R. Lee and A.K. Ramdas, Solid State Commun. **51** (1984) 861.

[34] J.K. Furdyna, J. Appl. Phys. **64** (1988) R29.

[35] A. Fazzio, M.J. Caldas and A. Zunger, Phys. Rev. B **30** (1984) 3430.

[36] A. Kisiel, J. Oleszkiewicz, M. Podgórny, G. Dalba, F. Rocca and E. Burattini, J. Cryst. Growth 101 (1990) 239.

[37] M. Taniguchi, N. Happo, K. Mimura, H. Sato, J. Harada, K. Miyazaki, H. Namatame, Y. Ueda and M. Ohashi, J. Phys.: Condens. Matter **7** (1995) 4371.

[38] K. Mimura, N. Happo, H. Sato, J. Harada, K. Miyazaki, H. Namatame, Y. Ueda, M. Ohashi and M. Taniguchi, Cryst. Res. Technol. **31** (1996) 911.

[39] K. Mimura, N. Happo, H. Sato, J. Harada, K. Miyazaki, H. Namatame, Y. Ueda, M. Ohashi and M. Taniguchi, J. Electron Spectrosc. Related Phenom. **79** (1996) 13.

[40] H. Sato, M. Tamura, N. Happo, T. Mihara, M. Taniguchi and Y. Ueda, Solid State Commun. **92** (1994) 921.

Chapter 2.
General description of photoemission and inverse-photoemission spectroscopy

2-1. Photoemission spectroscopy

Photoemission spectroscopy (PES) is a direct experimental method to investigate electronic states in solids and an old experimental technique still in extensive use. A schematic drawing of PES experiments and the principle of the PES process are illustrated in Fig. 2-1 and Fig. 2-2 [1, 2], respectively. In the PES experiments, the light impinges on the sample, and the electrons excited by photoelectric effect are then analyzed with respect to their kinetic energy and their momentum in an energy analyzer. The phenomenon of photoemission was detected by

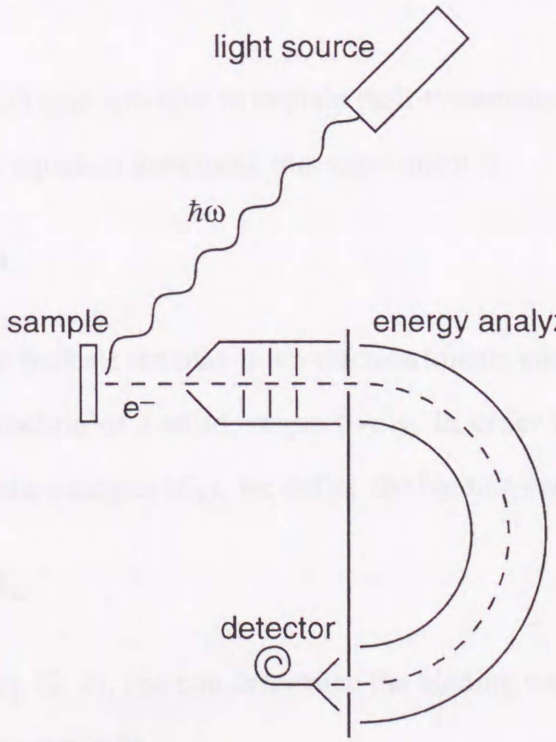

Fig. 2-1. Schematic drawing of a photoemission experiment.

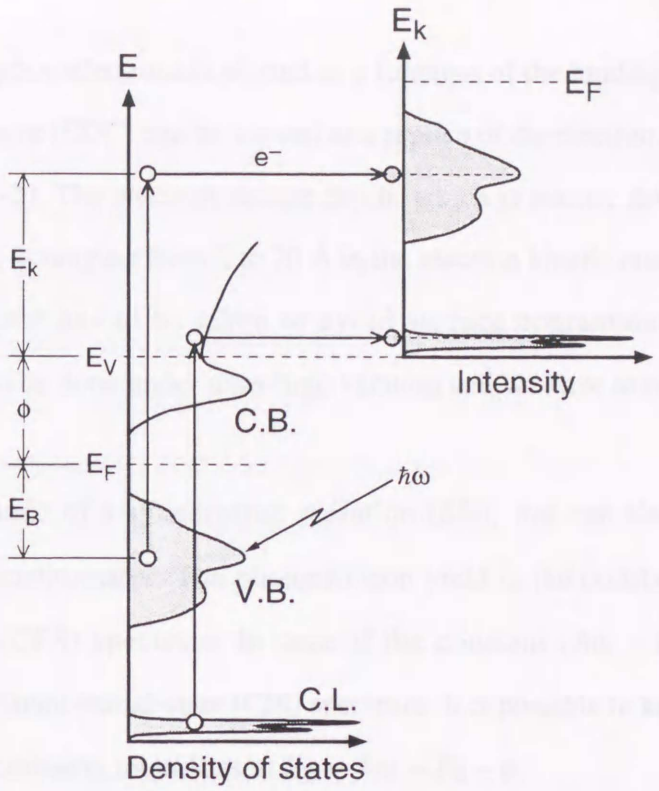

Fig. 2-2. Schematic diagram of the process of photoemission spectroscopy.

Hertz in 1887. In 1905, Einstein was able to explain their systematics by invoking the quantum nature of light. The basic equation governing this experiment is,

$$E_{\text{kin, max}} = \hbar\omega - \phi, \tag{2. 1}$$

where $E_{\text{kin, max}}$, $\hbar\omega$ and ϕ indicate the maximum electron kinetic energy, the energy of incident photon and the work function of a solid, respectively. In order to extend this equation to electrons with lower kinetic energies (E_{k}), we define the binding energy (E_{B}) as follows,

$$E_{\text{B}} = E_{\text{kin, max}} - E_{\text{k}}. \tag{2. 2}$$

By using eq. (2. 1) and eq. (2. 2), one can determine the binding energy of the electrons in the sample from the following equation,

$$E_{\text{B}} = \hbar\omega - \phi - E_{\text{k}}. \tag{2. 3}$$

In the number of the photoelectrons is plotted as a function of the binding energy, the obtained energy distribution curve (EDC) can be viewed as a replica of the electron energy distribution in the solids (see Fig. 2-2). The electron escape depth, which is mainly determined by plasmon energy losses in solid, is ranging from 2 to 20 Å in the electron kinetic energy range of PES [2]. Therefore, special care has to be taken to avoid surface contamination or degradation. Measurements have to be done under ultra-high vacuum and we have to make effort to obtain a fresh surface.

When use is mode of a synchrotron radiation (SR), $\hbar\omega$ can also experimentally be changed using a monochromator. The photoelectron yield in the constant E_k mode is called constant-final-state (CFS) spectrum. In case of the constant ($\hbar\omega - E_k$)-value mode, the spectrum is called constant-initial-state (CIS) spectrum. It is possible to know the detailed $\hbar\omega$-dependence of photoemission intensities at $E_B = \hbar\omega - E_k - \phi$.

Furthermore, in the case of PES experiments for $Cd_{1-x}Mn_xTe$ using synchrotron radiation, a resonance takes place over a specific energy range as a results of the interference between the direct excitation process of Mn 3*d* electrons,

$$3p^6 3d^5 + \hbar\omega \rightarrow 3p^6 3d^4 + \varepsilon_f, \tag{2. 4}$$

and the discrete Mn 3*p*-3*d* core-excitation process followed by a super-Coster-Kronig decay,

$$\begin{aligned} 3p^6 3d^5 + \hbar\omega &\rightarrow 3p^5 3d^6, \\ 3p^5 3d^6 &\rightarrow 3p^6 3d^4 + \varepsilon_f. \end{aligned} \tag{2. 5}$$

where ε_f denotes a photoelectron. Since only the Mn 3*d* states are resonantly enhanced for $\hbar\omega$ near the Mn 3*p*-3*d* core excitation, one can quantitatively estimate the contribution to the valence-band density of states by comparing the spectra taken just on resonance and antiresonance [3, 4]. The cross sections of other valence-band states, such as the Te 5*p* and Cd 5*s* states, do not very appreciably over a small energy range (~2.5 eV) around the resonance.

2-2. Inverse-photoemission spectroscopy

Inverse photoemission spectroscopy (IPES) has been recognized as a new and powerful technique to directly probe unoccupied electronic states of solids [5-15]. The physical basis of the spectroscopy may be viewed as the inverse of the PES process [9]. An incoming electron couples with an unoccupied state of the crystal and then decays radiatively into another lower lying unoccupied state. By monitoring the intensity of the emitted photon flux as a function of incident electron energy, one can map out features of the unoccupied states such as the density of states of conduction bands, as shown in Fig. 2-3. Similarly to the PES process, the IPES process can be followed as,

$$\hbar\omega = E_k + \phi - E_C, \tag{2. 6}$$

where $\hbar\omega$, E_k and E_C indicate the energy of the emitted photon, the energy of the incident

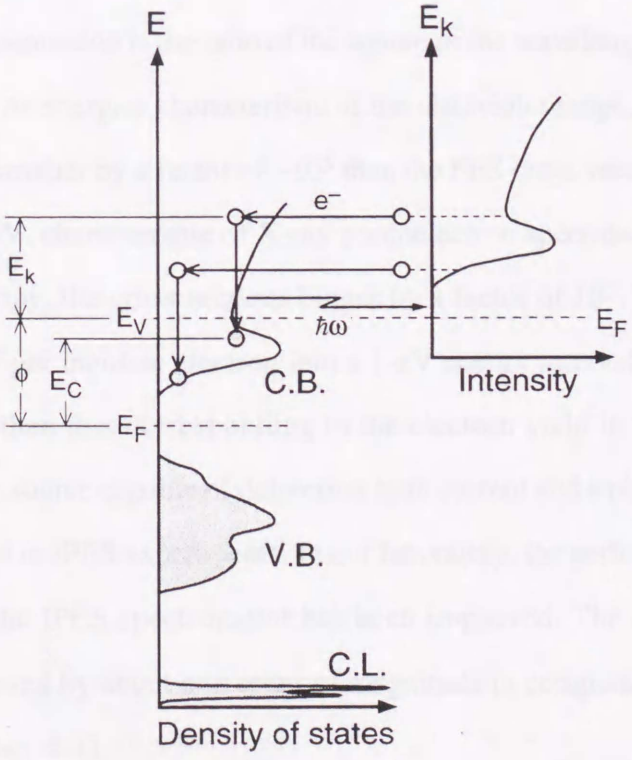

Fig. 2-3. Schematic diagram of the process of inverse-photoemission spectroscopy.

electron and the energy of the unoccupied state, respectively.

We can roughly define the IPES process as the inverse of the PES process, as described above. The relation of both processes, however, cannot be defined as a complete inverse process, because of the difference of electron number for initial and final states between both processes. Furthermore, the yield of the photoelectron or the photon between both processes is very different [9, 14]. Here, the ratio R of the cross sections for the PES and IPES process is

$$R = \left(\frac{d\sigma}{d\Omega}\right)_{\text{inverse}} \Big/ \left(\frac{d\sigma}{d\Omega}\right)_{\text{photoemission}} = \frac{\omega^2}{c^2 k^2} = q^2/k^2$$

or

$$R = \left(\frac{\lambda_{\text{electron}}}{\lambda_{\text{photon}}}\right)^2, \qquad (2.7)$$

where $d\Omega$ is the solid angle of emission. That is, the ratio of the inverse photoemission cross section to that of photoemission is the ratio of the square of the wavelength of the electron to that of the photon [9, 14]. At energies characteristic of the ultraviolet range, for instance 10 eV, the IPES cross section is smaller by a factor of ~10^5 than the PES cross section. At higher energies, of the order of 1000 eV, characteristic of X-ray photoelectron spectroscopy or bremsstrahlung isochromat spectroscopy, the cross sections bigger by a factor of 10^3. The number of emitted photons is about 10^{-8} per incident electron into a 1-eV energy interval and 2π steradians (sr), and is much smaller than that corresponding to the electron yield in photoemission [9, 14]. Therefore, an electron source capable of delivering high current and a photon detector with high sensitivity are required in IPES experiments. In our laboratory, the performance of the bandpass photon detector for the IPES spectrometer has been improved. The sensitivity of the IPES spectrometer is improved by about one order of magnitude in comparison with that before the improvement (see Chap. 4-1).

Spectrometers for IPES are classified into two types, depending on the method of photon detection, those that operate in an isochromat or fixed photon-energy mode [6, 7, 10 and 11] and

those that work in a tunable mode [12, 13]. In the measurements of the former type, photons with a specific energy are selected using a bandpass photon detector, as shown in Fig. 2-4. A spectrometer of this type fundamentally consists of an electron gun, a mirror, and a bandpass photon detector. This type introduced by Dose *et al.* [6, 7] includes a Geiger-Müller counter with a CaF_2 entrance window. Babbe *et al.*, on the other hand, presented a bandpass photon detector using a commercial photomultiplier in stead of the Geiger-Müller counter [10]. They obtained a photon detector with a full width at half maximum (FWHM) of 0.6 eV centered at the photon energy of 9.8 eV. Their detector has advantages of high stability, no dead time and

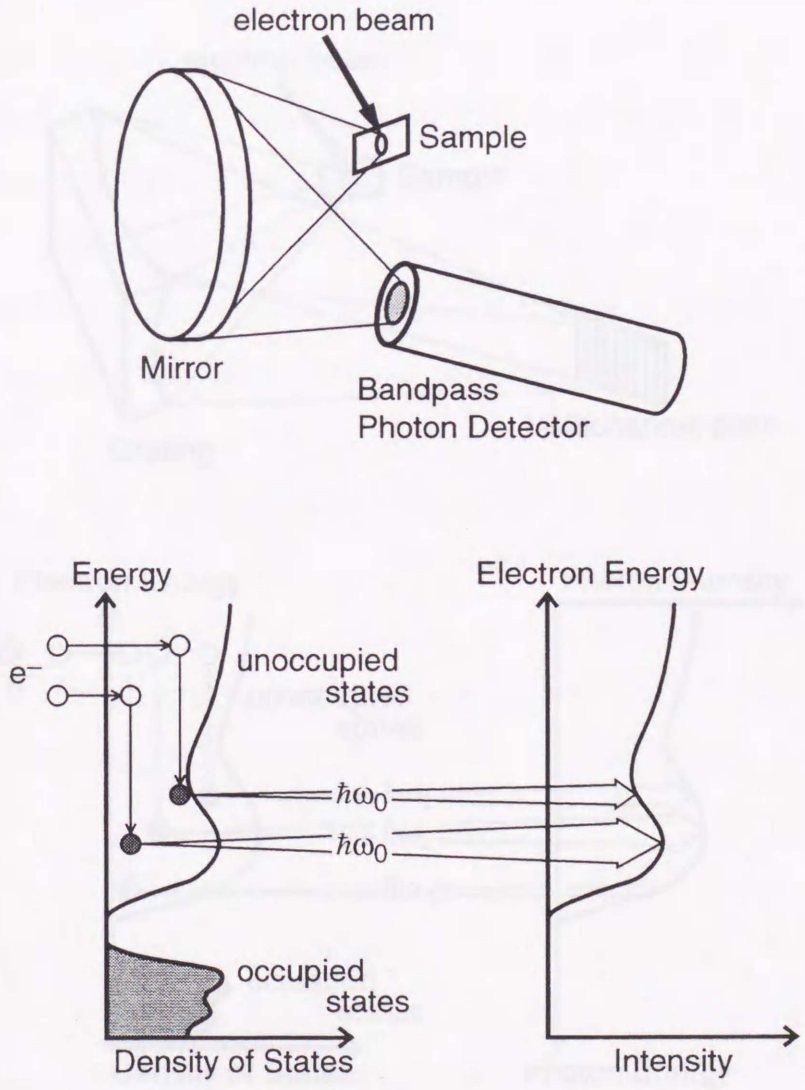

Fig. 2-4. Schematic diagram of the isochromat mode IPES.

compatibility with ultra high vacuum in comparison with the Geiger-Müller counter. Schafer *et al.* reported an improvement of the sensitivity of the photon detector by a factor of 3.5, by coating the CuBe first photocathode with a KBr film of about 700 Å thickness [11].

In the later type, photons are detected by scaning the monochromator energy, providing the energy distribution to be obtained, as shown in Fig. 2-5. A spectrometer of this type is fundamentally composed of an electron gun, a monochromator, and a two-dimensional detector. This type allows detection at different photon energies and has a higher energy resolution (18 Å). The monochromator is, however, very complex, expensive to build, and suffers from a very low counting rate [12, 13].

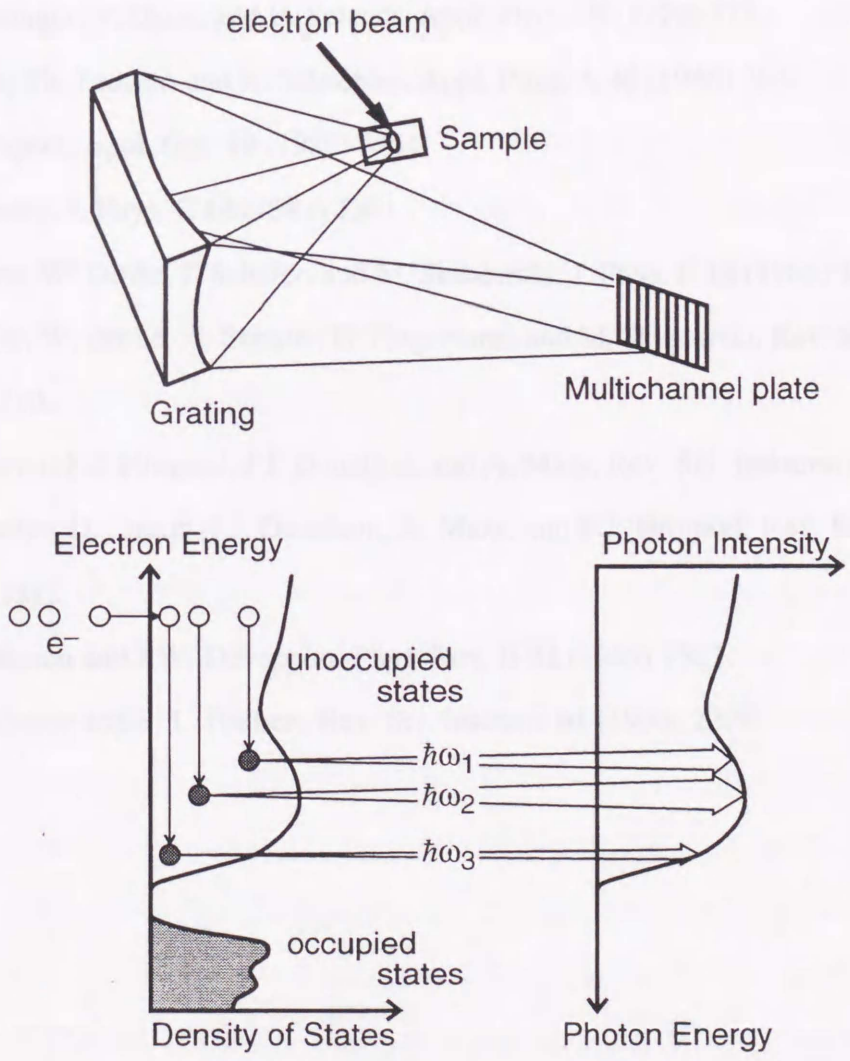

Fig. 2-5. Schematic diagram of the tunable photon energy mode IPES.

References

[1] *Photoemission in Solids I,* edited by M. Cardona and L. Ley (Springer-Verlag, Berlin, 1978).

[2] *Photoelectron Spectroscopy*, edited by S. Hüfner (Springer-Verlag, Berlin, 1995).

[3] L. Ley, M. Taniguchi, J. Ghijsen, R.L. Johnson and A. Fujimori, Phys. Rev. B **35** (1987) 2839.

[4] M. Taniguchi, A. Fujimori, M. Fujisawa, T. Mori, I. Souma and Y. Oka, Solid State Commun. **62** (1987) 431.

[5] V. Dose, Appl. Phys. **14** (1977) 117.

[6] G. Denninger, V. Dose, and H. Scheidt, Appl. Phys. **18** (1979) 375.

[7] V. Dose, Th. Fauster, and R. Schneider, Appl. Phys. A **40** (1986) 203.

[8] F.J. Himpsel, Appl. Opt. **19** (1980) 3964.

[9] J.B. Pendry, J. Phys. C **14** (1981) 1381.

[10] N. Babbe, W. Drube, I. Schäfer, and M. Skibowski, J. Phys. E **18** (1985) 158.

[11] I. Schäfer, W. Drube, M. Schuter, G. Plagemann, and M. Skibowski, Rev. Sci. Instrum. **58** (1987) 710.

[12] Th. Fauster, F.J. Himpsel, J.J. Donelson, and A. Marx, Rev. Sci. Instrum. **54** (1983) 68.

[13] Th. Fauster, D. Straub, J.J. Donelson, A. Marx, and F.J. Himpsel, Rev. Sci. Instrum. **56** (1985) 1212.

[14] P.D. Johnson and J.W. Davenport, Phys. Rev. B **31** (1985) 7521.

[15] P.D. Johnson and S. L. Hulbert, Rev. Sci. Instrum. **61** (1990) 2277.

Chapter 3.
Hot wall epitaxy (HWE)

3-1. HWE method

The HWE technique has been extensively applied to the growth of II-VI semiconductors [1–8] and DMS's such as $Cd_{1-x}Mn_xTe$ [9, 10], $Zn_{1-x}Mn_xTe$ [11] and $Zn_{1-x}Mn_xSe$ [12] epitaxial films. This technique has been also tried successfully for the growth of III-V and IV-VI compound films [13–15]. HWE is one of the thermal deposition techniques for thin films [13]. The HWE system fundamentally consists of four independent sections with heaters: a head, a wall, a source and a reservoir section. The thermal equilibrium condition is obtainable by an appropriate choice of temperatures. Each part takes a different role in growing the crystal, so it is easy to control various crystal properties. For example, the control of the stoichiometry by use of a reservoir has been reported to be an effective method of controlling the conduction carrier in PbTe or PbSnTe [13]. We present for comparison the features of the HWE method and those of a typical evaporator for thin film growth, as follows.

Figure 3-1 shows (a) a simplified schematic diagram of a HWE system with (b) that of a typical evaporating system. In conventional evaporation, the source is contained into the heated effusion cell. The substrate is also heated and is usually maintained at a distance of 5–15 cm from the top of cell. In this manner, the growth is taking place under conditions very far from thermodynamic equilibrium. Furthermore, if the deposition of compounds with different vapor pressures for each element is carried out, the composition of the vapor is not usually the same as that of the source material. On the other hand, the HWE method is considered as a vacuum film deposition technique whose main characteristics is the growth of epitaxial layers under conditions as near as possible to thermodynamic equilibrium and with a minimum loss of material. The main feature of HWE is the use of an another heated section ("hot wall" or "wall") which serves to enclose and direct the vapor from the source to the substrate. Thus, the HWE method can be considered as a variant of the vapor transport method in a closed tube, shown in

Fig. 3-2 [13].

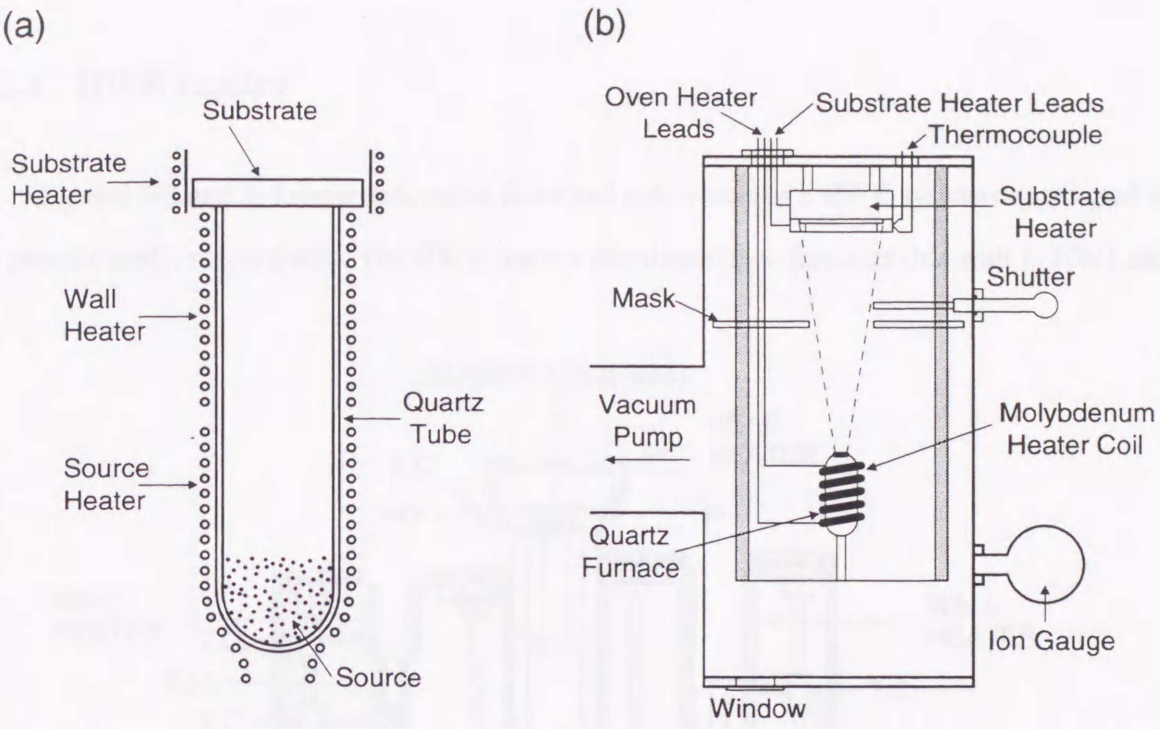

Fig. 3-1. (a) A simplified schematic diagram of a HWE system. (b) A schematic diagram of a typical evaporating system for thin film growth.

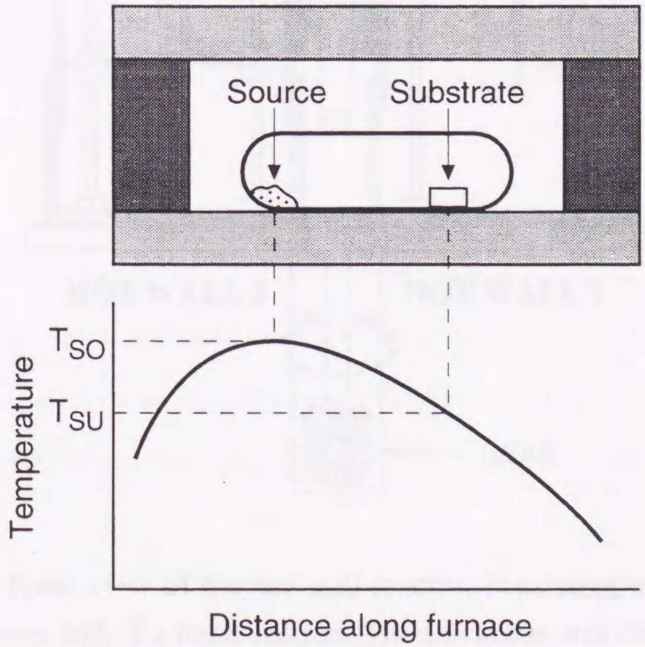

Fig. 3-2. A schematic diagram of a closed-tube vapor transport system.

3-2. Details of the HWE apparatus for DMS

3-2-1. HWE reactor

Figures 3-3 and 3-4 show schematic front and side views of a HWE system constructed in the present study, respectively. The HWE reactor consists of two furnaces (hot wall 1; HW1 and

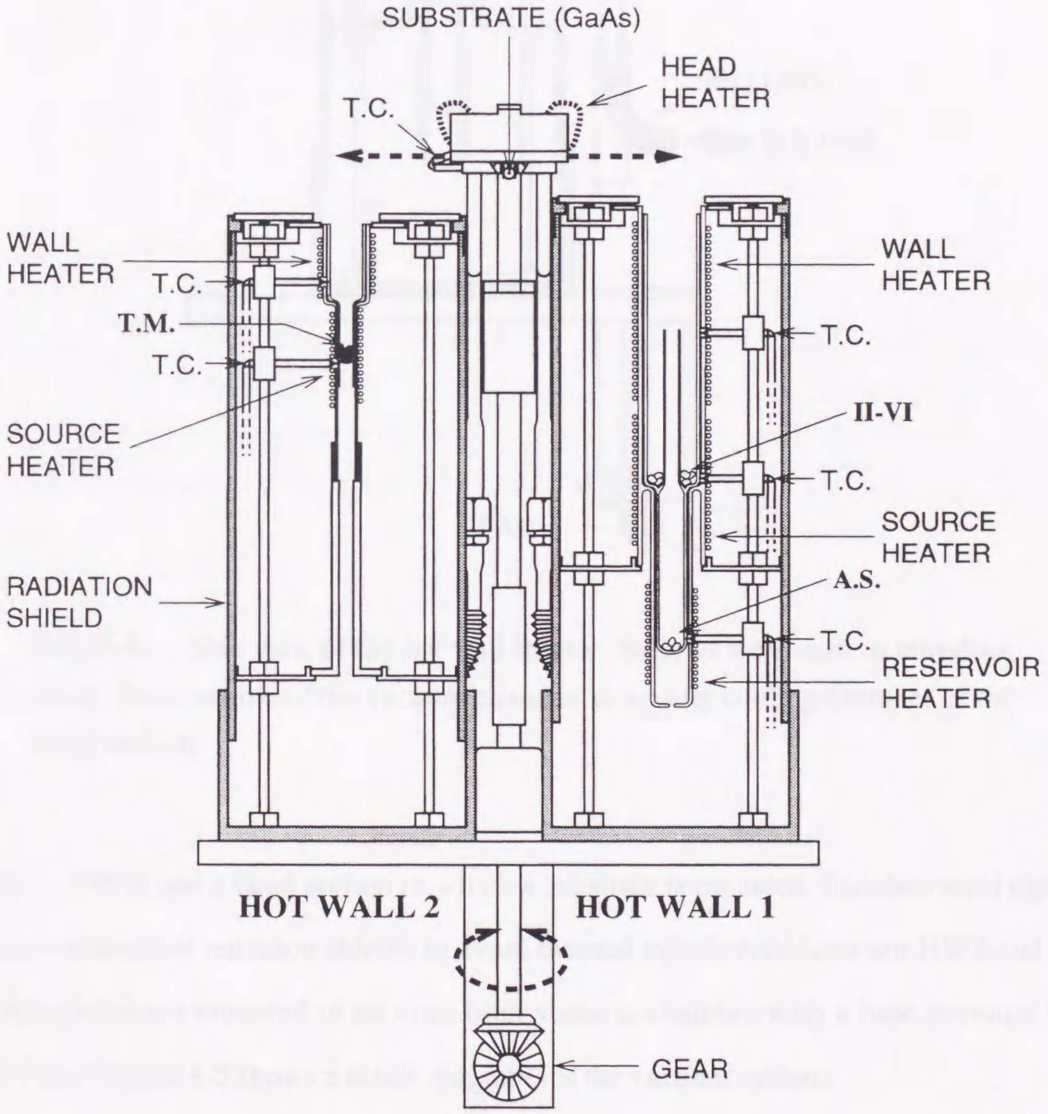

Fig. 3-3. Front view of the hot wall reactor, consisting of the HW1 and HW2 furnaces and of a head section. The thickness was controlled by the repetition number of the flip-flop motion, and x by the amount of time spent by the substrate over the HW1 and HW2 furnaces.

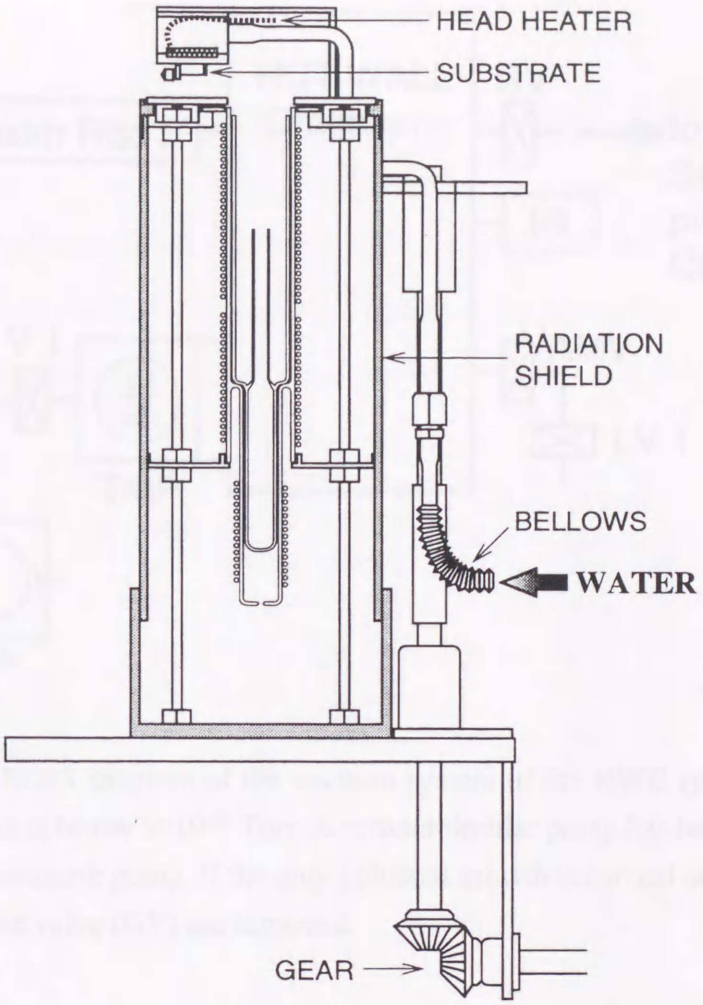

Fig. 3-4. Side view of the hot wall reactor. Bellows were used to introduce water from outside of the vacuum chamber to a water cooling chamber of the head section.

hot wall 2; HW2) and a head section in which a substrate is mounted. Stainless steel cylinders were used as thermal radiation shields to avoid thermal interference between HW1 and HW2. All components are mounted in an ultra high vacuum chamber with a base pressure below 3×10^{-9} Torr. Figure 3-5 shows a block diagram for the vacuum system.

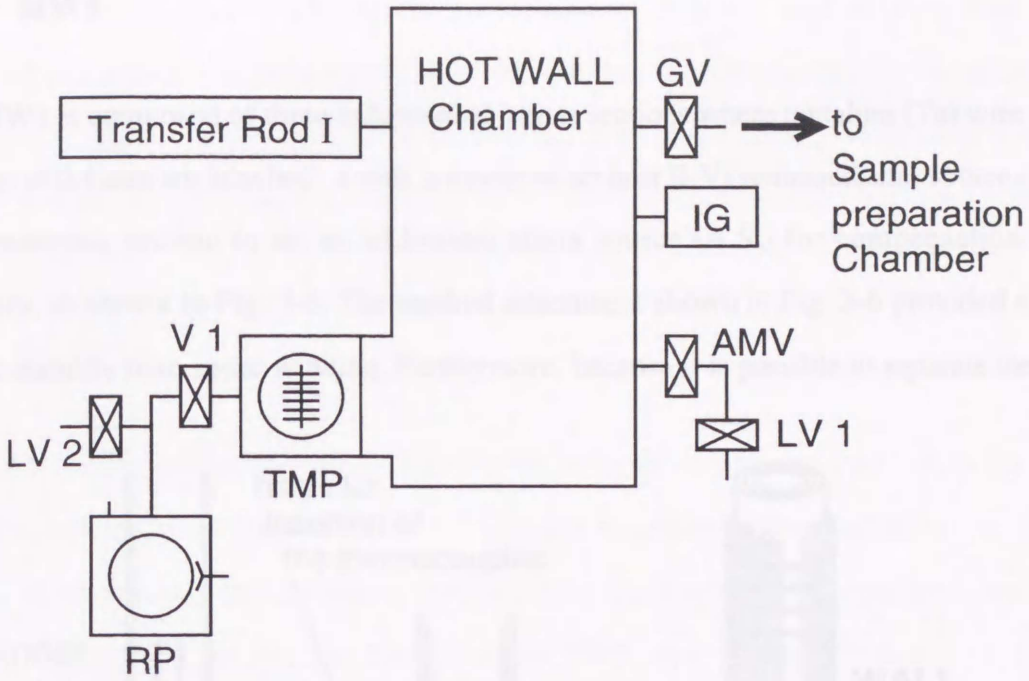

Fig. 3-5. Brock diagram of the vacuum system of the HWE system. The base pressure is below 3×10^{-9} Torr. A turbomolecular pomp has been used as the main evacuative pomp. If the only epitaxial growth is carried out, transfer rod I and gate valve (GV) are removed.

3-2-2. HW1

HW1 is composed of three independent heater sections where tantalum (Ta) wire with a diameter of 0.4 mm are attached : a wall, a source to set host II-VI semiconductor source (II-VI), and a reservoir section to set an additional anion source (A.S.) for compensation of the vacancies, as shown in Fig. 3-6. The method attachment shown in Fig. 3-6 provided a better thermal stability than spiral winding. Furthermore, because it is possible to separate the HW1

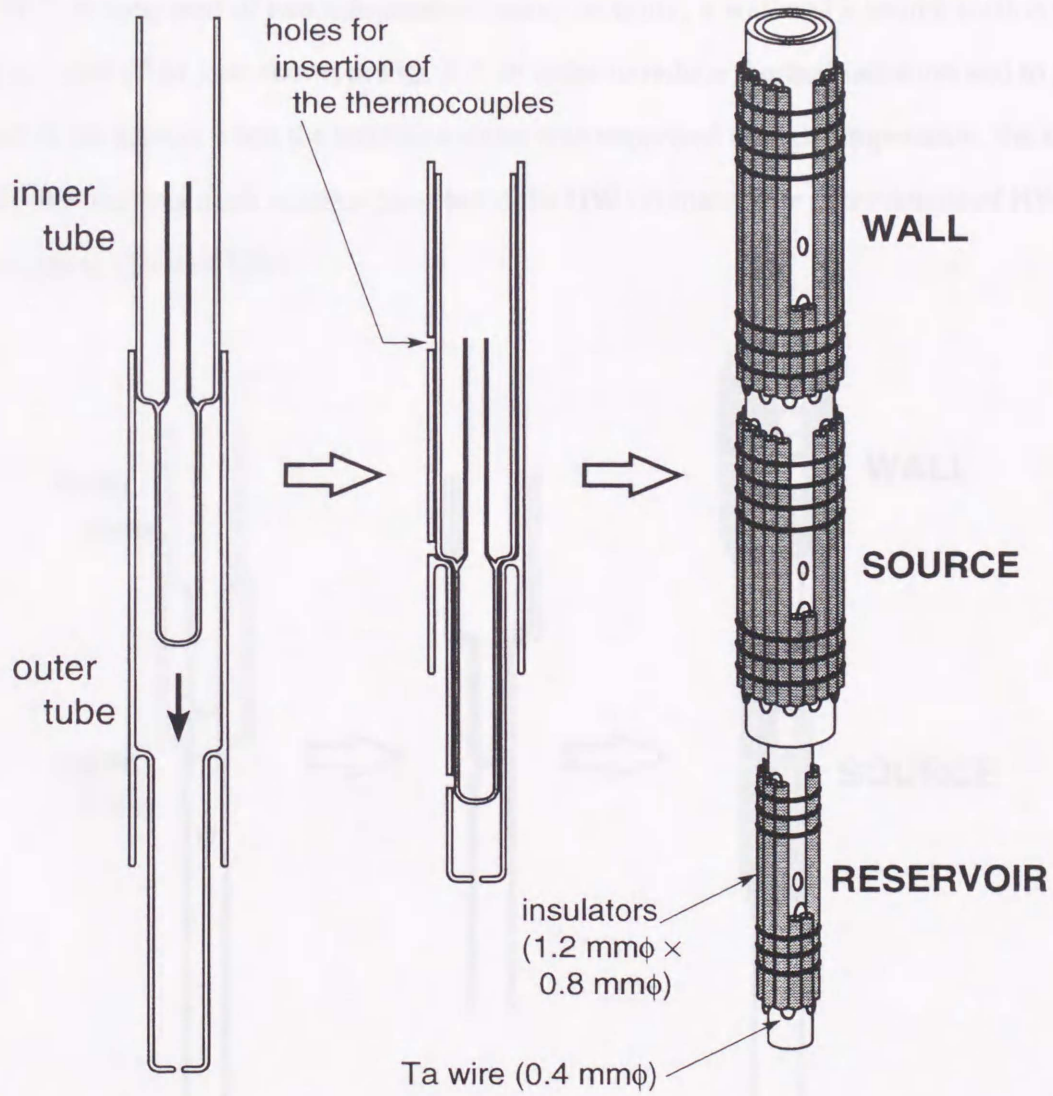

Fig. 3-6. Schematic illustration of the HW1 furnace, consisting of a wall, a source and a reservoir section. Tantalum wire passed though insulator tubes was attached to the outer quartz tube. The height of the outer quartz tube is about 220 mm.

furnace into an outer quartz tube, where the heaters are attached, and an inner quartz tube containing the source materials, source materials can easily be exchanged by using the inner tube as a cartridge. Alumel-chromel thermocouples for each section were independently directed into narrow gaps with a width of about 0.5 mm between the outer and inner tube.

3-2-3. HW2

HW2 is composed of two independent heater sections : a wall and a source section to set transition metal (T.M.), as shown in Fig. 3-7. In order to reduce thermal radiation and to avoid overload of the heaters when the transition metal was vaporized at high temperature, the size of the HW2 furnace was made smaller than that of the HW1 furnace. The other details of HW2 are almost same as those of HW1.

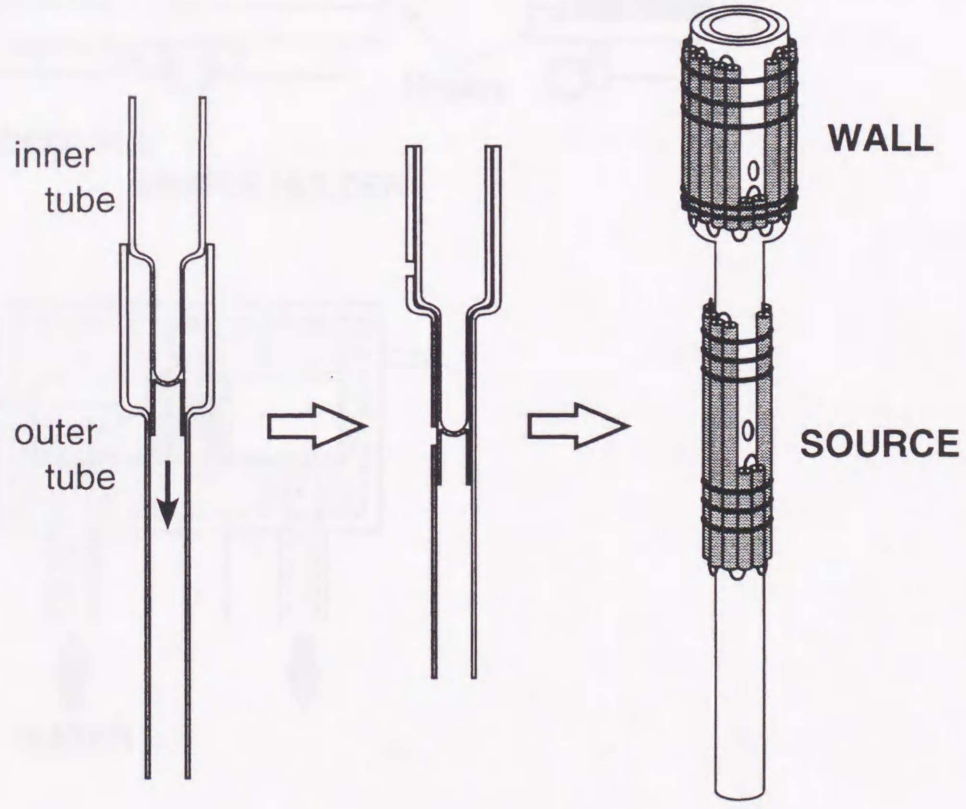

Fig. 3-7. Schematic illustration of the HW2 furnace, consisting of a wall and a source section. The size of HW2 furnace was made smaller than that of HW1 furnace. The height of the outer quartz tube is about 110 mm.

3-2-4. Head section

Figure 3-8 shows schematically the head section. It consists of a heater using tantalum wire and a water cooling chamber to avoid interference of thermal radiation from HW1 and HW2, and to provide thermal stability. In order to improve thermal efficiency, blocks under the heater have been made of Cu or CuBe. Two bellows were used to introduce water from the outside of the vacuum chamber to the water cooling chamber, as shown in Fig. 3-4. An alumel-

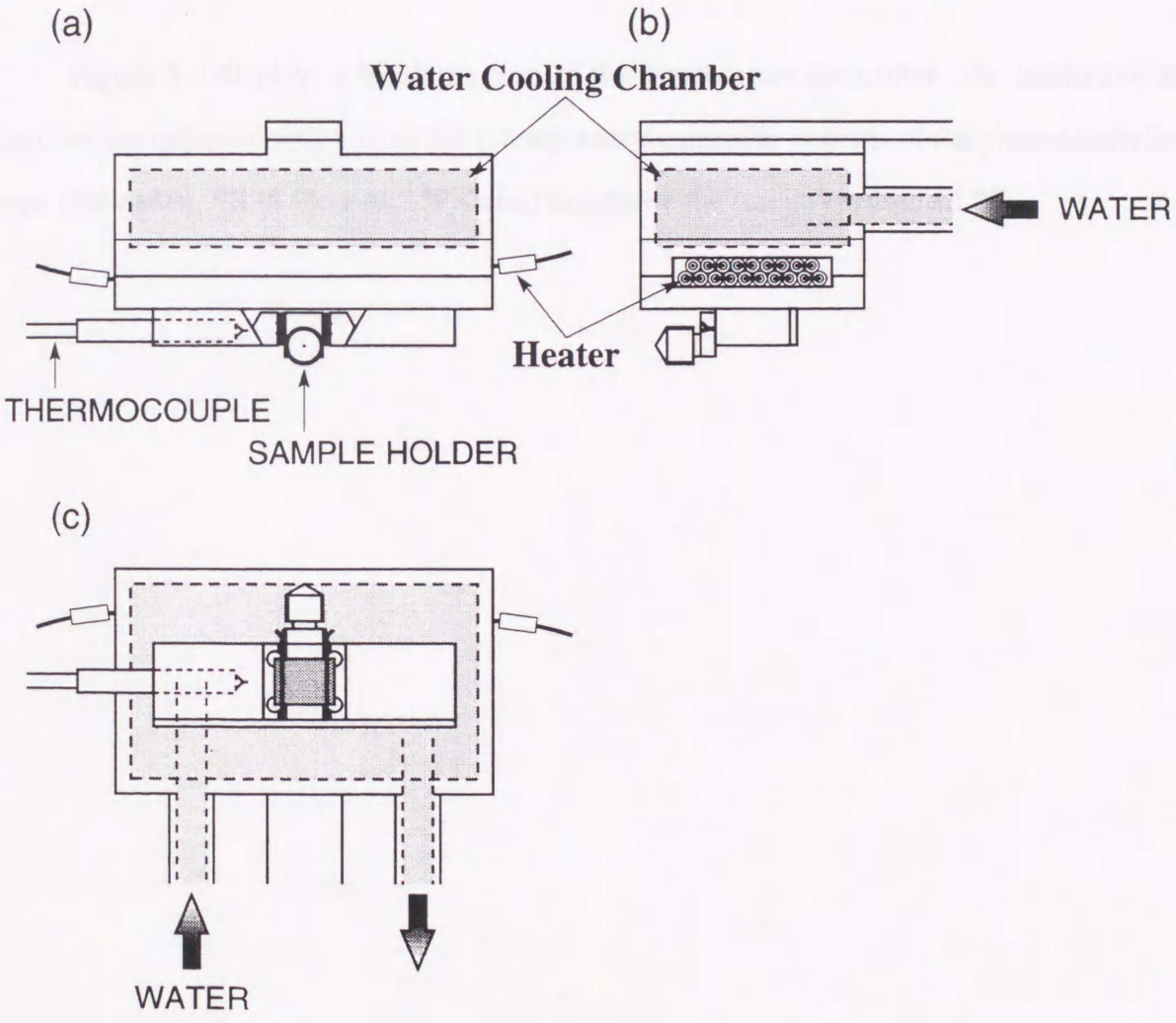

Fig. 3-8. Schematic illustration of the head section consisting of a heater and a water cooling chamber : (a) front view, (b) right side view and (c) base view. Water is introduced through the bellows from the outside of the vacuum chamber.

chromel thermocouple was inserted in a hole of the substrate-holding block. The head section can be moved in the horizontal direction between HW1 and HW2 by using a stepping motor controlled by a microcomputer. Thus, a flip-flop method [9, 14], moving the head section from HW1 to HW2, is employed to vary thickness and concentration (x) of DMS films. The thickness is controlled by the repetition number of the flip-flop motion, and x by the amount of time spent by the substrate over the HW1 and HW2 furnaces.

3-2-5. Temperature control

Figure 3-9 displays a block diagram of the temperature controller. The heaters of all sections are independently connected to temperature controller systems of the phase-controlled type (Shimaden, SR35 and PAC15P series) to achieve the stability within ±1 °C.

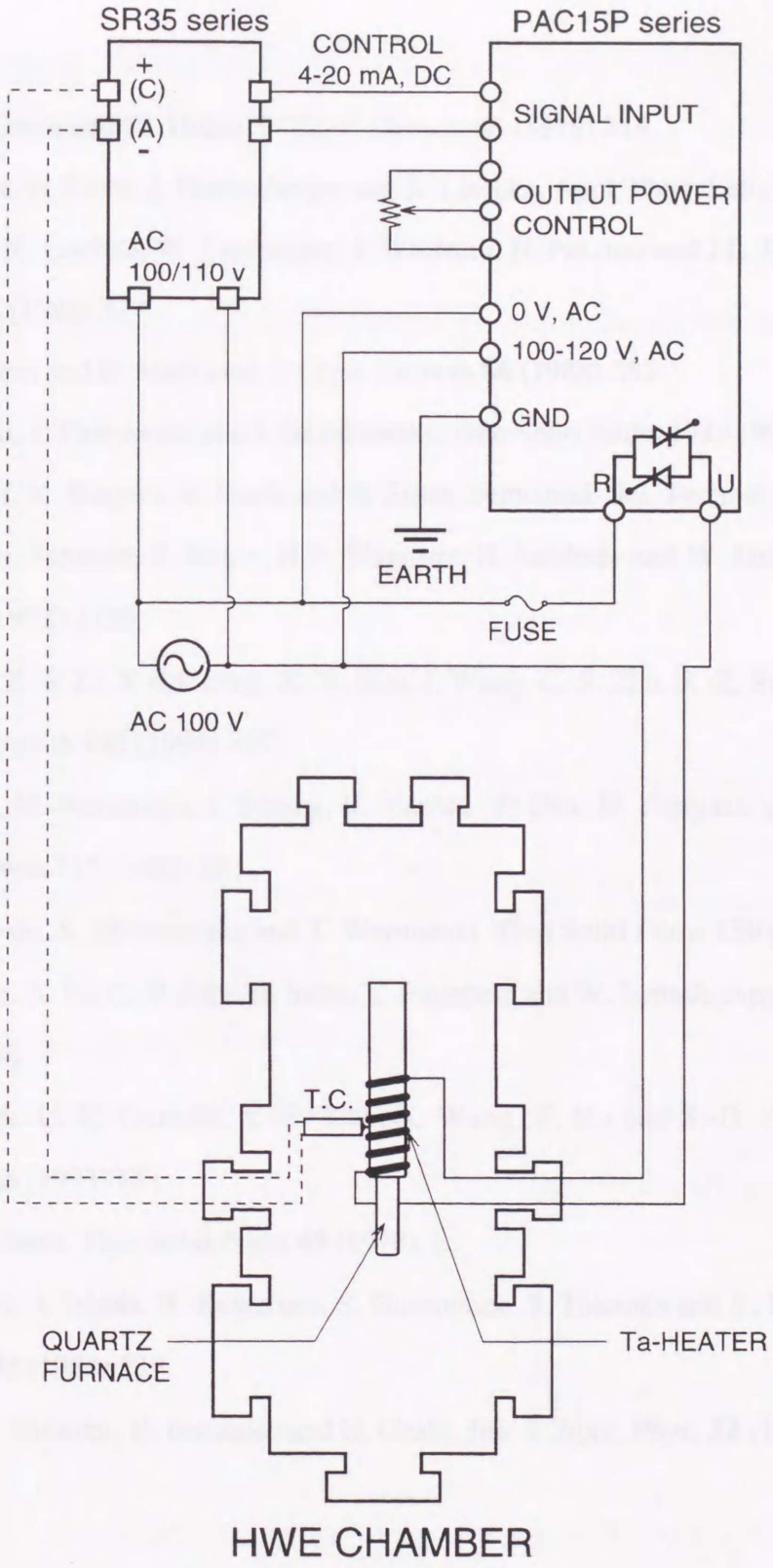

Fig. 3-9. A block diagram of temperature control system.

References

[1] A. Lopez-Otero and W. Huber, J. Cryst. Growth **45** (1978) 214.

[2] D. Schikora, H. Sitter, J. Humenberger and K. Lischka, Appl. Phys. Lett. **48** (1986) 1276.

[3] H. Shitter, K. Lischka, W. Faschinger, J. Wolfrum, H. Pascher and J.L. Pautrat, J. Cryst. Growth **86** (1988) 377.

[4] R. Korenstein and B. MacLeod, J. Cryst. Growth **86** (1988) 382.

[5] A. Rogalski, J. Piotrowski and J. Gronkowski, Thin Solid Films **191** (1990) 239.

[6] E. Abramof, K. Hingerl, A. Pesek and H. Sitter, Semicond. Sci. Technol. **6** (1991) A80.

[7] P. Link, Th. Schmidt, S. Bauer, H.P. Wangner, H. Leiderer and W. Gebhardt, J. Appl. Phys. **72** (1992) 3730.

[8] W.-Z. Cai, Z.-S. Li, X.-M. Ding, X.-Y. Hou, J. Wang, C.-S. Zhu, R.-Z. Su amd X. Wang, J. Cryst. Growth **142** (1994) 397.

[9] K. Suzuki, M. Nakamura, I. Souma, K. Yanata, Y. Oka, H. Fujiyasu and H. Noma, J. Cryst. Growth **117** (1992) 881.

[10] I. Miotkowski, S. Miotkowska and T. Warminski, Thin Solid Films **150** (1987) 337.

[11] E. Abramof, A. Pesek, P. Juza, H. Sitter, T. Fromherz and W. Jantsch, Appl. Phys. Lett. **60** (1992) 2368.

[12] J. Wang, A.-U.-H. Qureshi, Y.-S. Tian, X. Wang, Y. Hu and S.-D. Zheng, J. Cryst. Growth **126** (1993) 651.

[13] A. Lopez-Otero, Thin Solid Films **49** (1978) 3.

[14] H. Fujiyasu, A. Ishida, H. Kuwabara, S. Shimomura, S. Takaoka and K. Murase, Surface Science **142** (1984) 579.

[15] M. Iida, T. Shimizu, H. Enomoto and H. Ozaki, Jpn. J. Appl. Phys. **32** (1993) 4449.

Chapter 4.
Experimental details I: ultraviolet photoemission and inverse-photoemission study

4-1. Ultraviolet photoemission and inverse-photoemission spectrometers

Figure 4-1 shows schematically the apparatus used in the present experiments. The UPS spectrometer is composed of a He discharge lamp ($\hbar\omega$ = 21.2 and 40.8 eV) and a double-stage cylindrical-mirror analyzer (DCMA) to obtain angle-integrated spectra. The energy resolution

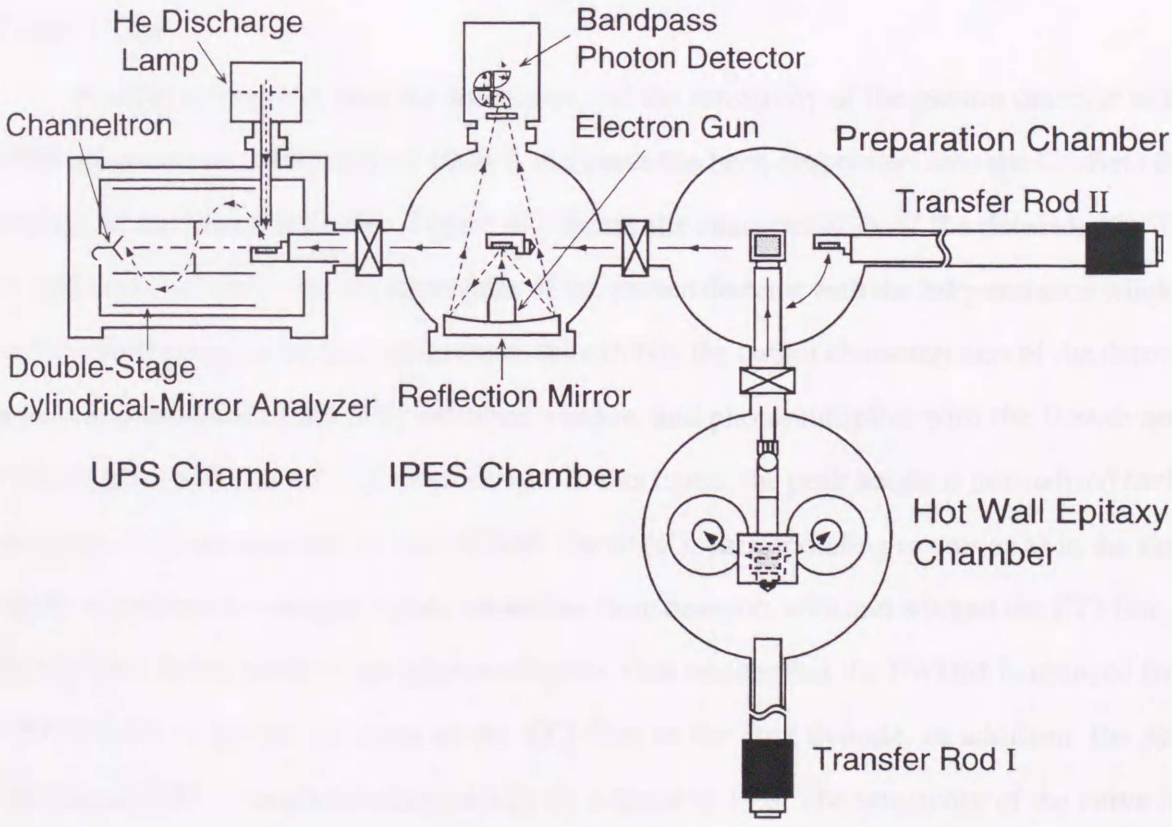

Fig. 4-1. A schematic illustration of the UPS and IPES spectrometer. The UPS spectrometer is composed of a He discharge lamp and a double-stage cylindrical-mirror analyzer to obtain angle-integrated spectra. The IPES spectrometer consists of an electron gun, an Al reflection mirror coated with a MgF_2 film, and the bandpass photon detector.

was set to be 0.2 eV by setting the pass energy of DCMA at 16 eV. The working pressure of the UPS chamber was 3×10^{-9} Torr under the operation of the discharge lamp, though the base pressure was 4×10^{-10} Torr.

The IPES spectrometer connected with the UPS apparatus consists of an electron gun of the Erdman-Zipf type [1] with a BaO cathode, an Al reflection mirror coated with a MgF_2 film of 200 Å thickness, and the bandpass photon detector with a pure SrF_2 crystal entrance window of 1-mm thickness (high-cut filter) and a commercial Cu-BeO photomultiplier having a sensitive cathode area of 12×10 mm^2 (low-cut filter) (Hamamatsu R-595: 0–5 kV). Light emitted from the sample is focused onto the first dynode of the photomultiplier, after passing through the SrF_2 entrance window. The acceptance angle of the light is about 0.8π sr. All components are mounted in an ultra high vacuum chamber under the base pressure below 7×10^{-11} Torr.

In order to improve both the resolution and the sensitivity of the photon detector of the IPES spectrometer, a KCl film of 1000-Å thickness has been evaporated onto the Cu-BeO first dynode of the photomultiplier. Figure 4-2 shows the characteristics of the detector [2]. The dashed curve (a) shows the characteristics of the photon detector with the SrF_2 entrance window and Cu-BeO photomultiplier, while curve (b) exhibits the output characteristics of the detector with a combination of the SrF_2 entrance window and photomultiplier with the first dynode coated with a KCl film of 1000-Å thickness. In this figure, the peak height is normalized to that of curve (a) for comparison of the FWHM. Curve (a'), corresponding to curve (a) in the same figure, is redrawn to compare output intensities from detectors with and without the KCl film on the Cu-BeO first dynode of the photomultiplier. One notices that the FWHM is reduced from 0.69 to 0.47 eV by the presence of the KCl film on the first dynode. In addition, the peak intensity at 9.43 eV increases dramatically by a factor of 13.6. The sensitivity of the curve (b), defined as the signal intensity integrated over the photon energy range form 7 to 10 eV, is by about one order of magnitude higher than that of the curve (a'). The overall resolution of the IPES spectrometer evaluated from the convolution of the energy spread of the incident electron beam (typically 0.25 eV) and the characteristic of the photon detector (FWHM = 0.47 eV) is

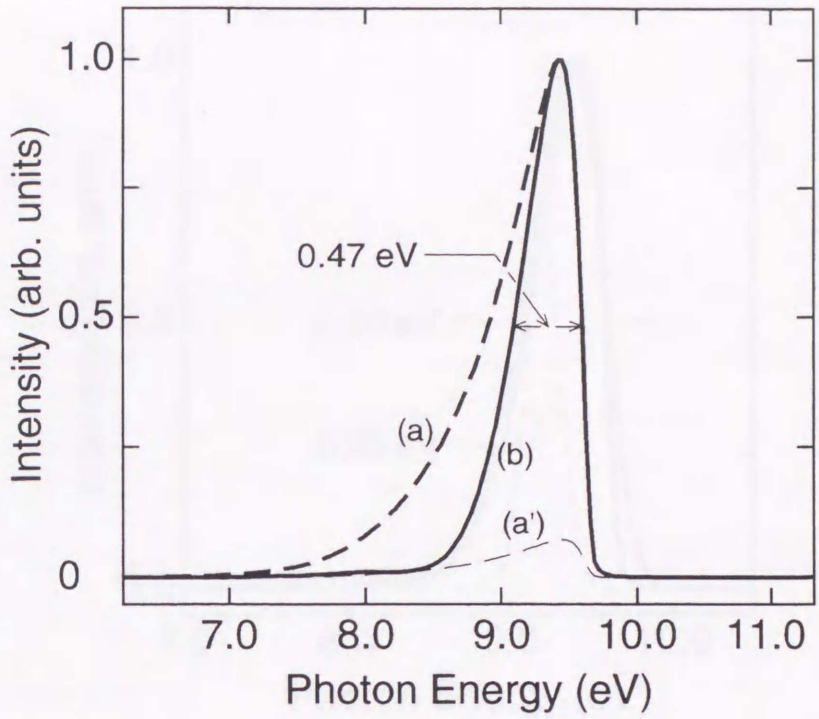

Fig. 4-2. Characteristic curves of the bandpass photon detectors without (a and a') and with the KCl film (b) on the Cu-BeO first dynode of the photomultiplier. Peak heights of curves (a) and (a') are adjusted to each other for comparison of the FWHM.

0.56 eV, as shown in Fig. 4-3. The typical counting rate for unoccupied states of polycrystalline Au near the Fermi level is 10^2–10^3 counts / (μA·s) at acceptance angle of 0.8π sr for operation voltages of the photomultiplier in the range of 2.5–4 kV. Details of the characterization of the new bandpass photon detector have been described in Refs. 3 and 4.

Energy calibrations of the IPES and UPS spectra were experimentally made using the spectra of a fresh film of polycrystalline Au [4]. The position of the Fermi level in the band gap of semiconductors depends significantly upon the individual samples, while energies of UPS and IPES spectra can be defined experimentally with respect to the Fermi level. The connection of the UPS and IPES spectra at the Fermi level by means of *in situ* measurements for the same sample surface is essential to evaluate accurately the energy separation between the peak in the UPS spectrum and that in the IPES spectrum.

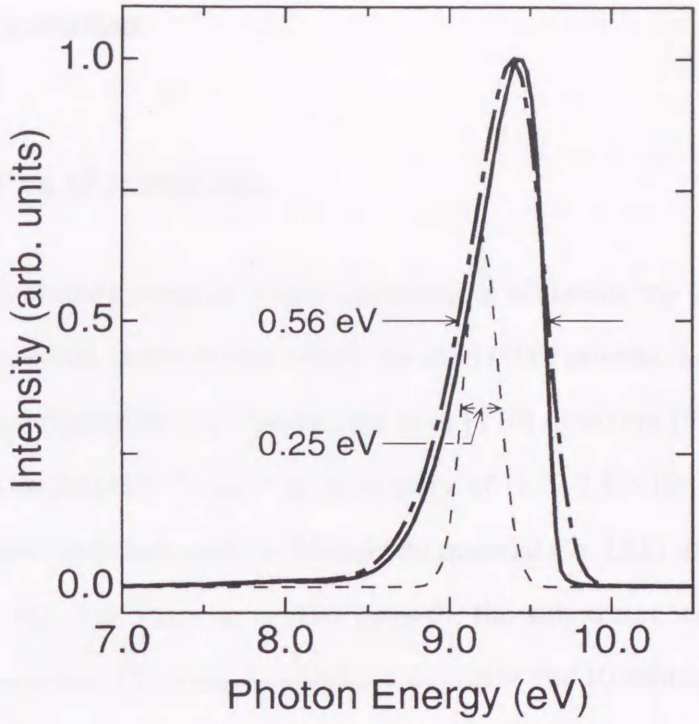

Fig. 4-3. Estimation of the overall energy resolution of the IPES apparatus by a convolution of the FWHM of the bandpass photon detector (0.47 eV: solid curve) and an energy spread of the electron beam (0.25 eV: dashed curve). The overall resolution is evaluated to be 0.56 eV (dash-dotted curve).

All measurements of IPES and UPS spectra were carried out at room temperature. The energy was referred to the VBM determined by extrapolating the steep leading edge of the highest valence-band peak to the baseline.

4-2. Sample preparation

4-2-1. Preparation of substrates

The choice of substrate material is very important in achieving the growth of the highest quality single-phase crystal. In the present study, we used (100) oriented Si-doped *n*-type GaAs substrates with a misorientation of 2° toward the next [110] direction [5], and with impurity concentration of $(1.0–2.5)\times10^{-18}$ cm^{-3} or resistivity of $(1.5–2.8)\times10^{-3}$ Ω·cm. We cut our substrates from commercial GaAs wafers (Mitsubishi material Co. Ltd.) in a typical size of 6×8 mm^2, as shown in Fig. 4-4. Prior to crystal growth, the substrates were prepared by the following etching process : (1) trichloroethylene degrease for 10 minutes ; (2) acetone and

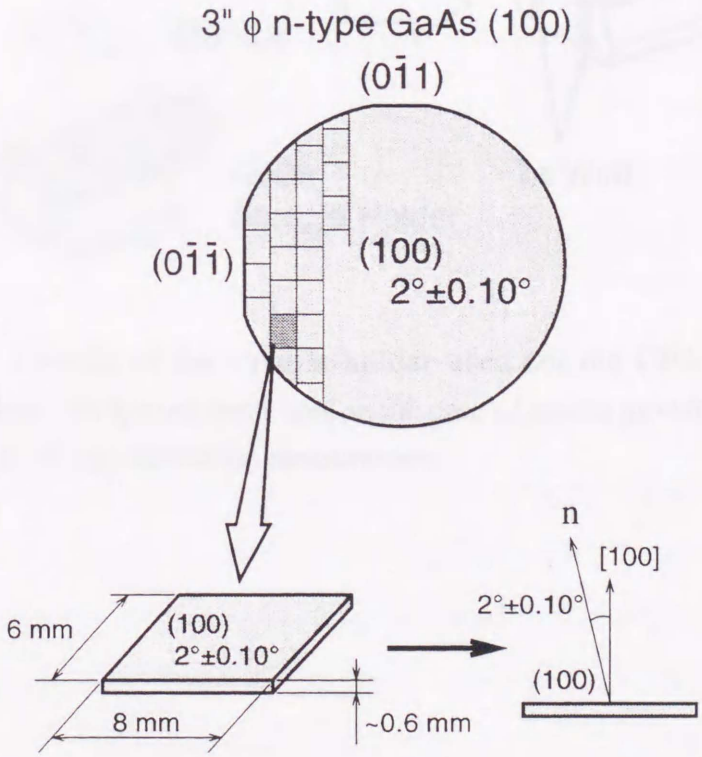

Fig. 4-4. (100)-oriented Si-doped *n*-type GaAs substrate for the growth of $Cd_{1-x}Mn_xTe$ film by HWE. A GaAs wafer with a diameter of 3 inches was cut in a typical size of 6×8 mm^2.

ethanol rinse for 10 minutes ; (3) $H_2SO_4/H_2O_2/H_2O$ (5:1:1) etch for 1 minute ; (4) bidistilled H_2O rinse ; (5) storage in ethanol.

Figure 4-5 shows details of the sample holder for the UPS and IPES measurements. Special care was paid to achieve reliable Ohmic contacts, which were alloyed onto the back of the substrate using Sn to avoid uncontrolled voltage drop at the GaAs substrate – Mo foil interface. The Mo foil was used to prevent reaction between the GaAs substrate and CuBe sample-holder during the heating process made at 580 °C for 2 min and 600 °C for 30 min, for the crystal growth of $Cd_{1-x}Mn_xTe$ ($0 \leq x \leq 0.7$) and that of zinc-blende MnTe, respectively.

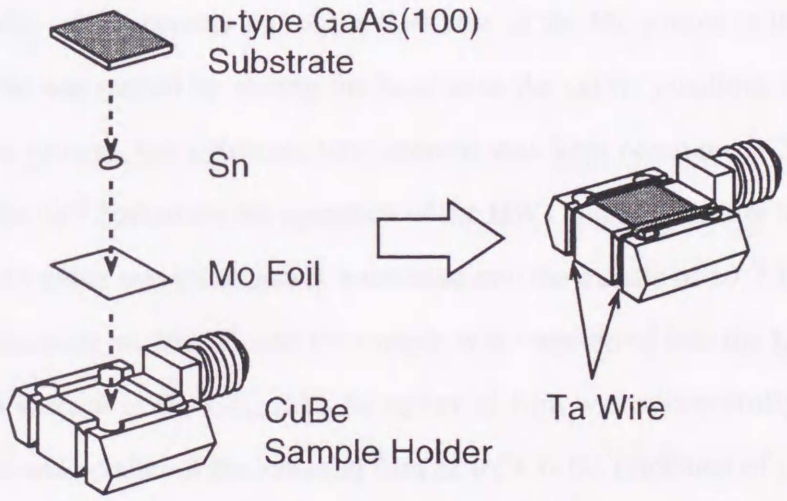

Fig. 4-5. Details of the sample holder used for the UPS and IPES measurements. Sn has not been used in the case of crystal growth of sample used only for X-ray diffraction measurement.

4-2-2. Epitaxial growth of thin films for ultraviolet photoemission and inverse-photoemission experiments

(1) $Cd_{1-x}Mn_xTe$ ($0 \leq x \leq 0.7$)

CdTe, Te, and Mn source materials were set into the source and reservoir section of HW1, and the source section of HW2. The etched substrate loaded at the head section in the vacuum chamber was preheated at 580 °C for 2 min to remove the oxide layer. After the preheating process, the temperature of the substrate dropped down to 300 °C, and CdTe and Mn source temperatures were increased to 520 and 860 °C, respectively. The Te reservoir temperature was varied between 350 and 365 °C depending of x. After confirming the temperature stability of all sections and of the flow rate of the Mn source in the range of ~0.1 Å/s, crystal growth was started by sliding the head onto the center positions of the HW1 and HW2. During the growth, the substrate temperature was kept constant at 300 °C, and the vacuum was $(1–5)\times10^{-8}$ Torr under the operation of the HW1 and HW2. After the growth of the film, the vacuum chamber was immediately evacuated into the middle of 10^{-9} Torr, keeping the substrate temperature above 250 °C, and the sample was transferred into the UPS chamber. In this way, a clean surface of the $Cd_{1-x}Mn_xTe$ epitaxial film was successfully obtained. The crystal orientation and x-value of the epitaxial film as well as the thickness of (0.5–1) μm were checked by X-ray diffraction (XRD) [6].

In comparison with UPS spectra, IPES spectra are much more sensitive to electrostatic charging effect. To avoid such an effect, the thickness of the film was reduced by decreasing only the repetition number of the flip-flop motion without changing any other parameters in the growth condition for the thick $Cd_{1-x}Mn_xTe(100)$ film until the IPES spectrum exhibited no electrostatic charging effect. The thickness of samples used for the UPS and IPES experiments was measured using a surface profiler (High precision optical stylus surface measuring instrument, Kosaka Ltd.). The typical value of the thickness was about 300 Å.

In general, CdTe epitaxial films can grow on GaAs(100) substrates with (100) and (111) orientation, depending on the growth conditions [7], and often mixed films are obtained. In the present experiments, it can reasonably be assumed that the thin films used for the UPS and IPES

measurements would be (100)-oriented films, because $Cd_{1-x}Mn_xTe$ epitaxial films with the (100) orientation grew steadily under suitable parameters above mentioned. The UPS spectra for thin $Cd_{1-x}Mn_xTe$ films, which exhibited no electrostatic charging effect in the IPES measurements, were fully consistent with those for the thick $Cd_{1-x}Mn_xTe(100)$ films. The UPS spectra for thick $Cd_{1-x}Mn_xTe(100)$ films thick enough for determining the orientation by XRD were free from the electrostatic charging effect and consistent with those for bulk alloys.

Residual strain is known to be important and affect, for example, the band-gap energy of CdTe. The amount of the strain-induced change in the band-gap energy is, however, estimated to be ~10 meV [8, 9] and negligible in comparison with the energy resolution of 0.2 and 0.56 eV in the UPS and IPES measurements, respectively.

The x-values of the thin epitaxial films were again evaluated by X-ray photoemission spectroscopy (XPS; ESCA 5400, Perkin Elmer) using integrated emission-intensities of the Cd 3*d*, Mn 2*p* and Te 3*d* core levels of the epitaxial films, after the UPS and IPES measurements. The XPS spectra from bulk $Cd_{1-x}Mn_xTe$ specimens were used as a reference.

(2) zinc-blende MnTe ($x = 1$)

Zinc-blende MnTe had been considered to be a hypothetical compound. Recently, metastable zinc-blende MnTe epitaxial films have been fabricated on substrates or buffer layers with zinc-blende structure, by using thermal nonequilibrium growth techniques like molecular beam epitaxy (MBE) [10–16] and ionized cluster beam (ICB) deposition [17, 18]. It is noted that the stable phase of MnTe is of a NiAs-type structure, and that HWE is a thermodynamic equilibrium growth technique [19]. In order to overcome this difficulty, the growth of zinc-blende MnTe epitaxial films using the HWE system was carried out as follows.

For the growth of zinc-blende MnTe, we used the HW2 furnace and not the HW1 furnace. NiAs-type MnTe source material was set into the source section of HW2. The etched substrate loaded at the head section in the vacuum chamber was preheated at 600 °C for 30 min to remove the oxide layer. After the preheating process, the temperature of the substrate dropped until 250–320 °C, and the NiAs-type MnTe source was heated up to 860 °C, while the wall section of

HW2 was not heated. In this way, the growth was carried out under conditions out of thermodynamic equilibrium, because of the increased temperature between the head and source of HW2. After confirming the stability of the furnace temperature of all sections (except for HW1) and of the flow rate of the MnTe source in the range of ~0.3 Å/s, crystal growth was started by sliding the head to the center positions of HW2. During the growth, the substrate temperature was kept constant at 250–320 °C, and the vacuum was 2×10^{-8} Torr under the operation of the HW2. After the growth of the film, the sample was immediately transferred into the IPES chamber. In this way, a clean surface of the zinc-blende MnTe epitaxial film was successfully obtained. The crystal orientation of the epitaxial film with a thickness of about 3000 Å was checked by XRD.

To avoid electrostatic charging effects in the UPS and, especially, IPES measurements, the thickness of film was reduced by decreasing only the repetition number of the flip-flop motion without changing any other parameters in the growth condition for the thick zinc-blende MnTe film until the IPES spectrum exhibited no electrostatic charging effect anymore. The typical value of the thickness was about 100 Å.

In general, zinc-blende MnTe epitaxial films can grow on GaAs(100) substrates with (100) and (111) orientation, depending on the growth conditions [14, 15]. In the present experiments, we confirmed the orientation of the thin films used for the UPS and IPES measurements using low-energy electron diffraction (LEED) fixed in the IPES chamber, as shown in Fig. 4-6.

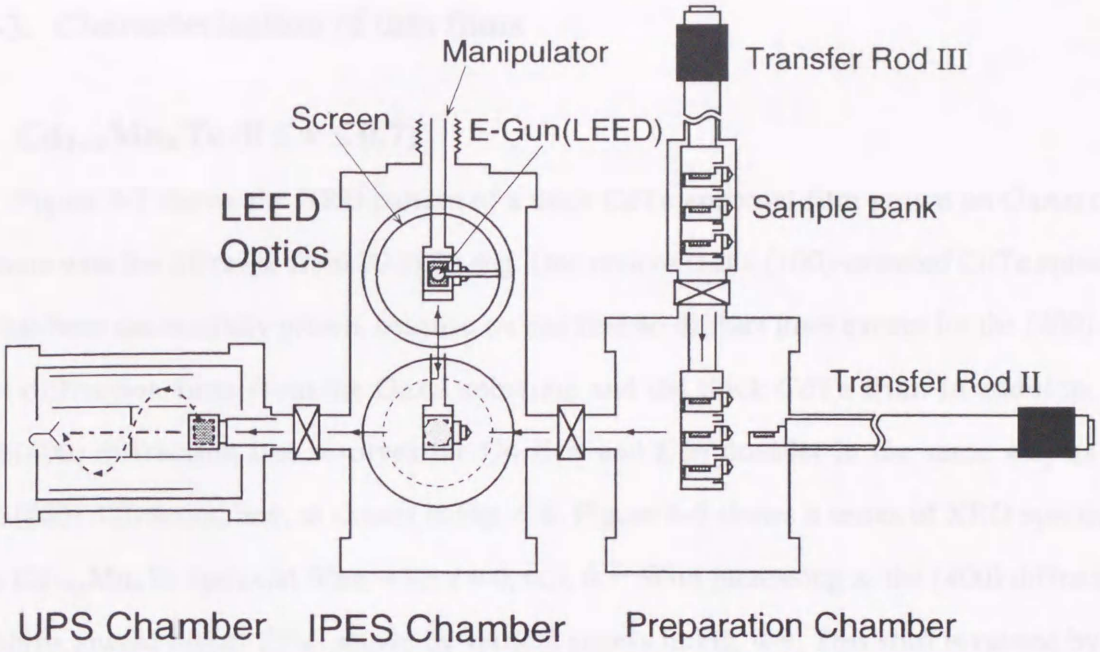

Fig. 4-6. Schematic illustration of UPS, IPES and LEED apparatuses used for the experiments of zinc-blende MnTe epitaxial film. This illustration is a cross section of the line connected form UPS to preparation chambers in Fig. 4-1.

4-2-3. Characterization of thin films

(1) $Cd_{1-x}Mn_xTe$ ($0 \leq x \leq 0.7$)

Figure 4-7 shows the XRD pattern of a thick CdTe epitaxial film grown on GaAs(100) substrate with the 2θ range from 20 to 80 deg. One notices that a (100)-oriented CdTe epitaxial film has been successfully grown, because we can find no diffract lines except for the (400) and (200) diffraction lines from the GaAs substrate and the thick CdTe film. In addition, the CdTe(400) diffraction line resolves the Cu $K\alpha_1$ and $K\alpha_2$ doublet in the same way as the GaAs(400) diffraction line, as shown in Fig. 4-8. Figure 4-9 shows a series of XRD spectra of thick $Cd_{1-x}Mn_xTe$ epitaxial films with $x = 0$, 0.3, 0.7. With increasing x, the (400) diffraction line shifts toward higher 2θ as shown by vertical arrows in Fig. 4-9. This shift is caused by the decrease of lattice constant with x [6].

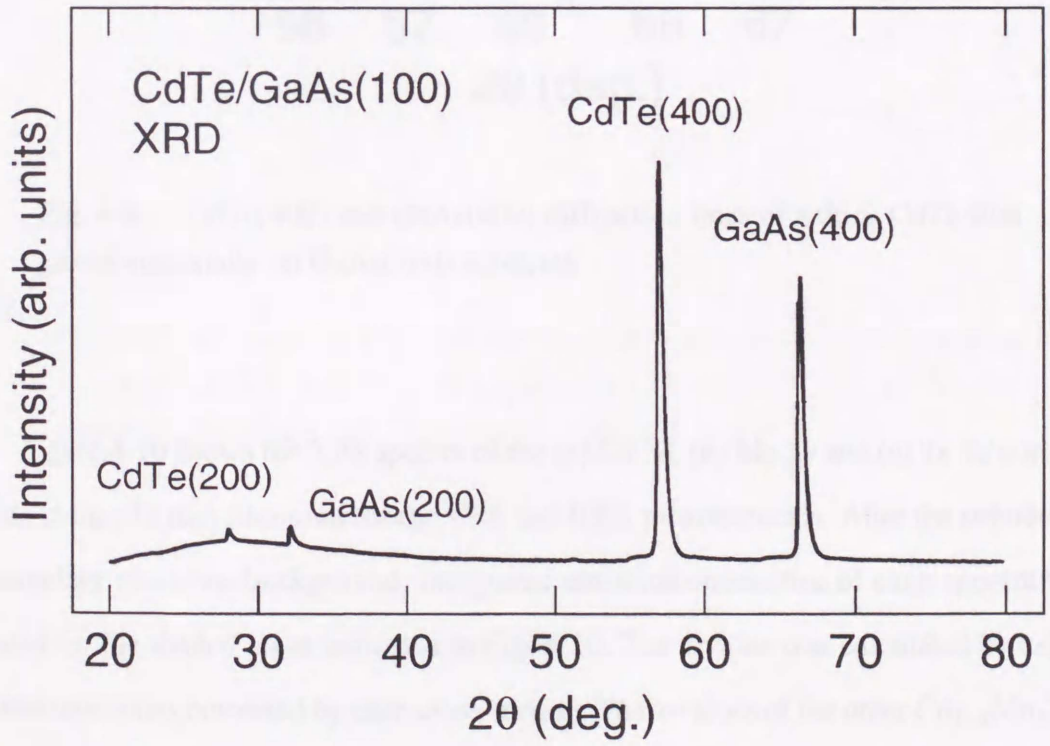

Fig. 4-7. θ-2θ XRD pattern of thick CdTe film grown epitaxially on GaAs(100) substrate.

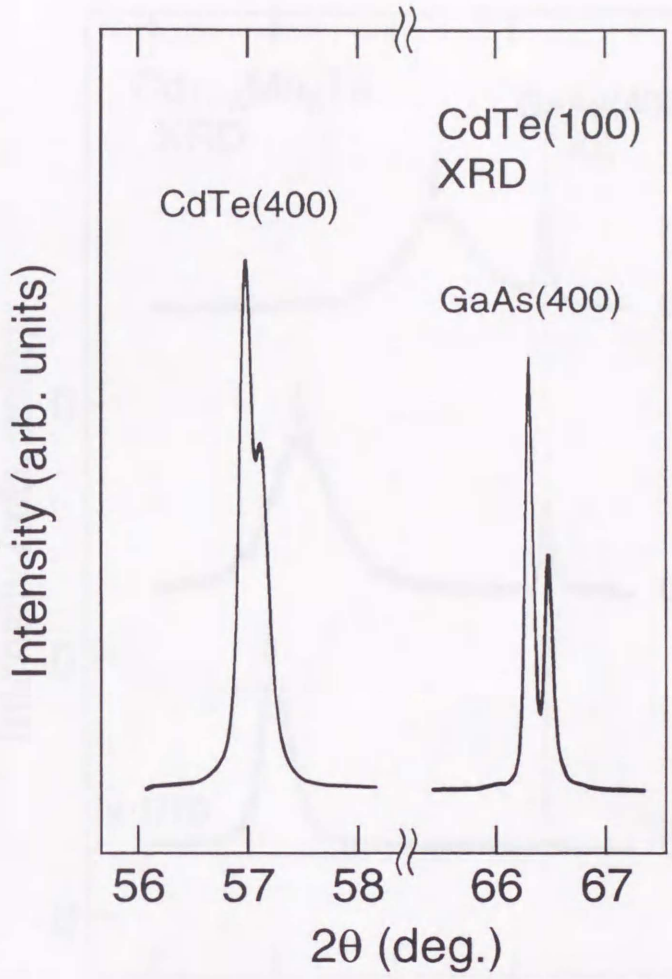

Fig. 4-8. CdTe(400) and GaAs(400) diffraction lines of a thick CdTe film grown epitaxially on GaAs(100) substrate.

Figure 4-10 shows the XPS spectra of the (a) Cd 3*d*, (b) Mn 2*p* and (c) Te 3*d* core levels of a $Cd_{0.3}Mn_{0.7}Te$ thin film used for the UPS and IPES measurements. After the subtraction of the secondary electrons background, integrated emission-intensities of each spectrum were evaluated for the shaded areas indicated in Fig. 4-10. The *x*-value was calculated by using the evaluated intensities corrected by each cross section. The *x*-values of the other $Cd_{1-x}Mn_xTe$ thin films used for the UPS and IPES measurements were also evaluated by the same procedure. The *x*-values evaluated from the XPS measurements for thin epitaxial films were in good agreement with those for thick films estimated from the XRD within $x = \pm 0.05$.

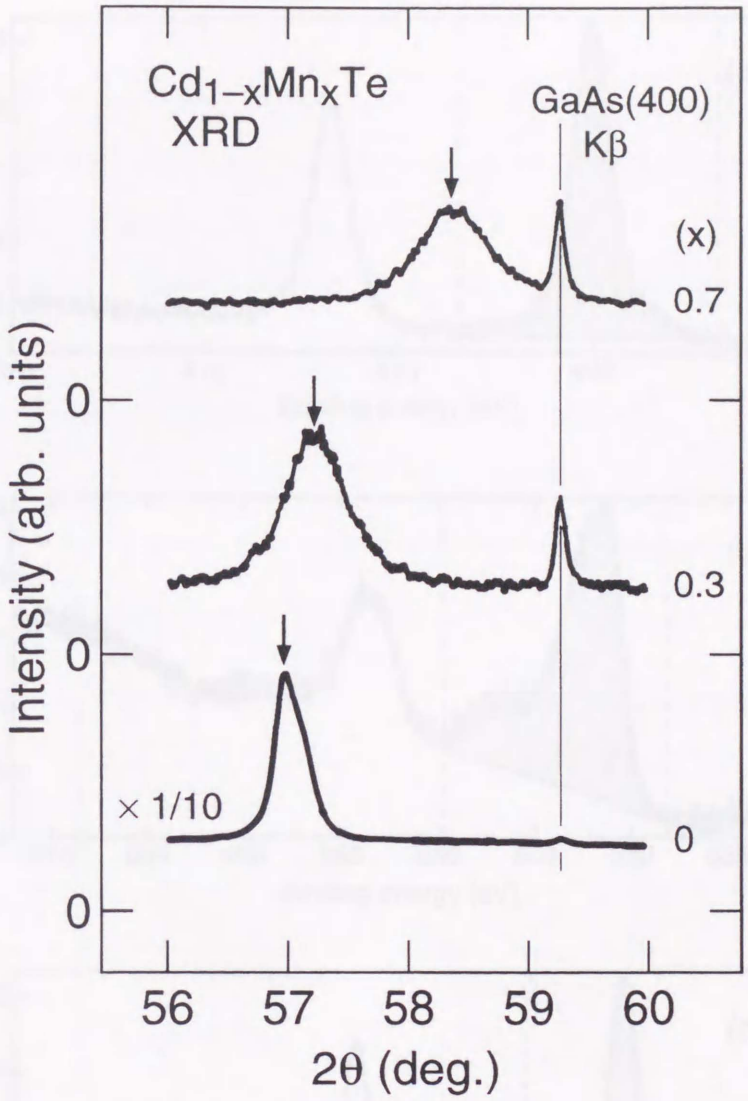

Fig. 4-9. A series of (400)-diffraction lines of thick $Cd_{1-x}Mn_xTe$ films grown eppitaxially on GaAs(100) substrates with $x = 0$, 0.3 and 0.7. Vertical arrows indicate the positions of (400)-diffraction lines.

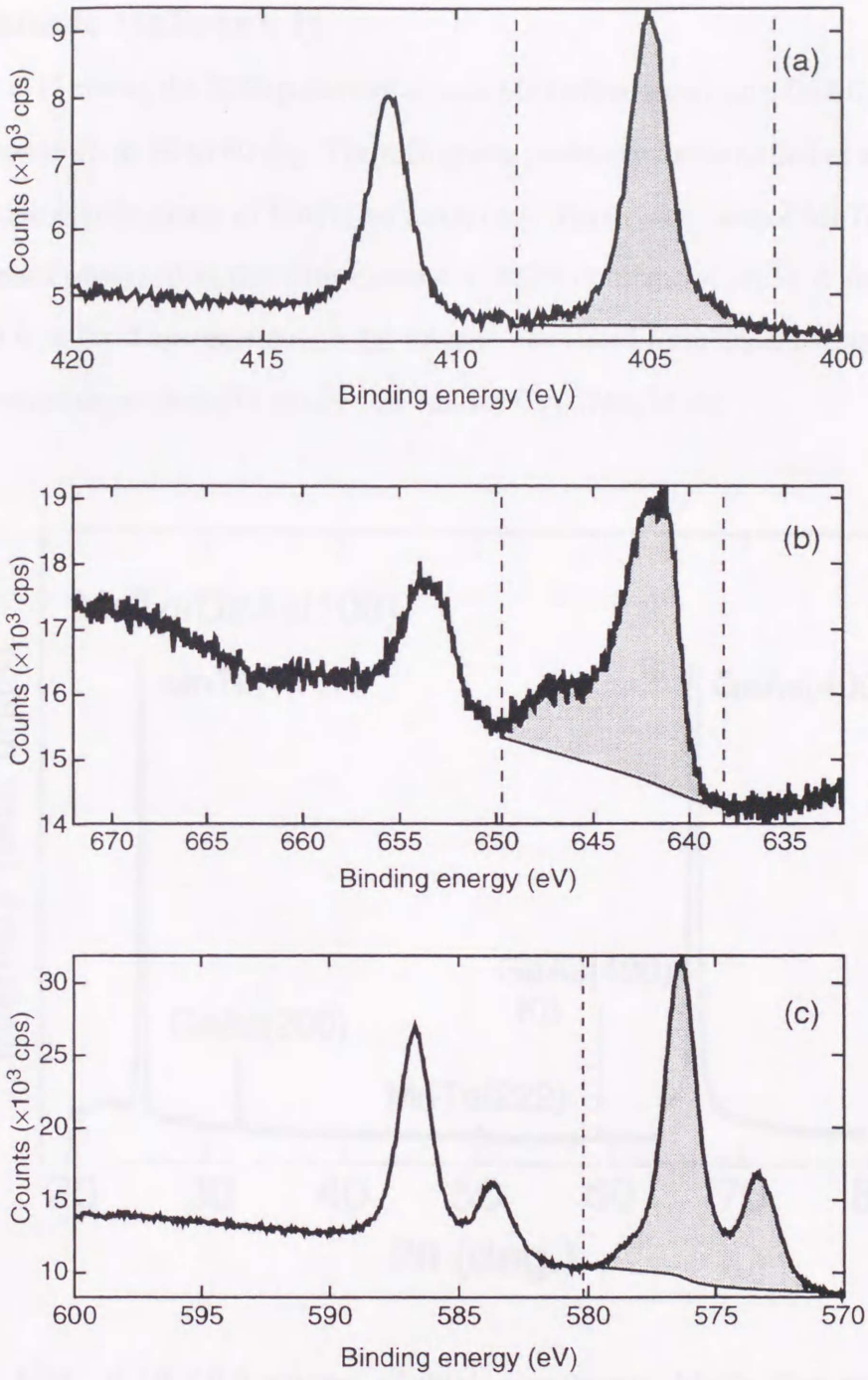

Fig. 4-10. XPS spectra of (a) Cd 3*d*, (b) Mn 2*p* and (c) Te 3*d* core levels of $Cd_{0.3}Mn_{0.7}Te$ thin film used for the UPS and IPES measurements. XPS measurements were performed again after the UPS and IPES measurements. These spectra were used for the evaluation of Mn concentration (x).

(2) zinc-blende MnTe ($x = 1$)

Figure 4-11 shows the XRD pattern of a thick MnTe film grown on a GaAs(100) substrate with the 2θ range from 20 to 80 deg. The diffraction peaks can be identified as corresponding only to the zinc-blende phase of MnTe; no hexagonal NiAs-type phase of MnTe is observed. The XRD peaks observed in this film indicate a lattice constant of ~6.34 Å for zinc-blende MnTe which is in good agreement with the value of calculated form linear extrapolation of the Mn concentration dependence of lattice constant for $Cd_{1-x}Mn_xTe$ [6].

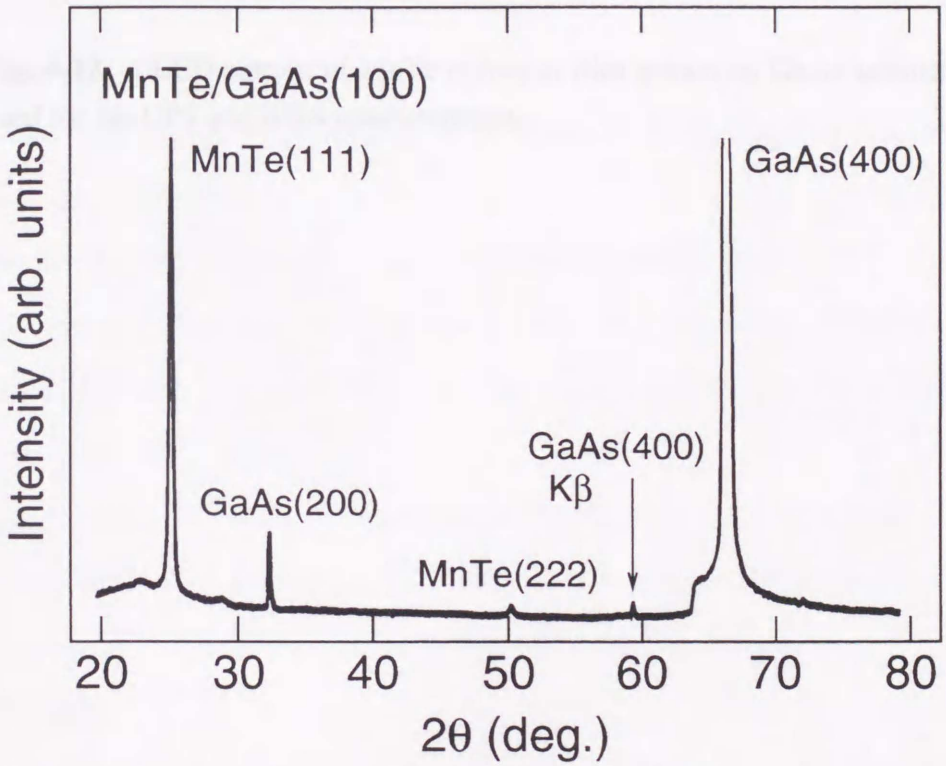

Fig. 4-11. θ-2θ XRD pattern of thick zinc-blende MnTe film grown epitaxially on GaAs(100) substrate.

Figure 4-12 shows a LEED pattern of a MnTe film used for the UPS and IPES measurements. One notices that a well-defined LEED pattern of an unconstructed zinc-blende MnTe(111) epitaxial film was successfully obtained.

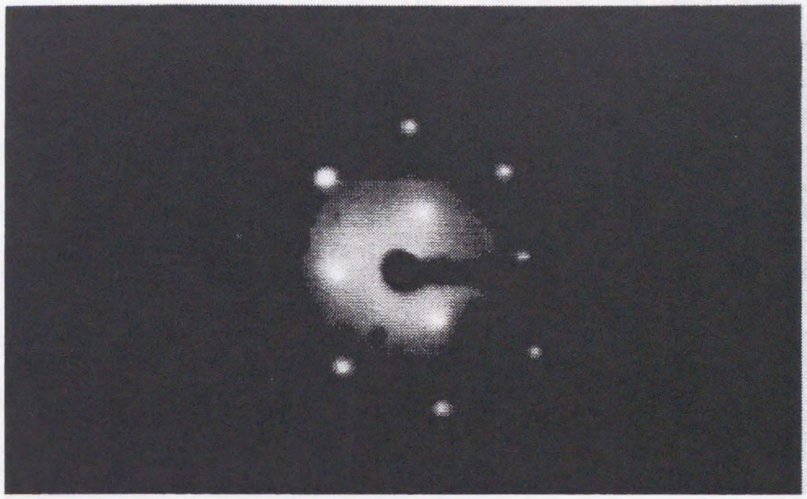

Fig. 4-12. LEED pattern of MnTe epitaxial film grown on GaAs substrate used for the UPS and IPES measurements.

References

[1] P.W. Erdman and E.C. Zipf, Rev. Sci. Instrum. **53** (1982) 225.

[2] The characteristics of the detector were evaluated with the aid of synchrotron radiation from SOR-RING (an electron storage ring operated at 0.38 GeV) at the Institute for Solid State Physics of The University of Tokyo.

[3] K. Yokoyama, K. Nishihara, K. Mimura, Y. Hari, M. Taniguchi and M. Fujisawa, Rev. Sci. Instrum. **64** (1993) 87.

[4] Y. Ueda, K. Nishihara, K. Mimura, Y. Hari, M. Taniguchi and M. Fujisawa, Nucl. Instrum. and Methods, A **330** (1993) 140.

[5] H. Sitter, K. Lischka, W. Faschinger, J. Wolfrum, H. Pascher and J.L. Pautrat, J. Cryst. Growth **86** (1988) 377.

[6] N. Bottka, J. Stankiewicz and W. Giriat, J. Appl. Phys. **52** (1981) 4189.

[7] K. Lischka, E.J. Fantner, T.W. Ryan and H. Sitter, Appl. Phys. Lett. **55** (1989) 1309.

[8] J.H. Lee, S.B. Kim, B.J. Koo, I.H. Chung, M. Jung, H.L. Park and T.W.Kim, Solid State Commun. **84**, 901 (1992).

[9] H. Tatsuoka, H. Kuwabara, Y. Nakanishi and H. Fujiyasu, J. Appl. Phys. **67** (1990) 6860.

[10] S.M. Durbin, J. Han, O. Sungki, M. Kobayashi, D.R. Menke, R.L. Gunshor, Q. Fu, N. Pelekanos, A.V. Nurmikko, D. Li, J. Gonsalves and N. Otsuka, Appl. Phys. Lett. **55** (1989) 2087.

[11] R.L. Gunshor, M. Kobayashi, L.A. Kolodziejski, N. Otsuka and A.V. Nurmikko, J. Cryst. Growth **99** (1990) 390.

[12] D.W. Niles, H. Höchst and M.A. Engelhardt, J. Electron Spectrosc. Related Phenom. **52** (1990) 139.

[13] P. Klosowski, T.M. Giebultowicz, J.J. Rhyna, N. Samarth, H. Luo and J.K. Furdyna, J. Appl. Phys. **70** (1991) 6221.

[14] H. Akinaga, K. Ando, T. Abe and S. Yoshida, J. Appl. Phys. **74** (1993) 746.

[15] H. Akinaga and K. Ando, Appl. Surf. Sci. **75** (1994) 292.

[16] P.R. Bressler and H.-E. Gumlich, J. Cryst. Growth **138**, 1028 (1994).

[17] H. Anno, T. Koyanagi and K. Matsubara, J. Cryst. Growth **117** (1992) 816.

[18] K. Ando, K. Takahashi and T. Okuda, J. Magn. Magn. Mater. **104-107** (1992) 993.

[19] A. Lopez-Otero, Thin Solid Films **49** (1978) 3.

Chapter 5.
Experimental details II: Resonant photoemission spectroscopy

5-1. Photoemission measurements at SOR-RING

Resonant photoemission (RPES) measurements in the Mn 3*p*-3*d* core excitation region were performed at BL-2 of Institute for Solid State Physics (ISSP-SOR) of The University of Tokyo [1]. Radiation from a 380 MeV electron storage ring (SOR-RING) was monochromized by a 2 m grating incidence monochromator of the modified Rowland mount type. A double-stage cylindrical mirror analyzer (DCMA) mounted on an analyzer chamber was used to the measurements of angle-integrated photoemission spectra. A preparation chamber is connected to the analyzer chamber separated by a gate valve. An airlock which accommodates a sample bank was attached to the preparation chamber. We could change the sample without breaking the vacuum of the analyzer chamber. All photoemission measurements were performed at room temperature with the energy resolution of ~0.3 eV without any electrostatic charging effect. Intensities of resonant photoemission spectra were normalized to the monochromator output using a photoelectron yield from a Au film, taking its quantum yield [2] into account. The base pressure of the analyzer and preparation chambers was 7×10^{-11} and 1×10^{-10} Torr, respectively.

5-2. Sample preparation

Bulk $Cd_{1-x}Mn_xTe$ samples used for the resonant photoemission measurements were grown by a Bridgeman furnace arranged in the Taniguchi laboratory. Suitable amounts of Cd (purity 99.999 %), Mn (purity 99.99 %), and Te (purity 99.9999 %) metals were enclosed in quartz ampoules under vacuum better than 1×10^{-5} Torr. Then this ampoule was set in the Bridgeman furnace. The temperature gradient in the furnace was about 1 °C/mm and the descent

speed of the ample was 3 mm/hr. The starting temperature at the bottom of ample was 1200 °C. The crystal structure for the obtained bulk samples was checked by X-ray diffraction (XRD) with the Cu $K\alpha_1$ line (1.540562 Å wave length). The x-values were evaluated by means of electron-probe micro-analysis (EPMA). Table 5-I shows x-values determined by EPMA in comparison with those in the starting point. The clean surface of samples for the measurements were prepared *in situ* by cleavage in the sample preparation chamber under the base pressure of 1×10^{-10} Torr. Details for the Bridgeman furnace and the growth of DMS's have been already described in Ref. 3.

Table 5-I. x-values of bulk $Cd_{1-x}Mn_xTe$ samples determined by EPMA

x-values in starting point	0.10	0.20	0.30	0.40	0.50	0.60	0.70
x-values	0.10	0.18	0.30	0.40	0.48	0.60	0.69

References

[1] H. Sugawara, K. Naito, T. Miyahara, A. Kakizaki, I. Nagakura and T. Ishii, J. Phys. Soc. Jpn. **53** (1984) 279.

[2] J.B. Pendry, J. Phys. C **14** (1980) 1381.

[3] N. Happo, Dr. thesis, Hiroshima University (1996).

Chapter 6.
Results and discussion

6-1. Photoemission and inverse-photoemission study of $Cd_{1-x}Mn_xTe$

6-1-1. Ultraviolet photoemission and inverse-photoemission spectra of $Cd_{1-x}Mn_xTe$

Figure 6-1 shows a series of valence-band UPS and conduction-band IPES spectra of $Cd_{1-x}Mn_xTe$ films grown epitaxially on conductive GaAs(100) substrates with $x = 0$, 0.2, 0.3, 0.5 and 0.7. Intensities of the UPS and IPES spectra are tentatively normalized at –1.5 and 12 eV, respectively. The energy scale is referred to the valence-band maximum (VBM). The UPS spectrum of pure CdTe has been previously reported by several authors and discussed in detail. We recall here that the features at –1.0, –1.5, –2.5 and –4.4 eV indicated by vertical bars reflect maxima in the DOS of valence bands mainly derived from flat regions around the L_3, X_5, W_2- Σ_1^{min} and L_1 symmetry points, respectively [1, 2]. The valence-band DOS is primarily composed of the Te 5*p* states. With increasing x from 0 to 0.3, we find no discernible change in the shape of the valence bands, except for a slight blurring of fine structures. For x above 0.5, however, new emission shows up clearly between the two prominent peaks at –1.5 and –4.4 eV. The shapes of the UPS spectra are consistent with those measured for $Cd_{1-x}Mn_xTe$ ($0 \le x \le 0.65$) at excitation-photon energy of 22 eV by means of photoemission using synchrotron radiation [3]. An increasing spectral density between –1.5 and –4.4 eV with x is predominantly due to the Mn 3*d* emission with a main peak at –3.4 eV [3, 4]. Although the positions of the Cd 4*d* core levels have been reported to be almost independent of x in the earlier experiment [3], energies of the $4d_{5/2}$ and $4d_{3/2}$ relative to the VBM are found to shift almost linearly from –10.10 and –10.75 eV ($x = 0$) to –10.30 and –10.95 eV ($x = 0.7$), respectively, in the present study. In addition, we have found that the energies of the Cd 4*d* core levels measured at ~50 eV

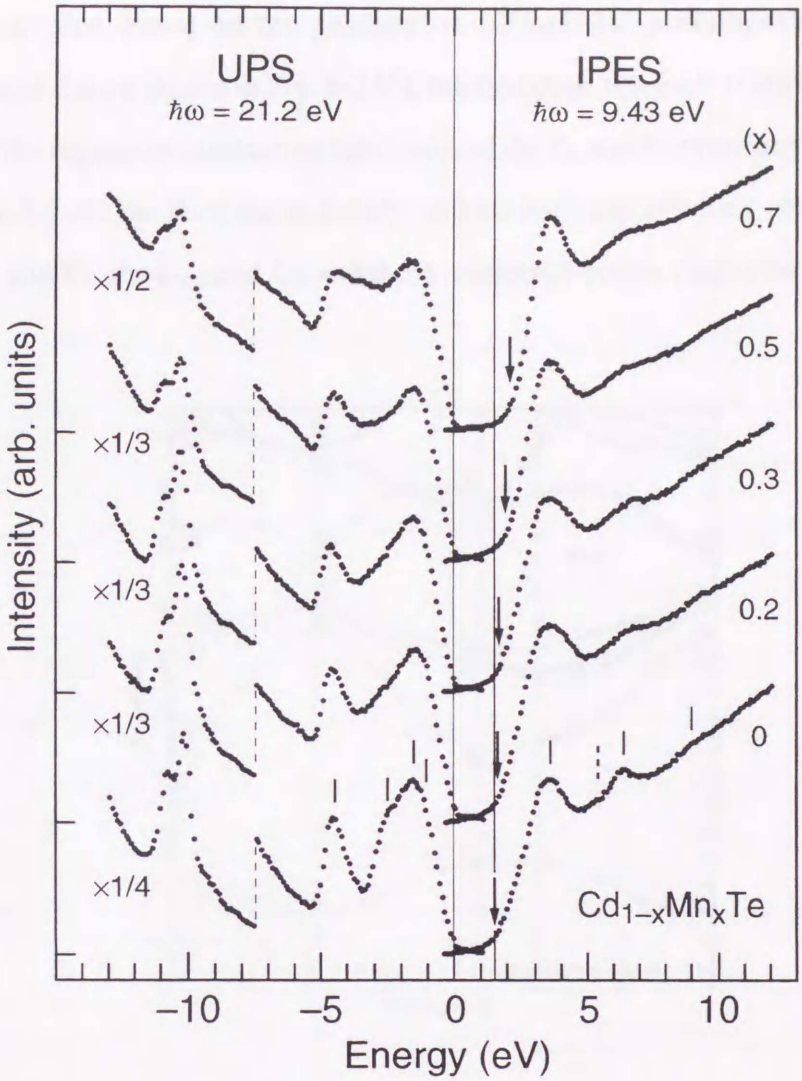

Fig. 6-1. A series of the valence-band UPS and conduction-band IPES spectra of $Cd_{1-x}Mn_xTe$ films grown epitaxially on GaAs(100) substrates with x of 0, 0.2, 0.3, 0.5 and 0.7. Intensities of the UPS and IPES spectra are tentatively normalized at –1.5 and 12 eV, respectively. Vertical bars indicate the position of structures and arrows indicate the thresholds of the IPES spectra. Energies are referred to the VBM.

in the bulk $Cd_{1-x}Mn_xTe$ alloys shift also almost linearly with x. The origin of these energy shifts is discussed below, in terms of the band-structure calculation [5].

On the other hand, The IPES spectrum of pure CdTe exhibits peak structures at 3.7, 5.4, 6.4 and 9.0 eV above the VBM (vertical bars). From a comparison with the results of band-

structure calculation based on the nonlocal semiempirical pseudopotential method by Chelikowsky and Cohen shown in Fig. 6-2 [6], the first peak at 3.7 eV is attributed to the DOS feature due to flat regions of conduction bands around the X_6 and X_7 symmetry points. The weak second peak at 5.4 eV, the third one at 6.4 eV, and the forth one at 9.0 eV are ascribed to those around the Γ_7 and Γ_8, the $L_{4,5}$ and L_6, and the Λ symmetry points, respectively.

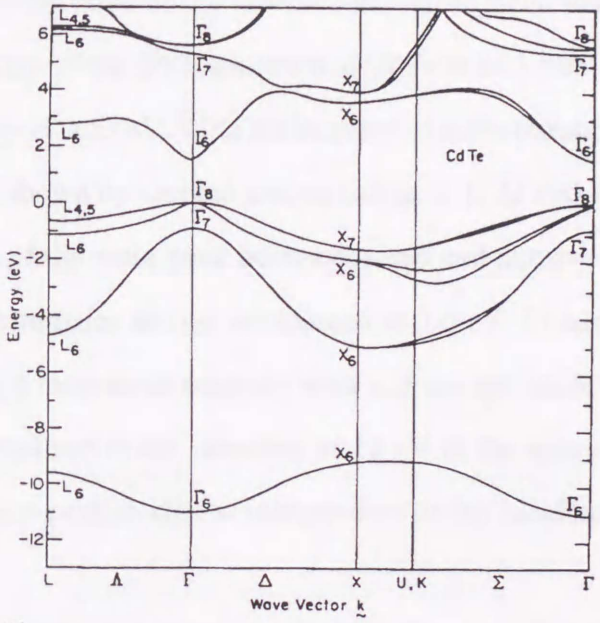

Fig. 6-2. Band structure for CdTe calculated by Cherikowsky and Cohen [6]. The VBM is taken as the zero of energy.

As regards the energy positions of structures, the spectrum is quantitatively consistent with the ultraviolet IPES spectrum for the CdTe(110) cleaved surface measured at normal incidence using tunable-photon anergy mode [7], except for the surface-resonance peak on CdTe(110) at 2.8 eV above the VBM. On the basis of the band-structure calculation by Chadi *et al.* [8], features observed at 3.7 and 6.4 eV above the VBM were attributed to the X_6 and Γ_8 symmetry points of the conduction bands, respectively [7]. The BIS spectrum at a photon energy of 1486.6 eV on CdTe(110) cleaved surface has been also reported, emphasizing structures at 4.1, 6.7, 9.6, 11.3, 12.5 and 15 eV above the VBM [9]. From a comparison with the results of nonlocal semiempirical-pseudopotential calculation [6], peaks at 4.1 and 6.7 eV were

ascribed to the DOS feature of conduction bands originating from states around the Δ and X symmetry points, and that derived from states in low symmetry directions of the Brillouin zone [9], respectively. We find that the peak structures at 4.1, 6.7 and 9.6 eV in the BIS spectrum correspond to those at 3.7, 6.4 and 9.0 eV in the present IPES spectrum, respectively, after the shift of the peaks in the BIS spectrum by 0.3–0.6 eV toward lower energy.

The energy position of the conduction-band minimum (CBM) can be roughly evaluated by extrapolating the leading edge of the lowest conduction-band peak to the baseline. One notices the threshold energy of the IPES spectrum of CdTe to be 1.5 eV in good agreement with the direct band-gap energy of 1.53 eV. With the increase of x, the threshold shifts almost linearly toward higher energy as shown by vertical arrows in Fig. 6-1. At x=0.7, the spectral rise at the threshold and the width of the main peak becomes steep and narrow, respectively, while the energy of the main peak remains almost unchanged at 3.6 eV. In addition, the main peak is assumed to exhibit a slight increase in intensity with x, if the spectra of $Cd_{1-x}Mn_xTe$ ($0.2 \leq x \leq 0.7$) are tentatively normalized to the intensity at 12 eV in the spectrum of pure CdTe. The energy of the narrow main-peak is almost independent of the incidence angle of the electron beam.

The higher-energy shift of the threshold with x is consistent with the variation of the fundamental band-gap energy determined by optical absorption [10] and ellipsometry measurements [11], and can be understood as a result of an increasing contribution of the higher lying Mn 4s level relative to the Cd 5s level [5, 10, 11]. The shift at $x = 0.7$ is, however, by about 0.2 eV smaller than that obtained from the experiments on interband transitions [10, 11]. These shifts are mainly due to the characteristics of the IPES spectrometer with an overall energy-resolution of 0.56 eV, therefore, spectral broadening due to such an instrumental resolution is significant for measurements of the intense and steep edge.

The narrowing, constant energy-position and a slight increase in intensity of the main peak with x suggest the Mn derived states with fairly localized character at 3.6 eV above the VBM. The energy position is in agreement with 3.3±0.5 eV predicted for the Mn 3$d\downarrow$ states from the analysis of the Te L_1 and L_3 XANES spectra [12]. A constant energy of the narrow

main-peak for the incidence angle of the electron beam is also consistent with the localized character.

While the Mn 3*d* features in the UPS spectra are clearly observed as an increase in intensity at –3.4 eV with *x*, those in the IPES spectra can be recognized only in the form of a narrowing of the main peak at constant energy of 3.6 eV, and as a slight increase in intensity of the main peak under the tentative normalization of the spectra. We assume that the main reasons why the Mn 3*d* features are less pronounced in the IPES spectra in comparison with those in the UPS spectra in Fig. 6-1 are that: (1) The photoabsorption cross-section of the Mn 3*d* states [13] at 9.43 eV (IPES) is smaller by a factor of about 3 than that at 21.2 eV (UPS). (2) The Mn 3*d* features in the IPES spectra show up at an energy just overlapping with the first peak in the spectrum of CdTe, whereas those in the UPS spectra appear at an energy between the two prominent DOS peaks.

6-1-2. Resonant photoemission spectra of $Cd_{1-x}Mn_xTe$

Figure 6-3 shows a series of valence-band photoemission spectra of $Cd_{0.31}Mn_{0.69}Te$ for photon energy ($\hbar\omega$) near the Mn 3*p*-3*d* core excitation region (~50 eV). Energy is referred to the VBM. In Fig. 6-3, we can compare the spectra not only with respect to their shape but also in terms of their relative intensities, because the spectral intensities are normalized to the monochromator output. One notices that the prominent peak at –3.4 eV is remarkably enhanced. With increasing $\hbar\omega$ from 43 to 60 eV, the intensity of this peak decreases gradually until its minimum at $\hbar\omega = 47.4$ eV and reaches to the maximum at $\hbar\omega = 49.9$ eV. The other states in the valence bands except for the peak at –3.4 eV are also enhanced, and, in particular, states between –6 and –9 eV appears near the resonance.

In order to investigate the resonant profile in detail, we measured constant-initial state (CIS) spectra which trace the photoemission cross sections of selected valence-band features as a function of $\hbar\omega$. Figure 6-4 shows the CIS spectra of $Cd_{0.31}Mn_{0.69}Te$ at the initial energy (E_i) with respect to the VBM. One can see that the spectrum for $E_i = -3.4$ eV shows a prominent

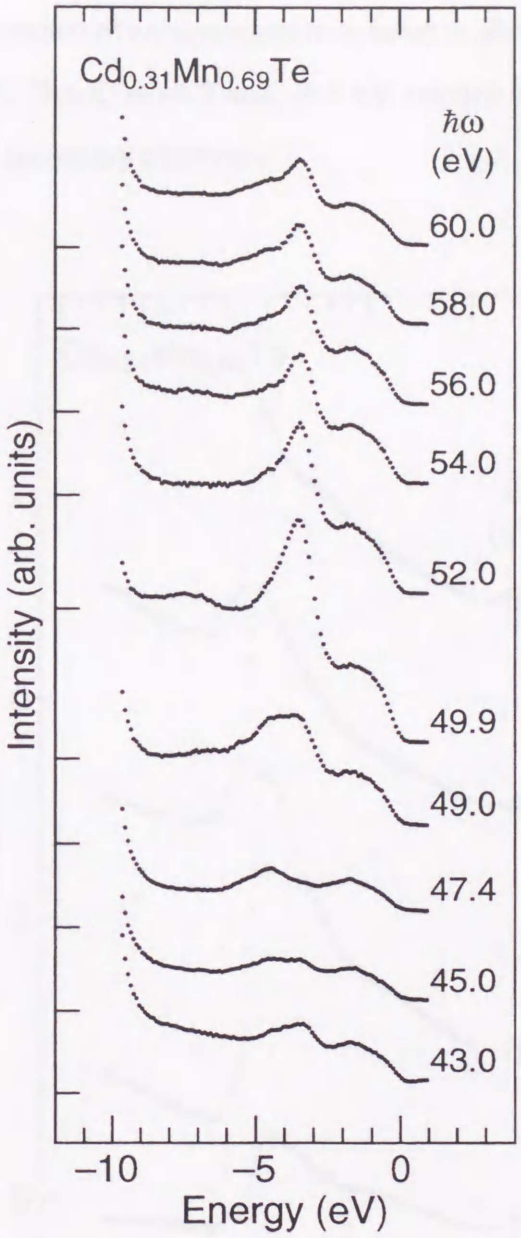

Fig. 6-3. A series of valence-band spectra of $Cd_{0.31}Mn_{0.69}Te$ for $\hbar\omega$ near the Mn $3p$-$3d$ core excitation. The peak at –3.4 eV indicates a prominent resonance.

Fano-type resonance. With increasing $\hbar\omega$, the intensity of this structure first decreases gradually to a minimum at 47.4 eV, and then increases sharply to reach a maximum at 49.9 eV, reflecting the same a tendency seen in Fig. 6-3. The spectra for E_i = –0.8 and –1.8 eV also exhibit a

remarkable resonance. The amount of enhancement is as much as about one-third of that for the spectrum for E_i = –3.4 eV. The E_i = –4.3 and –6.8 eV spectra have contributions in the background due to inelastic secondary electrons.

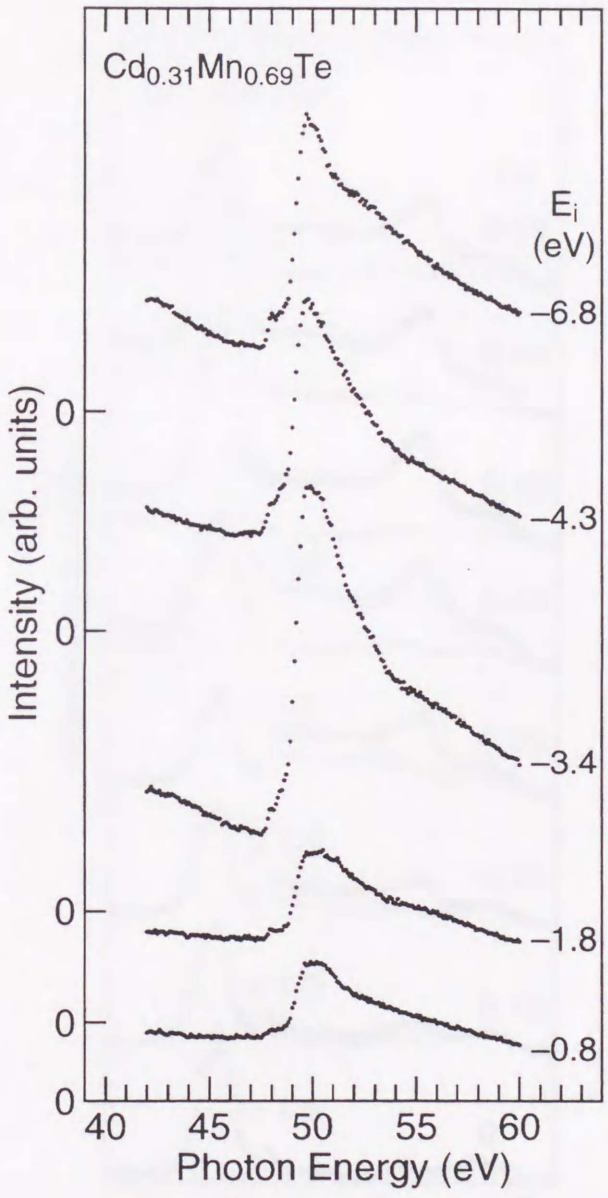

Fig. 6-4. CIS spectra of $Cd_{0.31}Mn_{0.69}Te$ for selected valence-band regions that are identified by binding energy E_i.

Figure 6-5 shows the valence-band photoemission spectra of $Cd_{1-x}Mn_xTe$ with x = 0, 0.10, 0.18, 0.30, 0.40, 0.48, 0.60 and 0.69. In this figure, upper curves and lower curves indicate the spectra measured just on resonance ($\hbar\omega$ = 49.9 and 49.5 eV) and at antiresonance ($\hbar\omega$ = 47.4

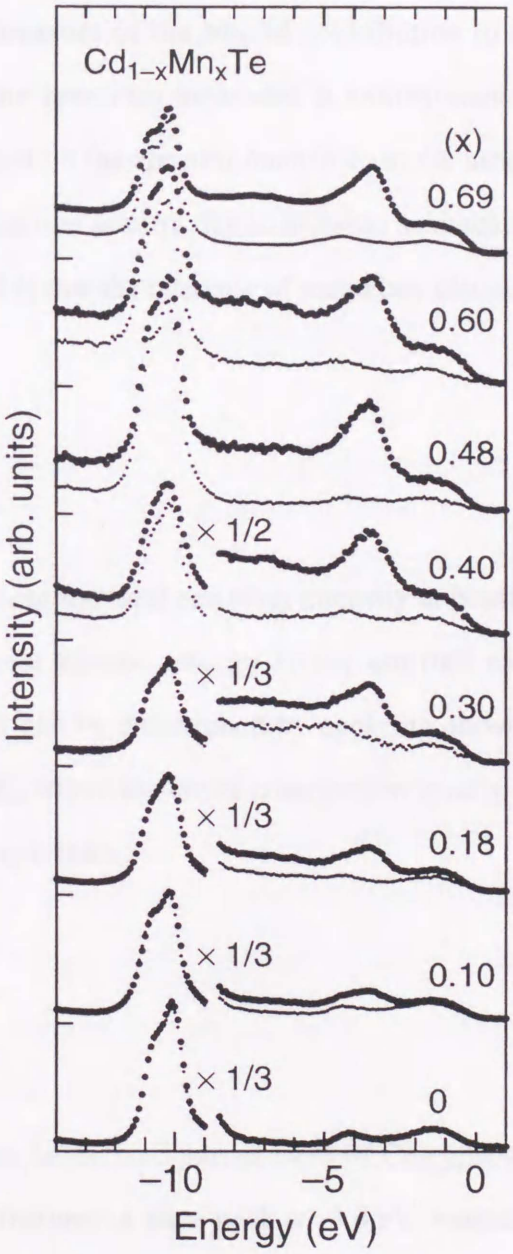

Fig. 6-5. Valence-band photoemission spectra of $Cd_{1-x}Mn_xTe$ alloys with x = 0, 0.10, 0.18, 0.30, 0.40, 0.48, 0.60 and 0.69. For each Mn concentrations, upper and lower curves indicate the spectra measured just on resonance and at antiresonance, respectively.

and 47.0 eV), respectively. For $Cd_{0.31}Mn_{0.69}Te$ only, the energy positions of the resonance and antiresonance shift by 0.4 eV toward the higher $\hbar\omega$ values due to the influence of the adjustments of the monochromator with the difference of the measurement time. We can recognize that all spectra recorded just on resonance, except for that of $x = 0$, are remarkably enhanced. Intense peaks at about 10 eV originate from the Cd 3*d* core emission.

In order to deduce a measure of the Mn 3*d* contribution to the valence-band DOS in $Cd_{1-x}Mn_xTe$, we subtract the spectrum measured at antiresonance from that taken just on resonance, after the normalization the spectral intensities to the monochromator output. Here, the backgrounds in the subtraction spectra due to inelastic secondary electrons were removed from the spectra, assuming [14] that the intensity of secondary electrons $I_s(E)$ at binding energy E is given by

$$I_s(E) = k\int_{E_0}^{E} I(E')dE', \tag{6. 1}$$

where $I(E')$, E_0, and k represent the total emission intensity at binding E', the binding energy corresponding to the highest kinetic energy fo the emitted electrons, and a constant, respectively. The constant k can be determined by applying above formula to the emission intensity at binding energy E_a where the entire contribution is only from secondary electrons. Then, k satisfies the following relation:

$$k = \frac{I_s(E_a)}{\int_{E_0}^{E_a} I(E')dE'}. \tag{6. 2}$$

Figure 6-6 shows a Mn 3*d*-derived partial DOS of $Cd_{0.31}Mn_{0.69}Te$. The Mn 3*d* partial DOS exhibits characteristic features: a main peak at –3.4 eV, valence bands from 0 to –2.5 eV and a broad satellite structure around –7 eV. These three fundamental features are observed for spectra corresponding to all Mn concentrations ($0.10 \leq x \leq 0.69$).

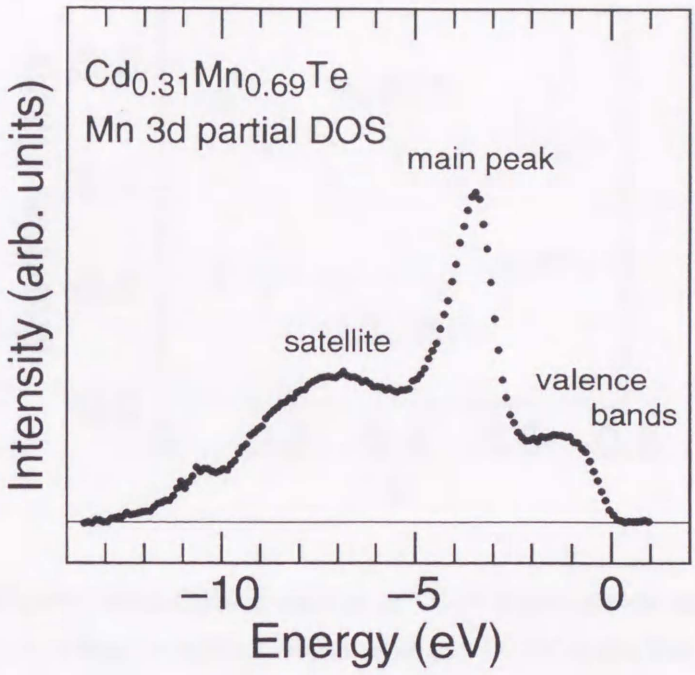

Fig. 6-6. Mn 3*d* partial DOS of $Cd_{0.31}Mn_{0.69}Te$ evaluated from resonant photoemission experiments. The Mn 3*d* partial DOS of $Cd_{1-x}Mn_xTe$ consists of three structures; a main peak of –3.4 eV, valence bands between 0 and –2.5 eV, and a broad satellite between –5 and –9 eV.

Figure 6-7 shows intensities of the satellite at –7 eV indicated by open circles and valence band at –1.2 eV by closed circles relative to that of the main peak at –3.4 eV in the Mn 3*d* partial DOS's for $Cd_{1-x}Mn_xTe$ alloys as a function of x ($0.10 \leq x \leq 0.69$). One notices that the satellite and valence-band intensities are almost independent of x. These intensities are almost unchanged within the range of 0.48 ± 0.03 and 0.23 ± 0.03, respectively, for $x = 0.10$–0.69. This independence of the relative intensity with respect to x is discussed bellow, using the configuration interaction theory.

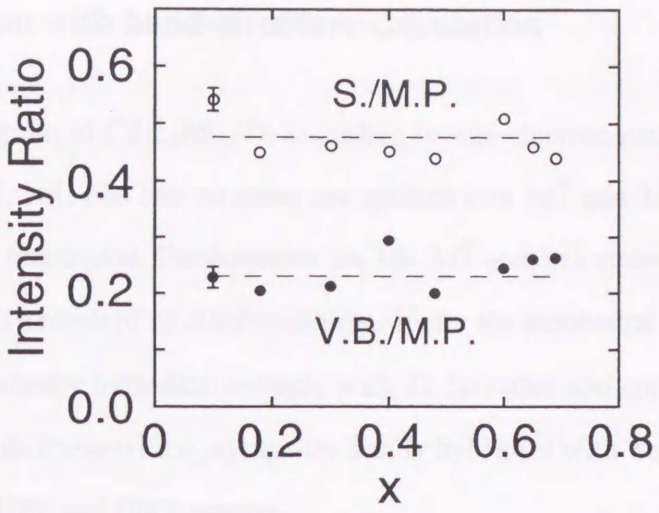

Fig. 6-7. Relative intensities of satellite at –7 eV (open circles) and valence band at –1.2 eV (closed circles) to main peak at –3.4 eV in the Mn 3*d* partial DOS of $Cd_{1-x}Mn_xTe$, as a function of x.

6-1-3. Comparison with band-structure calculation

The energy diagram of $Cd_{1-x}Mn_xTe$ according to one-electron picture is schematically shown in Fig. 6-8 [15, 16]. The Mn 3*d* states are splitted into $3d\uparrow$ and $3d\downarrow$ states by an intra-atomic spin exchange interaction. Furthermore, the Mn $3d\uparrow$ and $3d\downarrow$ states split into states with t_{2g} and e_g symmetry as a result of *sp-d* hybridization. Under the tetrahedral environment, the Mn 3*d* states with t_{2g} symmetry hybridize strongly with Te 5*p* states and spread into valence and conduction bands, while those with e_g symmetry hardly hybridize with Te 5*p* states and remain as sharp peaks in the UPS and IPES spectra.

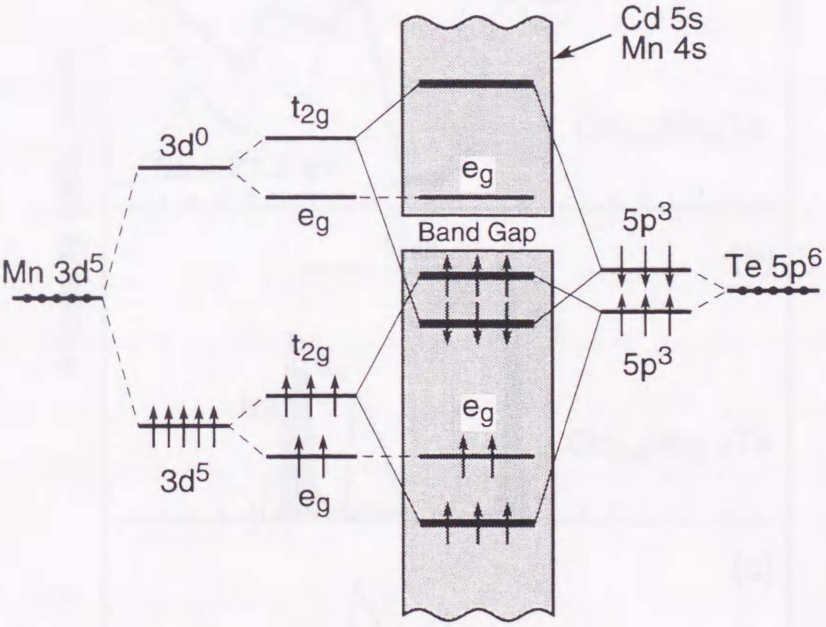

Fig. 6-8. Schematic energy diagram of $Cd_{1-x}Mn_xTe$ according to one-electron picture [15, 16].

Figure 6-9-(a) shows the valence-band UPS and conduction-band IPES spectra of $Cd_{0.3}Mn_{0.7}Te$ and CdTe films. The valence-band photoemission spectrum of $Cd_{0.31}Mn_{0.69}Te$ measured at a photon-energy of 49.9 eV (on resonance) is also shown to demonstrate the Mn 3*d* emission. One notices again a main peak at 3.6 eV and a broad and weak structure around 6.5 eV

in the IPES spectrum, and valence-band structure between 0 and –2.5 eV, a main peak at –3.4 eV in the UPS spectrum, and also a broad satellite between –5 and –9 eV in the spectrum measured at 49.9 eV, respectively.

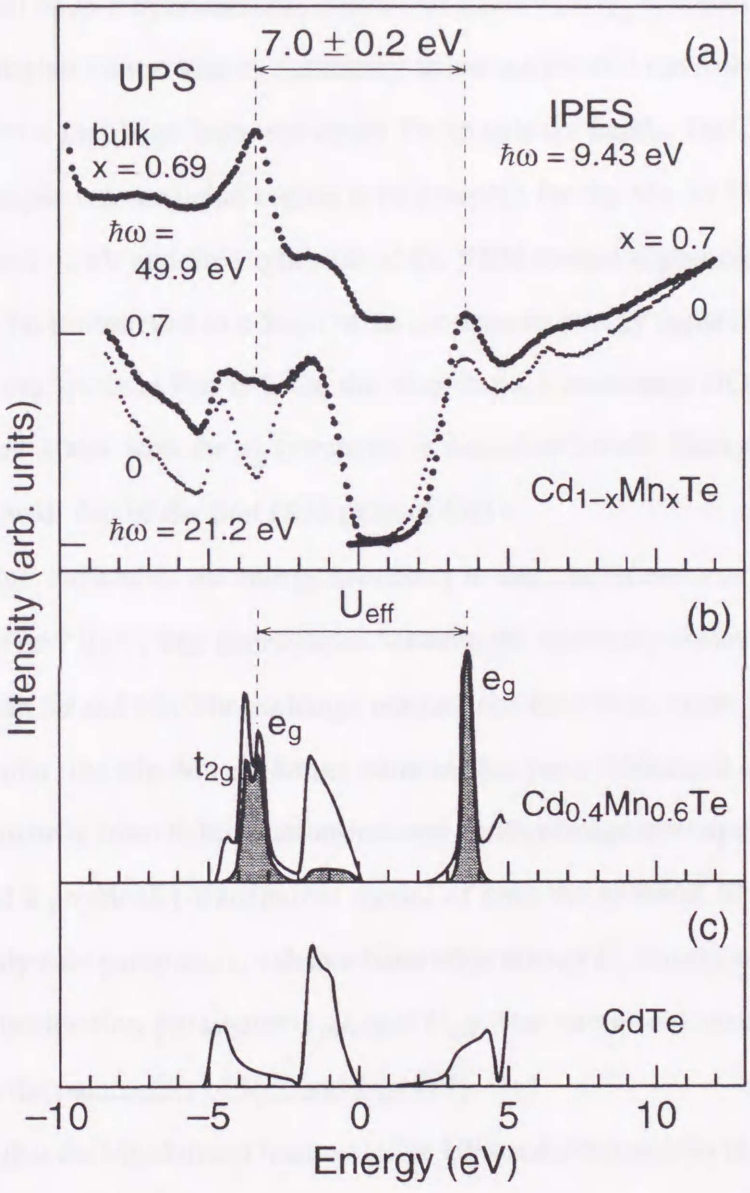

Fig. 6-9. (a) Valence-band UPS and conduction-band IPES spectra of $Cd_{0.3}Mn_{0.7}Te$ and CdTe films. To demonstrate the Mn 3*d* emission, the valence-band spectrum of $Cd_{0.31}Mn_{0.69}Te$ measured at 49.9 eV (on resonance) is also shown. (b) Total and Mn 3*d* partial (shaded area) DOS's of $Cd_{0.4}Mn_{0.6}Te$ and (c) total DOS of CdTe based on the tight binding calculations [5].

First, we compare Fig. 6-9-(a) with the theoretical total and Mn 3*d* partial DOS's of $Cd_{0.4}Mn_{0.6}Te$ calculated by Ehrenreich *et al.* [5] in Fig. 6-9-(b). The total DOS of CdTe is also shown in Fig. 6-9-(c) for the convenience of discussion. The zero of energy in the theoretical DOS's is referred to the VBM of CdTe. In Fig. 6-9-(b), the occupied Mn $3d\uparrow$ states split into two peaks as a result of *sp-d* hybridization. The lower states with t_{2g} symmetry hybridize more strongly than the higher states with e_g symmetry in the tetrahedral environment and shift to lower energy due to a repulsion from the upper Te 5*p* valence bands. The corresponding 3*d* admixture in the upper valence-band region is responsible for the Mn 3*d* DOS in the energy region between 0 and –2 eV and the slight shift of the VBM toward higher energy. Such a shift of the VBM is, in fact, observed in a form of an increase in energy separations between the VBM and Cd 4*d* core levels in Fig. 6-1. On the other hand, a prominent DOS peak due to the unoccupied Mn $3d\downarrow$ states with the e_g symmetry is placed at 3.6 eV. Energy position of this peak is coincident with that of the first DOS peak of CdTe.

The U_{eff}-value, *defined as the energy necessary to add one* 3*d electron to a* Mn^{2+} *ion* [5, 17–19], is taken to be 7.0 eV. The connections between the electronic structure in Fig. 6-9-(b) and the *sp*-band–Mn 3*d* and Mn-Mn exchange interactions have been extensively investigated [17, 18]. In particular, the Mn-Mn exchange constant has been calculated quantitatively and shown to result primarily from hybridization-induced antiferromagnetic super exchange. Then, authors developed a physically transparent model of both the *sp*-band–Mn 3*d* and Mn-Mn exchange using only four parameters; valence-band-edge energy E_v, energy of occupied Mn 3*d* states E_d, *p-d* hybridization parameter V_{pd}, and U_{eff}. For numerical results, the principal uncertainty lies in the parameters of V_{pd}, and U_{eff} [17].

One notices that the Mn-derived features in the UPS and IPES spectra in Fig. 6-9-(a) are in good agreement with those in the calculated DOS curves. Taking into account the experimental features observed for the narrow main-peak at 3.6 eV in the IPES spectrum as well as the comparison between experiment and theory in Fig. 6-9, we assign the peak at 3.6 eV to the Mn $3d\downarrow$ states, and evaluate the U_{eff}-value to be 7.0±0.2 eV from Fig. 6-9-(a). The new splitting-energy of 7.0±0.2 eV is in quantitative agreement with the predicted U_{eff}-value and supports the electronic structure model for the estimation of the nearest neighbor Mn-Mn exchange constant

(J^{dd}) of $Cd_{1-x}Mn_xTe$, using input parameters such as E_v–E_d = 3.4 eV taken from photoemission experiments [3, 4], U_{eff} = 7.0 eV, V_{pd} = 0.219 eV estimated from experimental *sp-d* exchange constant [20] and the Mn–Te bond length of 2.759 Å determined by extended X-ray absorption fine-structure (EXAFS) experiments [21]. Authors calculated further a chemical trend of J^{dd} in $Cd_{1-x}Mn_xY$ (Y = Te, Se, S). The predicted increase in J^{dd} from the telluride to the selenide is in reasonable agreement with the increase observed experimentally. The larger predicted increase in J^{dd} from selenide to sulfide overestimates the experimental trend, which may be corrected when more accurate input parameters become available.

Recent first principle calculations for $Cd_{1-x}Mn_xTe$ by Wei and Zunger predicted the U_{eff} of 4.9 eV [15, 16]. Calculations for paramagnetic zinc-blende MnTe by Masek *et al.* provided a value of 5.5 eV [22] and those for antiferromagnetic zinc-blende MnTe by Podgórny suggested a value of about 4 eV for the splitting energy [23]. All calculated values are substantially smaller than our experimental value of 7.0±0.2 eV. On the other hand, the earlier experimental value determined from the BIS measurements is 8.3±0.4 eV [24] and substantially larger than the present value. For this discrepancy, it should be noted that the photoemission and BIS measurements were made for different cleaved surfaces of $Cd_{0.8}Mn_{0.2}Te$ alloy [24], though the position of the Fermi level in the band-gap depends significantly on the cleaved faces of crystals. *In situ* measurements of the UPS and IPES spectra in the present study rule out such irreversible shift of the Fermi level.

With respect to the Mn derived feature at 4.6 eV in the reflectivity [25] and ellipsometry [11] measurements of $Cd_{1-x}Mn_xTe$, Kendelewicz interpreted tentatively the structure as coming from interband transitions from the *sp*-valence band to the unoccupied Mn 3*d* states [25]. The initial states were related to the maximum in the valence-band DOS at 1.8 eV below the VBM; the states around the X_5 symmetry point. This places the unoccupied Mn 3*d* states at 2.8 eV above the VBM. On the other hand, Franciosi *et al.* attributed the structure to optical transitions from the top of the *sp*-valence band states to the unoccupied Mn 3*d* states at 4.8±0.3 eV above the VBM on the basis of their experimental result [24]. Both values of 2.8 and 4.8 eV are rather in poor agreement with the present result of 3.6 eV.

The location of the unoccupied Mn 3*d* states at 3.6 eV above the VBM in the present study

provides a plausible interpretation. We remember that the valence-band spectrum of pure CdTe exhibits the DOS structure at –1.0 eV, which is primarily derived from the flat region of valence bands around the L_3 symmetry point. In addition, the shape of the *sp* part of the valence-band spectrum would not change appreciably when Mn is added [3]. The location of the unoccupied Mn 3*d* states at 3.6 eV above the VBM in the present study, thus, suggests that the optical transition at 4.6 eV is most probably due to transitions from the states around the L_3 symmetry point at –1.0 eV to the unoccupied Mn 3*d* states, in agreement with the assignment by Larson *et al.* [17].

6-1-4. Comparison with configuration-interaction calculation

In spite of the good correspondence between the experiment and energy-band theory, the theory cannot interpret the multielectron satellite in the energy region between –5 and –9 eV. Nor can it explain the intra-atomic d-d^* optical absorption observed at about 2.2 eV for $Cd_{1-x}Mn_xTe$ with $x \geq 0.4$ [26]. Gunnarsson *et al.* have presented the results of *ab initio* calculations for the parameters in the Anderson model, such as the energy-dependent *p-d* hybridization parameters and the Mn 3*d* Coulomb correlation energy of 7.3 eV [27]. Without any empirical parameters, the Mn 3*d* photoemission spectrum was fairly well reproduced including the multielectron satellites.

Very recently, the CI calculation using a $Mn^{2+}(Te^{2-})_4$ model cluster reported by Mizokawa and Fujimori has been extended to interpret not only the Mn 3*d* photoemission spectrum, but also the Mn 3*d* IPES spectrum and the d-d^* optical absorption spectra, using the same set of parameters [28]. Figure 6-10 exhibits (a) the valence-band photoemission spectrum of $Cd_{0.31}Mn_{0.69}Te$ measured at 49.9 eV (on resonance), a measure of the Mn 3*d* partial DOS evaluated from resonant photoemission experiments in the Mn 3*p*-3*d* core excitation region (dotted curves) and the conduction-band IPES spectrum of $Cd_{0.3}Mn_{0.7}Te$ film, and (b) the calculated spectra (solid curves) [28]. In the calculation, d^5, $d^6\underline{L}$, $d^7\underline{L}^2$ and d^4, $d^5\underline{L}$, $d^6\underline{L}^2$ configurations are taken into account for the initial and final states, respectively, where $\underline{L}$

represents a ligand hole. The line spectra are calculated using parameters of $U = 4.0$ eV, $\Delta = 2.0$ eV and $(pd\sigma) = -1.1$ eV. Here, U is the Coulomb correlation energy of the Mn $3d$ electrons and Δ is the ligand-to-metal charge-transfer energy. In addition, $(pd\sigma)$ represents the p-d transfer integral and $(pd\sigma)/(pd\pi)$ is fixed at -2.16 [29]. The solid curves are constructed by a convolution of the line spectra with Gaussian and Lorentzian functions for the sake of

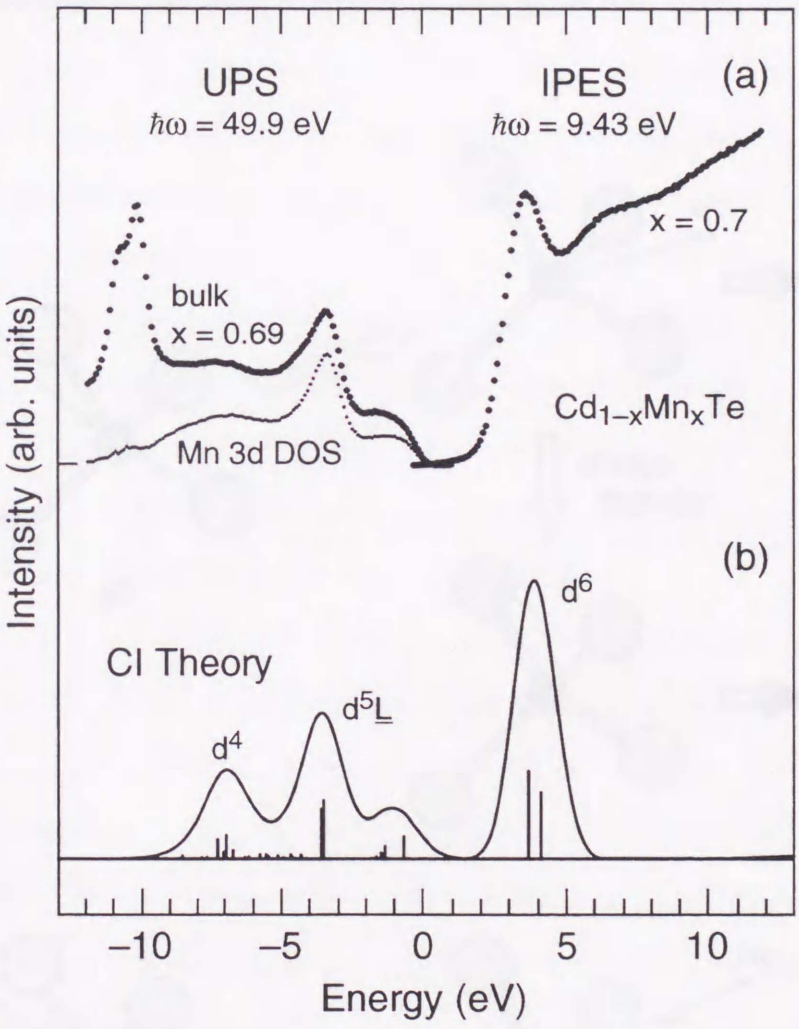

Fig. 6-10. (a) Conduction-band IPES spectrum of $Cd_{0.3}Mn_{0.7}Te$ film, valence-band photoemission spectrum of $Cd_{0.31}Mn_{0.69}Te$ measured at 49.9 eV (on resonance) and a measure of the Mn $3d$ partial DOS evaluated from resonant photoemission experiment in the Mn $3p$-$3d$ core excitation region (dotted curves). (b) Mn $3d$-derived photoemission and inverse-photoemission spectra of $Cd_{1-x}Mn_xTe$ calculated on the basis of the configuration interaction theory [28].

comparison. The CI analysis revealed that the feature between 0 and –5 eV with a main peak at –3.4 eV is predominantly due to transitions into the $d^5\underline{L}$ final states, whereas the satellite between –5 and –9 eV is ascribed to transitions into the d^4 final states. The $d^5\underline{L}$ denotes the states screened by charge transfer from the Te-derived valence-band states and the d^4 represents the final states produced by emission of a 3*d* electron from the d^5 ground state, as shown in Fig. 6-11-(a). On the same line of argument, the main peak at 3.6 eV in the Mn 3*d* inverse-photoemission spectrum is attributed to transitions into the d^6 final states. The d^6 denotes the

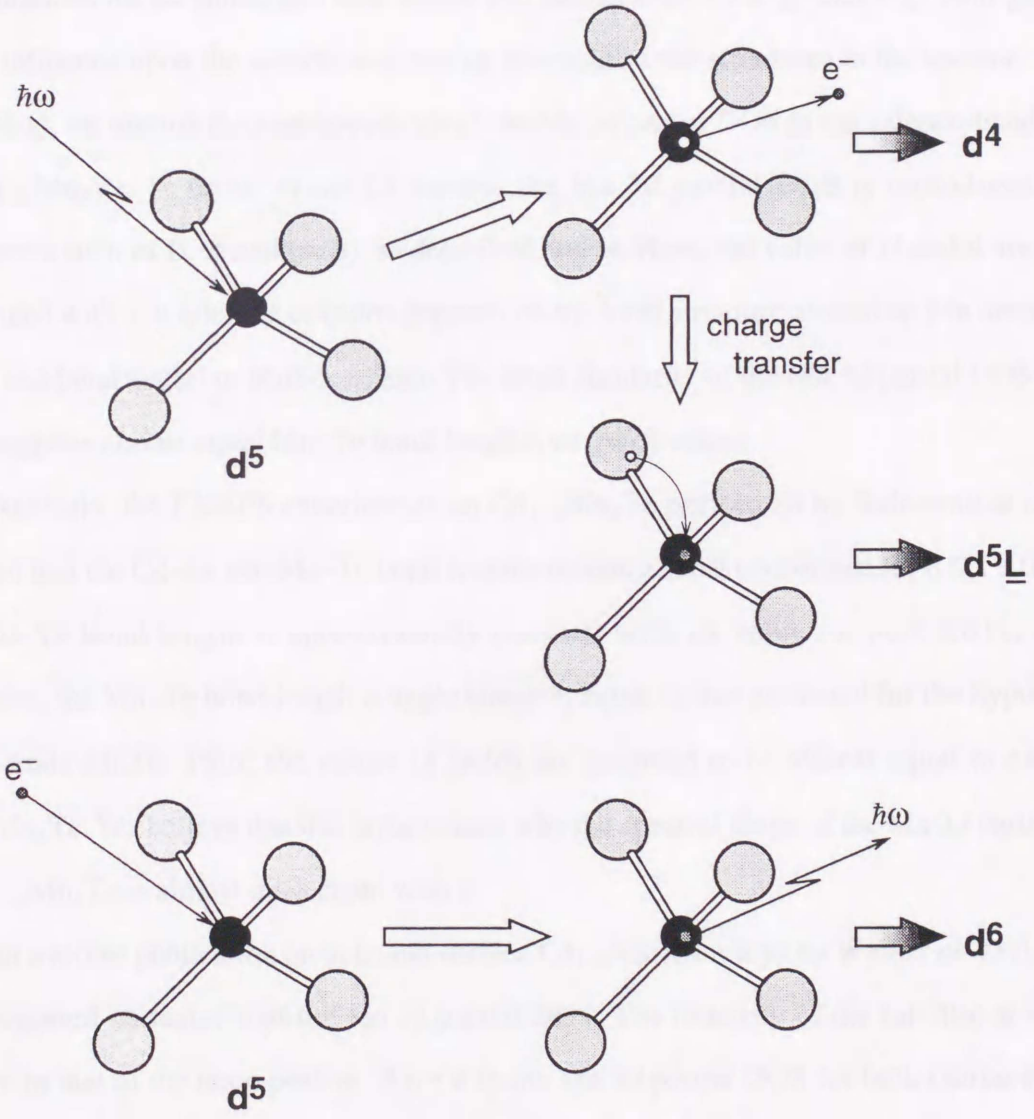

Fig. 6-11. The $MnTe_4$ cluster model of *d*-electron excitation process indicated by d^4, $d^5\underline{L}$ and d^6 final states in $Cd_{1-x}Mn_xTe$.

states added one $3d$ electron to the d^5 ground state, as shown in Fig. 6-11-(b).

Previous analysis for the Mn $3d$ partial DOS of $Cd_{1-x}Mn_xTe$ provided a Mn $3d$ Coulomb correlation energy of 7.5 eV [4, 30] [$U \equiv E(3d^4)+E(3d^6)-2E(3d^5)$, *where* $E(3d^n)$ *is the center-of-gravity of the* $3d^n$ *multiplet*], different from the value of 4.0 eV from Ref. 28. The discrepancy in U originates mainly from the fact that the relevant optical and magnetic properties and impurity states have been interpreted consistently using the same set of parameters. Besides, the previous analysis was performed using only the d^5, $d^6\underline{L}$ and d^4, $d^5\underline{L}$ configurations as initial and final states, respectively, while the recent analysis takes further account of the $d^7\underline{L}^2$ and $d^6\underline{L}^2$ configurations for the initial and final states. The inclusion of the $d^7\underline{L}^2$ and $d^6\underline{L}^2$ configurations has an influence upon the number and energy positions of the structures in the spectra.

Next, we discuss the x-independence of the Mn $3d$ partial DOS in the valence-band region of $Cd_{1-x}Mn_xTe$. In terms of the CI theory, the Mn $3d$ partial DOS is reproduced using parameters such as U, Δ and $(pd\sigma)$, as described above. Here, the value of U and Δ are almost unchanged with x, while that of $(pd\sigma)$ depends on the local structure around an Mn atom (bond length and bond angle) of $MnTe_4$ culster. The close similarity of the Mn $3d$ partial DOS with x, thus, suggests almost equal Mn–Te bond lengths, or $(pd\sigma)$ values.

Recently, the EXAFS experiments on $Cd_{1-x}Mn_xTe$ performed by Balzarotti *et al.* have revealed that the Cd–Te and Mn–Te bond lengths remain almost unchanged for $0 \le x \le 0.4$ [21]. The Cd–Te bond length is approximately constant with its value for pure CdTe, and, in particular, the Mn–Te bond length is approximately equal to that predicted for the hypothetical zinc-blende MnTe. Thus, the values of $(pd\sigma)$ are assumed to be almost equal to each x of $Cd_{1-x}Mn_xTe$. We believe that this is the reason why the spectral shape of the Mn $3d$ partial DOS of $Cd_{1-x}Mn_xTe$ is almost unchanged with x.

In a recent publication on bulk and surface $Cd_{1-x}Mn_xTe$ alloys by Wall *et al.* [31], results were reported on features of the Mn $3d$ partial DOS. The intensity of the satellite at –8.0 eV relative to that of the main peak at –3.6 eV in the Mn $3d$ partial DOS for bulk (surface) alloys increases remarkably from 0.19 to 0.37 (form 0.15 to 0.47) with the increase of x from 0.20 to 0.60 (from 0.29 to 0.94), whereas the relative intensity of the valence bands at –1.5 eV remains almost unchanged around 0.3 for the bulk and surface alloys, as shown in Fig. 6-12. All

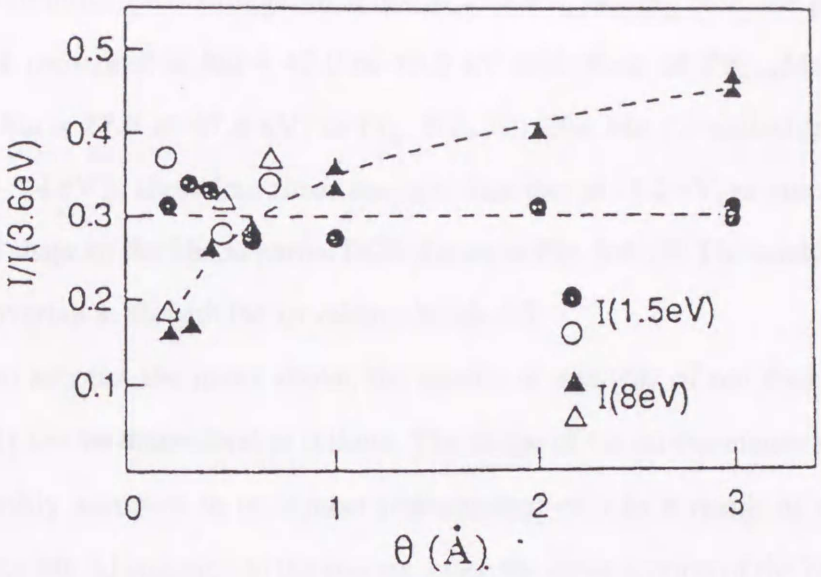

Fig. 6-12. Relative intensites of satellite at –8 eV (open triangles, bulk alloys; solid triangles, surface alloys) and valence band at –1.5 eV (open circles, bulk alloys; solid circles, surface alloys) normalized to the main peak of $Cd_{1-x}Mn_xTe$ at –3.6 eV evaluated by Wall *et al.* [31]. All data were determined from the peak intensity relative to a secondary background (linearly interpolated between 0 and –16 to –17 eV) in the resonance curves.

intensities were defined relative to a linearly interpolated secondary background between 0 and –16 to –17 eV in the spectra measured just on resonance. Authors have claimed that the concentration dependence of the satellite intensity is in conflict with the results of CI analysis, and concluded that the unscreened d^4 identification of the many-body final states responsible for the satellite should be reexamined [31].

On the other hand, we should find again that the satellite and the valence-band intensity relative to the main peak indicate x-independence in our evaluated method, and are almost unchanged within the range of 0.48±0.03 and 0.23±0.03, respectively, as described in Chapter 6-2-3 (Fig. 6-7). We find that the inconsistency on the x dependence of the satellite intensity between our and Wall's groups would be mainly due to the data analysis method employed, and also to discrepancy of raw data in the low-concentration region below x = ~0.4

Here, we reiterate the following: (1) For pure CdTe, the emission intensity of the *sp* band

at –1.2 eV is about three times stronger than that at –3.4 eV, judging from the photoemission spectra of CdTe measured at $\hbar\omega$ = 47.0 or 49.5 eV and those of $Cd_{1-x}Mn_xTe$ taken at antiresonance ($\hbar\omega$ = 47.0 or 47.4 eV) in Fig. 6-5. (2) The Mn 3*d* emission intensity of $Cd_{1-x}Mn_xTe$ at –3.4 eV is about four times stronger than that at –1.2 eV, as one can recognize from the spectral shape of the Mn 3*d* partial DOS shown in Fig. 6-6. (3) The satellite intensity at –7 eV does not overlap at all with the *sp* valence bands [4].

Taking into account the items above, the results of analysis of our data based on the method in Ref. 31 can be understood as follows. The shape of the on-resonance spectra for $x \geq$ ~0.4 are reasonably assumed to be almost independent of x as a result of the dominant contribution of the Mn 3*d* emission to the spectra, since the cross section of the Mn 3*d* states at $\hbar\omega$ = 50 eV is about 30 times larger than that of the Te 5*p* states [13]. The decrease of x brings the decrease of the Mn 3*d* contribution and the relative increase of the contribution of the *sp* valence-band emission to the total valence-band spectra. Thus, if we normalize the peak intensities at –1.2 and –7 eV relative to that at –3.4 eV in the on-resonance spectra, the intensity at –1.2 eV would increase rapidly with the decrease of x from 0.4 to 0.1 as a result of an increasing contribution of the *sp* valence bands, while that at –7 eV would exhibit a slight decreases or no remarkable x dependence, in agreements with our results by the analysis based on Ref. 31.

Then, we believe that the present results in Fig. 6-7 are quite reasonable and support the d^4 identification for the satellite in the Mn 3*d* partial DOS.

6-2. Photoemission and inverse-photoemission study of zinc-blende MnTe

6-2-1. Ultraviolet photoemission and inverse-photoemission spectra of zinc-blende MnTe

Figure 6-13-(a) shows the valence-band UPS spectra measured at $\hbar\omega$ = 21.2 and 40.8 eV, and the conduction-band IPES spectrum of zinc-blende MnTe(111) epitaxial film, as an end point material of $Cd_{1-x}Mn_xTe$, grown on GaAs(100) substrate. Energy is referred to the VBM. The energy separation between the VBM and CBM evaluated by extrapolating the leading edge of the lowest conduction-band peak to the baseline is estimated to be about 2.0 eV. This value is smaller than the optical band gap of 2.92 eV at 300 K estimated from the optical absorption measurements [32] and determined as the peak energy of the magnetic circular dichroism spectra [33], mainly due to the characteristics of the overall energy resolution of the IPES spectrometer, as described above.

The UPS spectrum measured at 40.8 eV exhibits a peak at –1.5 eV, a narrow peak at –3.4 eV, a broad structure around –7.5 eV, and a peak at –11.4 eV, while the spectrum at 21.2 eV exhibits three peaks at –1.5, –3.4 and –4.3 eV with a shoulder at –1.0 eV. These fundamental features in the top 10 eV region of valence-bands are in agreement with results obtained by XPS [32] and synchrotron-radiation photoemission [34, 35] measurements. On the other hand, the IPES spectrum emphasizes a sharp peak at 3.5 eV and a broad structure around 7 eV.

6-2-2. Comparison with band-structure calculation

In order to compare the spectra obtained in the experiments with that by the band-structure calculation, Fig. 6-13-(b) shows the theoretical total DOS of antiferromagnetic zinc-blende MnTe based on the spin-polarized, self-consistent local-spin density total-energy and band-structure calculation reported by Wei and Zunger [16]. One can recognize that the whole feature of the experimental spectra except for the broad structure around –7.5 eV in the UPS spectrum

at 40.8 eV is qualitatively consistent with the theoretical DOS. The theoretical DOS of valence-bands can be divided into two parts: the Te 5*s* bands centered at –10.5 eV and the upper Te 5*p* and Mn 3*d* hybridization bands in the energy region from 0 to –4 eV. The prominent peak due to occupied Mn 3*d* states is placed at –2.5 eV. The theoretical DOS of conduction-bands, on the other hand, consists of almost dispersionless bands due to mainly Mn 3*d* states between 1 and

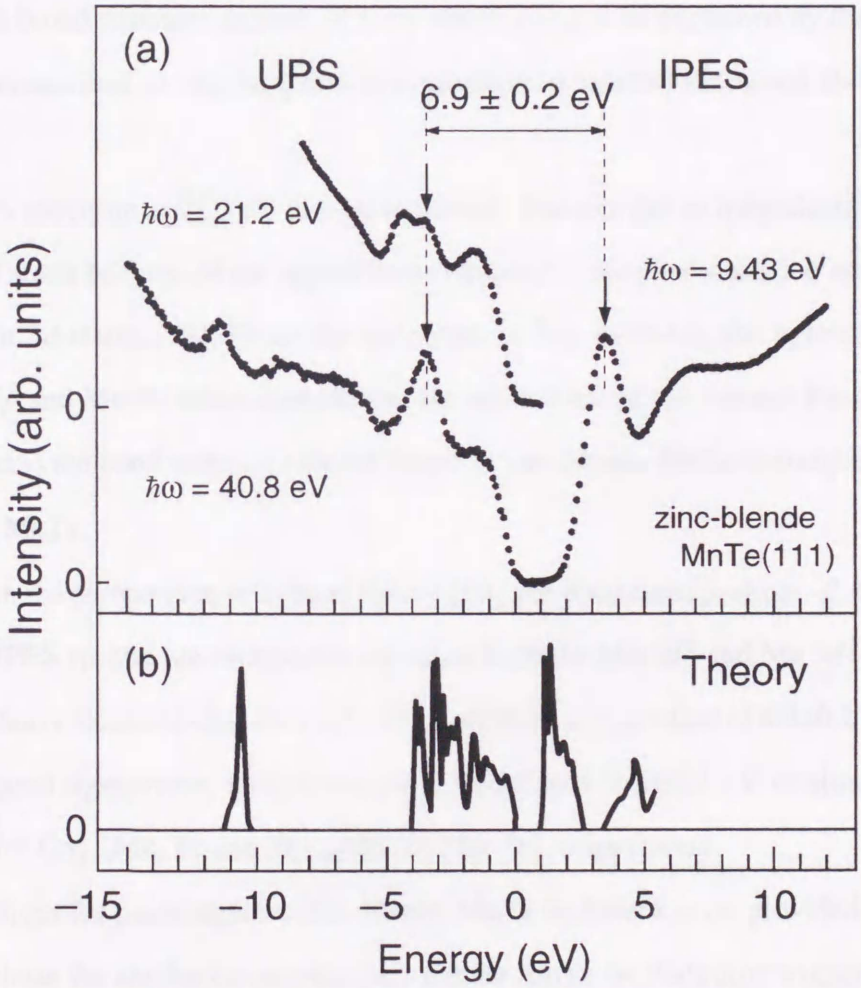

Fig. 6-13. (a) Valence-band UPS spectra measured at 40.8 and 21.2 eV, and conduction-band IPES spectrum of zinc-blende MnTe(111) epitaxial film grown on GaAs(100) substrate. Energy is referred to the VBM. Vertical arrows indicate peaks due to Mn 3*d* states with fairly localized character. (b) Total DOS of antiferromagnetic zinc-blende MnTe calculated by Wei and Zunger [16].

2.5 eV and *sp*-band states around 4.5 eV. The unoccupied Mn 3*d* states with high DOS are located at 2.2 eV. Theory predicts a U_{eff}-value of 4.7 eV.

At $\hbar\omega$ = 40.8 eV, the photoemission cross section of Mn 3*d* states is much larger than those of the Te 5*s* and 5*p* states [13]. Especially, the features of the UPS spectrum measured at 40.8 eV is very similar to those of the Mn 3*d* partial DOS of zinc-blende MnTe film evaluated from a resonant photoemission experiment in the Mn 3*p*-3*d* core excitation region [35]. Therefore, we ascribe the narrow peak at –3.4 eV to the Mn 3*d* states with fairly localized character. The broad structure around –7.5 eV which can not be explained by the one-electron band picture is ascribed to emission due to multielectron satellite discussed above [4, 28, 30, 35].

The UPS spectrum at 21.2 eV is used to identify features due to hybridization between Te 5*p* and Mn 3*d* states because of the approximate equality of the photoemission cross sections of Te 5*p* and Mn 3*d* states [13]. From the spectrum in Fig. 6-13-(a), the hybridization bands between Te 5*p* and Mn 3*d* states spread over the top 5.2 eV of the valence bands. In Chapter 6-2-3, we discuss the band width of valence bands in zinc-blende MnTe in comparison with that of NiAs-type MnTe.

Based on the comparison with band theory [16], the prominent peaks at –3.4 and 3.5 eV in the UPS and IPES spectra are ascribed to emission from the Mn $3d\uparrow$ and Mn $3d\downarrow$ states with e_g symmetry of fairly localized character [16, 17], providing a U_{eff}-value of 6.9±0.2 eV. This U_{eff}-value is in good agreement with those of 7.0±0.2 and 7.2±0.2 eV evaluated from our experiments for $Cd_{1-x}Mn_xTe$ and $Zn_{1-x}Mn_xTe$ [36–38], respectively.

Calculations for paramagnetic zinc-blende MnTe by Masek *et al.* provided a value of 5.5 eV [22] and those for antiferromagnetic zinc-blende MnTe by Podgórny suggested a value of about 4 eV for the splitting energy [23]. All of the calculated values [17, 22, 23] are substantially smaller than our experimental values of 6.9±0.2 eV. The U_{eff}-value of 5.7 eV for zinc-blende MnTe estimated by Bressler and Gumlich [39] seems to be at variance with the present value. There is, however, no inconsistency, since the value reported for zinc-blende MnTe [39] is only a measure of the lower limit of the exchange energy.

6-2-3. Comparison of the spectra of zinc-blende MnTe with those of NiAs-type MnTe

Finally, we discuss in comparison of the UPS and IPES spectra of zinc-blende MnTe with those of stable NiAs-type MnTe. The UPS and IPES spectra of NiAs-type MnTe have been reported by Sato *et al.* [40]. The UPS and IPES apparatuses used for the measurements were the same as those in the present study, and clean surfaces of samples were obtained by scraping with a diamond file.

Figure 6-14 shows the UPS at 21.2 eV and IPES spectra of zinc-blende and NiAs-type MnTe. The UPS and IPES spectra of NiAs-type MnTe exhibit three peaks with a shoulder and a main peak with a broad structure, respectively, as same as those of zinc-blende MnTe. We find that in the both UPS spectra the *p-d* hybridization bandwidth of 5.2 eV in the valence bands for

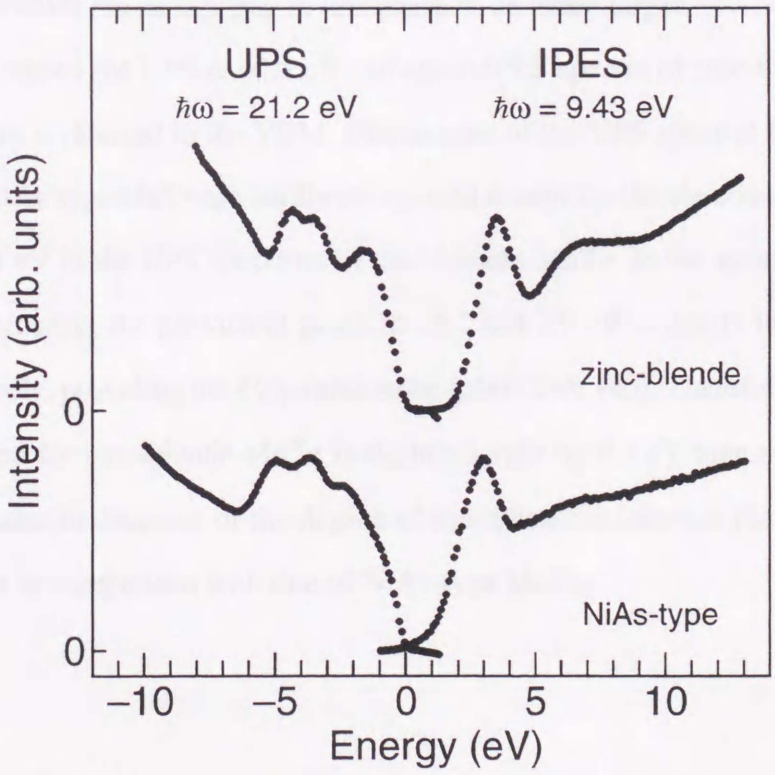

Fig. 6-14. Valence-band UPS spectra at 21.2 eV and conduction-band IPES spectra of zinc-blende MnTe and NiAs-type MnTe [40]. Energy is referred to the VBM.

zinc-blende MnTe is 1.3 eV smaller than that of 6.5 eV for NiAs-type. Moreover, the energy band gap between the VBM and the CBM decreases from 2.0 (zinc-blende MnTe) to 0.8 eV (NiAs-type MnTe).

In order to discuss properly the strength of different covalent interactions in hexagonal (NiAs-type MnTe) and cubic (zinc-blende MnTe) environments, Podgórny insists that one has to consider apart from the Mn–Te nearest neighbor (NN) distance, also the Mn–Mn and Te–Te next NN distances in both phases [23]. Accordingly, one notes the following: the Mn–Te, Mn–Mn and Te–Te distances are 2.74, 4.47 and 4.47 Å (cubic phase) and 2.92, 3.36 and 4.12 Å (hexagonal phase). It means that much smaller Mn–Mn and Te–Te distances in the hexagonal phase are expected to cause larger Mn 3*d* and Te 5*p* bandwidths due to increase of the overlap between the Mn 3*d* orbitals, and that between the Te 5*p* orbitals, respectively, in comparison to the cubic phase. That this is indeed the case is shown Fig. 6-14 where both spectra are compared. The width of the *p-d* hybridization bands is narrower by 1.3 eV in zinc-blende MnTe and this very fact causes the energy gap in this phase to be much larger.

Figure 6-15 shows the UPS at 40.8 eV and again IPES spectra of zinc-blende and NiAs-type MnTe. Energy is referred to the VBM. Differences of the UPS spectral features between zinc-blende and NiAs-type MnTe are hardly recognized except for the clear peak of Te 5*s* states exhibited at –11.4 eV in the UPS spectrum of zinc-blende MnTe. In the spectra of NiAs-type MnTe, one can recognize the prominent peaks at –3.7 and 2.9 eV to nearly localized Mn $3d\uparrow$ and $3d\downarrow$, respectively, providing the U_{eff}-value to be 6.6±0.2 eV [40]. Therefore, the U_{eff}-value of 6.9 eV evaluated for zinc-blende MnTe is slightly larger by 0.3 eV than that of 6.6 eV for NiAs-type MnTe,due to decrease of the degree of hybridization between the Mn 3*d* states of zinc-blende MnTe in comparison with that of NiAs-type MnTe.

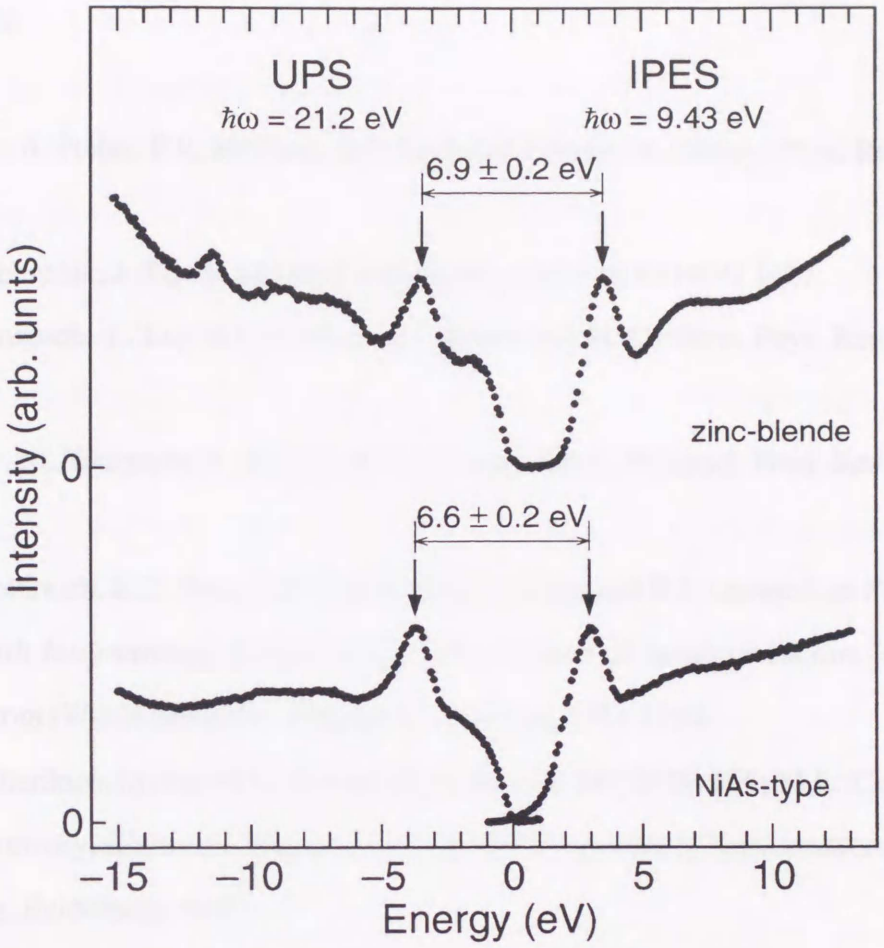

Fig. 6-15. Valence-band UPS spectra at 40.8 eV and conduction-band IPES spectra of zinc-blende MnTe and NiAs-type MnTe [40]. Energy is referred to the VBM. Vertical arrows indicate peaks due to Mn 3*d* states with fairly localized character.

References

[1] L. Ley, A. Pollak, F.R. McFeely, S.P. Kowalczyk and D.A. Shirley, Phys. Rev. B **9** (1974) 600.

[2] N.J. Shevchik, J. Tejeda and M. Cardona, Phys. Rev. B **9** (1974) 2627.

[3] M. Taniguchi, L. Ley, R.L. Johnson, J. Ghijsen and M. Cardona, Phys. Rev. B **33** (1986) 1206.

[4] L. Ley, M. Taniguchi, J. Ghijsen, R.L. Johnson and A. Fujimori, Phys. Rev. B **35** (1987) 2839.

[5] H. Ehrenreich, K.C. Hass, N.F. Johnson, B.E. Larson and R.J. Lampert, in *Proceedings of the 18th International Conference of the Physics* of Semiconductors, edited by O. Engstrom (World Scientific, Singapore, 1987), pp.1751-1754.

[6] J.R. Cherikowsky and M.L. Cohen, Phys. Rev. B **14** (1976) 556; M.L. Cohen and J.R. Cherikowsky, *Electronic Structure and Optical Properties of Semiconductors* (Springer-Verlag, Heidelberg, 1988).

[7] K.O. Magnusson, U.O. Karlsson, D. Straub, S.A. Flodstrom and F.J. Himpsel, Phys. Rev. B **36** (1987) 6566.

[8] D. Chadi, J.P. Walter, M.L. Cohen, Y. Petroff and M. Balkanski, Phys. Rev. B **5** (1972) 3058.

[9] A. Wall, Y. Gao, A. Raisanen, A. Franciosi and J.R. Cherikowsky, Phys. Rev. B **43** (1991) 4988.

[10] N.T. Khoi and J.A. Gaj, Phys. Status Solidi B **83** (1977) K133; K.C. Hass and H. Ehrenreich, J. Vac. Sci. Technol. A **1** (1983) 1678.

[11] P. Lautenschlager, S. Logothetidis, L. Vina and M. Cardona, Phys. Rev. B **32** (1985) 3811, and references therein.

[12] A. Kisiel, J. Oleszkiewicz, M. Podgórny, G. Dalba, F. Rocca and E. Burattini, J. Cryst. Growth **101** (1990) 239.

[13] J.J. Yeh and I. Lindau, At. Data Nucl. Data Tables **32** (1985) 45 and 72.

[14] D.A. Shirley, Phys. Rev. B **5** (1972) 4709.

[15] S.-H. Wei and A. Zunger, Phys. Rev. Lett. **56** (1986) 2391.

[16] S.-H. Wei and A. Zunger, Phys. Rev. B **35** (1987) 2340.

[17] B.E. Larson, K.C. Hass, H. Ehrenreich and A.E. Carlsson, Phys. Rev. B 37 (1988) 4137.

[18] B.E. Larson and H. Ehrenreich, Phys. Rev. B **39** (1989) 1747.

[19] B.E. Larson and H. Ehrenreich, J. Appl. Phys. **67** (1990) 5084.

[20] D. Heiman, Y. Shapira and S. Foner, Solid State Commun. **51** (1984) 603.

[21] A. Balzarotti, M. Czyżyk, A. Kisiel, N. Motta, M. Podgórny and M. Zimnal-Starnawska, Phys. Rev. B 30 (1984) 2295; A. Balzarotti, N. Motta, A. Kisiel, M. Zimnal-Starnawska, M.T. Czyżyk and M. Podgórny, Phys. Rev. B 31 (1985) 7526.

[22] J. Masek, B. Velicky and V. Janis, Acta Phys. Pol. A 69 (1986) 1107.

[23] M. Podgórny, Z. Phys. B 69 (1988) 501.

[24] A. Franciosi, A. Wall, Y. Gao, J.H. Weaver, M.-H. Tsai, J.D. Dow, R.V. Kasowski, R. Reifenberger and F. Pool, Phys. Rev. B 40 (1989) 12009.

[25] T. Kendelewicz, J. Phys. C 14 (1981) L407.

[26] Y.R. Lee and A.K. Ramdas, Solid State Commun. 51 (1984) 861.

[27] O. Gunnarsson, A.V. Postnikov and O.K. Andersen, Phys. Rev. B 39 (1989) 1708; Phys. Rev. B 40 (1989) 10407.

[28] T. Mizokawa and A. Fujimori, Phys. Rev. B 48 (1993) 14150; A. Fujimori and T. Mizokawa, *Electronic Structure of 3d Transition-Metal Impurities in Semiconductors, in II-VI Semiconductor Compounds*, edited by M.Jain (World Scientific, Singapore, 1992) p.103.

[29] W.A. Harrison, *Electronic Structure and the Properties of Solids* (Freeman, San Francisco, 1980).

[30] M. Taniguchi, A. Fujimori, M. Fujisawa, T. Mori, I. Souma and Y. Oka, Solid State Commun. **62** (1987) 431.

[31] A. Wall, A. Raisanen, G. Haugstad, L. Vanzetti and A. Franciosi, Phys. Rev. B **44** (1991) 8185.

[32] H. Anno, T. Koyanagi and K. Matsubara, J. Cryst. Growth **117** (1992) 816.

[33] K. Ando, K. Takahashi and T. Okuda, J. Magn. Magn. Mater. **104-107** (1992) 993.

[34] D.W. Niles, H. Hochst and M.A. Engelhardt, J. Electron Spectrosc. Related Phenom. **52** (1990) 139.

[35] P.R. Bressler and H.-E. Gumlich, J. Cryst. Growth **138**, 1028 (1994).

[36] M. Taniguchi, N. Happo, K. Mimura, H. Sato, J. Harada, K. Miyazaki, H. Namatame, Y. Ueda and M. Ohashi, J. Phys.: Condens. Matter **7** (1995) 4371.

[37] K. Mimura, N. Happo, H. Sato, J. Harada, K. Miyazaki, H. Namatame, Y. Ueda, M. Ohashi and M. Taniguchi, Cryst. Res. Technol. **31** (1996) 911.

[38] K. Mimura, N. Happo, H. Sato, J. Harada, K. Miyazaki, H. Namatame, Y. Ueda, M. Ohashi and M. Taniguchi, J. Electron Spectrosc. Related Phenom. **79** (1996) 13.

[39] P.R. Bressler, H.-E. Gumlich, Mater. Sci. Forum, **182-184** (1995) 639.

[40] H. Sato, M. Tamura, N. Happo, T. Mihara, M. Taniguchi and Y. Ueda, Solid State Commun. **92** (1994) 921.

Chapter 7.
Conclusion

We have *in situ* measured the valence-band UPS and conduction-band IPES spectra of $Cd_{1-x}Mn_xTe$ films ($0 \leq x \leq 0.7$) grown epitaxially on GaAs(100) substrates. In order to overcome the electrostatic charging effects in measurements of IPES spectra, we have constructed an HWE reactor. The IPES spectrum of pure CdTe shows peak structures at 3.7, 5.4, 6.4 and 9.0 eV above the VBM. On the basis of the results of band-structure calculation, these structures are interpreted to be associated with the DOS features due to particular flat regions of conduction bands around the X_6 and X_7, Γ_7 and Γ_8, $L_{4,5}$ and L_6, and the Λ symmetry points, respectively. With increasing x, the energy position of the CBM relative to the VBM shifts linearly toward higher energy as a result of an increasing contribution of the Mn 4*s* states to the conduction bands.

We have performed the Mn 3*p*-3*d* RPES experiments for bulk $Cd_{1-x}Mn_xTe$ ($0.10 \leq x \leq 0.69$), in order to investigate the Mn 3*d* contribution in $Cd_{1-x}Mn_xTe$ in detail. A prominent resonance for the peak at –3.4 eV relative to the VBM has been observed. The resonance does not only take place around the peak at –3.4 eV, but also over all regions of valence bands, and anathor states between –5 and –9 eV is also resonantly enhanced. Furthermore, relative intensities of the valence band at –1.2 eV and the multielectron satellite at –7 eV to the main peak at –3.4 eV, evaluated from the Mn 3*d* derived partial DOS, are almost independent of Mn concentration.

The energy position of the Mn 3*d*↓ states at 3.6 eV above the VBM in the present study is in good agreement with that predicted from the analysis of the Te L_1 and L_3 edge XANES spectra combined with the electronic structure calculation. The U_{eff}-value is directly estimated to be 7.0±0.2 eV. This value compares well with the predicted spin-exchange splitting energy of 7.0 eV in support of the electronic structure model, though the present result is substantially smaller than the earlier experimental value of 8.3±0.4 eV from the photoemission and BIS

measurements.

For the initial states of transitions responsible for the Mn derived feature at 4.6 eV in the reflectivity spectra, the valence-band states around the X_5 symmetry points are assumed to be the most probable candidate based on the location of the Mn $3d\downarrow$ states at 3.6 eV.

Aside from energy-band theory, the peak at 3.6 eV, features between 0 and –5 eV with a main peak at –3.4 eV, and those between –5 and –9 eV are assigned to the d^6, $d^5\underline{L}$ and d^4 final states, respectively, on the basis of the CI calculations using the cluster and Anderson impurity models.

We have also measured the UPS and IPS spectra of zinc-blende MnTe(111) epitaxial film on GaAs(100) substrate grown using the HWE reactor. We have directly estimated the U_{eff}-value of 6.9±0.2 eV. This value is in good agreement wiht those of $Cd_{1-x}Mn_xTe$ (7.0±0.2 eV) and $Zn_{1-x}Mn_xTe$ (7.2±0.2 eV). In addition, we compared the valence-band UPS and conduction-band IPES spectra of zinc-blende MnTe with those of stable NiAs-type MnTe. The band width in the valence-band region and U_{eff}-value of zinc-blende MnTe are narrower by 1.3 eV and larger by 0.3 eV than those of NiAs-type, respectively. A decrease in the band width from NiAs-type MnTe to zinc-blende MnTe is tentatively ascribed to the reduced overlap between the Mn 3*d* orbitals or the Te 5*p* orbitals with the increase of Mn–Mn and Te–Te next nearest neighbor distances, while an increase in the U_{eff}-value would be ascribed to the decrease of the degree of hybridization between the Mn 3*d* states.

Acknowledgments

I would like to express sincere gratitude to Prof. Masaki Taniguchi for his excellent guidance and continuous encouragement in completing this work. I am also grateful to Prof. Shinya Hosokawa, Prof. Hirofumi Namatame, Prof. Yoshifumi Ueda (Kure National College of Technology) and Prof. Michie Koyama (Kure National College of Technology) for their supports and valuable suggestions. I would like to sincerely thank to Dr. Hitoshi Sato, Dr. Naohisa Happo (Hiroshima City University), Dr. Izumi Ono (Toyota Technological Institute) and Dr. Masashi Nakatake for their supports, valuable suggestions and collaboration.

I am deeply grateful to Mr. Koichi Yokoyama (Kawasaki Iron Co. Ltd.), Mr. Jiro Harada, Mr. Keiji Miyazaki, Mr. Shinya Senba and Mr. Masatoshi Kioka (CXR) for their collaborations on the construction of HWE apparatus, growth of DMSs and the measurements of the UPS and IPES spectra, and to the other members of Taniguchi laboratory for their friendly help and collaborations. I deeply thank to Ms. Naomi Ishii, Ms. Ayako Gofuku and Ms. Naoko Matsuo for their support on office work.

I also acknowledge all members of the Hiroshima Synchrotron Radiation Center, Prof. Masaki Taniguchi, Prof. Katsuhide Yoshida, Prof. Hirofumi Namatame, Prof. Eiji Hashimoto, Prof. Jacques Ghijsen, Dr. Kenya Shimada, Dr. Shinya Yagi, Dr. Kiminori Goto, Dr. Ghalip Kutluk and Dr. Noriyuki Ojima for their support on this work.

I am grateful to Mr. Nobuhiko Shimizu and all members in Workshop for Advanced Techniques of metal and glass material sections for their strong technical support for the present study.

I would like to sincerely thank to Prof. Shojiro Takeyama (Himeji Institute of Technology), Prof. Yasuo Oka (Tohoku University) and Dr. Izuru Souma (Tohoku University) for their much discussions on the construction of HWE reactor and on the growth of thin films. I am grateful to Prof. Tamio Oguchi for stimulating discussions on theoretical aspects, and to Prof. Atsushi Fujimori (The University of Tokyo) and Dr. Takashi Mizokawa (The University of Tokyo) for discussions on the CI theory. I am grateful to Prof. Seiichi Miyazaki and Dr.

Masao Ohashi (Tokuyama National College of Technology) for measurements of thickness and XPS spectra of epitaxial films, and to Mr. Asao Minami for an electron-probe microanalysis on bulk samples, respectively. I thank also to Dr. Yasuhisa Tezuka and the staff of SRL-ISSP for the operation of SOR-RING and technical support.

Finally, I acknowledge my parents, Saburo Mimura and Katsumi Mimura, and my sister, Yoshiko Mimura, for their excellent understanding on my work and financial supports.

This work is partly supported by the Grant-in-Aid for Scientific Research from the Ministry of Education, Science and Culture, Japan, Iketani Science and Technology Foundation, The Ogasawara Foundation for the Promotion of Science and Technology, The Murata Science Foundation and Shimazu Science Foundation.

公表論文リスト

(1) Mn 3d states of $Cd_{1-x}Mn_xTe$
($Cd_{1-x}Mn_xTe$ の Mn 3*d* 状態) 1冊
共著者　三村功次郎、佐藤仁、原田次郎、宮崎圭司、谷口雅樹、植田義文
(学術誌) Journal of Magnetism and Magnetic Materials **140–144**, 2017–2018 (1995).
(ELSEVIER SCIENCE PUBLISHERS B.V.)　1995年出版

(2) Ultraviolet inverse-photoemission and photoemission spectroscopy studies of diluted magnetic semiconductors $Cd_{1-x}Mn_xTe$ ($0 \le x \le 0.7$)
(希薄磁性半導体 $Cd_{1-x}Mn_xTe$ ($0 \le x \le 0.7$) の真空紫外逆光電子・光電子分光による研究) 1冊
共著者　谷口雅樹、三村功次郎、佐藤仁、原田次郎、宮崎圭司、生天目博文、植田義文
(学術誌) Physical Review B **51**, 6932–6939 (1995).
(THE AMERICAN PHYSICAL SOCIETY)　1995年3月15日出版

(3) ULTRAVIOLET INVERSE-PHOTOEMISSION AND PHOTOEMISSION STUDIES OF DILUTED MAGNETIC SEMICONDUCTOR $Cd_{1-x}Mn_xTe$
(希薄磁性半導体 $Cd_{1-x}Mn_xTe$ の真空紫外逆光電子・光電子分光による研究) 1冊
共著者　谷口雅樹、三村功次郎、佐藤仁、生天目博文、植田義文
(学術誌) *Proceedings of 22nd International Conference on the Physics of Semiconductors* (Vancouver) **3**, 2565–2568 (1994).
(World Scientific Publishing Co. Pte. Ltd.)　1995年出版

(4) Ultraviolet inverse-photoemission and photoemission spectroscopies of zincblende MnTe
(閃亜鉛鉱型 MnTe の真空紫外逆光電子・光電子分光) 1冊
共著者　三村功次郎、佐藤仁、仙波伸也、生天目博文、谷口雅樹
(学術誌) Physica B, in press.
(ELSEVIER SCIENCE PUBLISHERS B.V.)　1997年出版予定

参考論文リスト

(1) Bandpass photon detector for inverse photoemission spectroscopy
(逆光電子分光装置のためのバンドパス型光検出器) 1冊
共著者 横山浩一、西原克浩、三村功次郎、開康子、谷口雅樹、植田義文、藤沢正美
(学術誌) Review of Scientific Instruments **64**, 87–90 (1993).

(2) Performance of the inverse photoemission spectrometer with a new bandpass photon detector of narrow bandwidth and high sensitivity
(狭帯域および高感度の新型バンドパス型光検出器を有する逆光電子分光装置の性能評価) 1冊
共著者 植田義文、西原克浩、三村功次郎、開康子、谷口雅樹、藤沢正美
(学術誌) Nuclear Instruments and Methods in Physics Research A**330**, 140–143 (1993).

(3) d^4 identification of the satellite in the Mn 3*d* photoemission spectra of $Cd_{1-x}Mn_xTe$ alloys
($Cd_{1-x}Mn_xTe$ の合金の Mn 3*d* 光電子スペクトル中のサテライトの d^4 の帰属について) 1冊
共著者 八方直久、佐藤仁、三村功次郎、細川伸也、谷口雅樹、植田義文、小山通栄
(学術誌) Physical Review B **50**, 12211–12214 (1994).

(4) Photoemission and EXAFS studies of $Zn_{1-x}Mn_xTe$
($Zn_{1-x}Mn_xTe$ の光電子分光と広域X線吸収微細構造研究) 1冊
共著者 八方直久、佐藤仁、三原隆弘、三村功次郎、細川伸也、谷口雅樹、植田義文
(学術誌) *Proceedings of the 22nd International Conference on the Physics of Semiconductors* (Vancouver) **3** (1994) 2497–2500.

(5) Mn and Te K-edge EXAFS studies of $Zn_{1-x}Mn_xTe$
($Zn_{1-x}Mn_xTe$ の Mn および Te-*K* 吸収端広域X線吸収微細構造研究) 1冊
共著者 八方直久、佐藤仁、三原隆弘、三村功次郎、細川伸也、谷口雅樹、植田義文
(学術誌) Physica B **208&209**, 291–292 (1995).

(6) Ultraviolet inverse-photoemission and photoemission spectra of diluted magnetic semiconductor $Zn_{1-x}Mn_xTe$
(希薄磁性半導体 $Zn_{1-x}Mn_xTe$ の真空紫外逆光電子・光電子スペクトル) 1冊
共著者 谷口雅樹、八方直久、三村功次郎、佐藤仁、原田次郎、宮崎圭司、生天目博文、植田義文、大橋正夫
(学術誌) Journal of Physics : Condensed Matter **7**, 4371–4383 (1995).

(7) Mn 3d states in diluted magnetic semiconductor $Zn_{1-x}Mn_xTe$
(希薄磁性半導体 $Zn_{1-x}Mn_xTe$ 中の Mn 3*d* 状態) 1冊
共著者 三村功次郎、八方直久、佐藤仁、原田次郎、宮崎圭司、生天目博文、植田義文、大橋正夫、谷口雅樹
(学術誌) Jounal of Electron Spectroscopy and Related Phenomena **79**, 13–16 (1996).

(8) Ultraviolet inverse-photoemission and photoemission spectroscopies of $Zn_{1-x}Mn_xTe$ films grown by hot wall epitaxy
(ホットウォールエピタキシー法により成長した$Zn_{1-x}Mn_xTe$薄膜の真空紫外逆光電子・光電子分光) 1冊
共著者 三村功次郎、八方直久、佐藤仁、原田次郎、宮崎圭司、生天目博文、植田義文、大橋正夫、谷口雅樹
(学術誌) Crystal Research and Technology **31**, 911–914 (1966).

(9) Zn, Mn and Te K-edge EXAFS studies of the diluted magnetic semiconductor $Zn_{1-x}Mn_xTe$
(希薄磁性半導体の Zn、Mn および Te-K 吸収端広域 X 線吸収微細構造研究) 1冊
共著者 八方直久、佐藤仁、三原隆弘、三村功次郎、細川伸也、植田義文、谷口雅樹
(学術誌) Journal of Physics : Condensed Matter **8**, 4315–4323 (1996).

(10) Mn 3d, 3p AND 3s RESONANT PHOTOEMISSION AT Mn 2p CORE THRESHOLD OF NiAs-TYPE MnTe
(NiAs 型の Mn 2p 内殻吸収領域での Mn 3d、3p、3s 共鳴光電子放出) 1冊
共著者 佐藤仁、古田明仁、田中新、三村功次郎、仙波伸也、八方直久、城健男、谷口雅樹、植田義文
(学術誌) *Proceedings of the 23nd International Conference on the Physics of Semiconductors*, in press.